Superconductivity in diamond and related materials

Philipp Achatz

THÈSE

présentée devant l'Université Joseph Fourier – Grenoble I
en co-tutelle avec la Technische Universität München

pour l'obtention du

DIPLOME DE DOCTORAT

par

Philipp ACHATZ

METAL-INSULATOR TRANSITION AND SUPERCONDUCTIVITY IN HEAVILY BORON-DOPED DIAMOND AND RELATED MATERIALS

Préparée au Laboratoire de Transport Electronique, Quantique et Supraconductivité
(LaTEQS) du Commissariat à l'Energie Atomique (CEA) de Grenoble,
à l'Institut Néel du Centre National de la Recherche Scientifique (CNRS) de Grenoble et
en co-tutelle avec le Walter Schottky Institut de la Technische Universität München,
dans le cadre de l'Ecole Doctorale de Physique

Soutenue publiquement le 24 Novembre 2008, devant le jury composé de

E. Gheeraert	Président
C. Nebel	Rapporteur
J. Lesueur	Rapporteur
C. Marcenat	Directeur de thèse
E. Bustarret	Co-directeur de thèse
M. Stutzmann	Co-directeur de thèse (Allemagne)

Contents

Zusammenfassung

Im Laufe dieser Doktorarbeit wurde der Metall-Isolator-Übergang und die Supraleitung in einkristallinem hoch Bor-dotierten Diamant und verwandten Materialien untersucht. Die Entdeckung der Supraleitung in diesem Material in 2004 zusammen mit der Idee, dass Halbleiter unter ausreichender Dotierung metallisch werden, haben eine detaillierte Studie des Transports bei tiefen Temperaturen motiviert und initiiert. Darüber hinaus ergab sich neues Interesse am Metall-Isolator-Übergang und der Supraleitung in anderen kovalent-gebundenen Gruppe IV Elementen, was zur Untersuchung von hoch Bor-dotierten einkristallinem Silizium sowie hoch Aluminium-dotierten 4H Siliziumkarbid führte. Eine weitere Idee bestand darin, die supraleitenden Eigenschaften von hoch Bor-dotierten nanokristallinem Diamant zu untersuchen, um die Robustheit dieses Effekts bezüglich Diamant zu bestätigen. Die Untersuchung des Metall-Isolator-Übergangs in diesem System zeigte zudem die Wichtigkeit der Granularität dieses Systems.

Im Fall von einkristallinem hoch Bor-dotierten Diamant erlaubte das gut kontrollierte Wachsen der Schichten eine detaillierte Studie des doping-induzierten Metall-Isolator-Übergangs. Die kritische Borkonzentration n_c erwies sich als dieselbe für den Metall-Isolator-Übergang als auch für den Normalleiter-Supraleiter-Übergang. Alle metallischen Proben zeigten Supraleitung und es wurde eine Verbindung zwischen dem Auftreten der Supraleitung und der Nähe zum Metall-Isolator-Übergang hergestellt (mittels Skalengesetz).

Darüberhinaus wurde der Ursprung der Supraleitung in einkristallinem Diamant untersucht. Zu diesem Zweck wurden isotopisch substituierte Proben (zum ersten Mal in unserer Gruppe) gewachsen. Beide Arten von Substitution (Matrix sowie Dotieratom) wurden durchgeführt, wodurch neben den Standard-$^{12}C^{11}B$-Proben die substituierten Probenserien $^{13}C^{11}B$ und $^{13}C^{10}B$ kamen. Allerdings waren die Ergebnisse aus Tieftemperaturtransport und Supraleitung nicht schlüssig, aber erleichtern und motivieren eine detailliertere Studie. Raman-Spektroskopie an diesen Serien hat es erlaubt, die Charakteristik um etwa 500 cm^{-1} auftretend mit einer Phononmode zu identifizieren, die Bor-Bor-Paaren zugeordnet werden kann. Diese zeigten sich als elektrisch inaktiv

und spielen eine wichtige Rolle für Studien in Abhängigkeit von der Borkonzentration.

Messungen des Hall-Effekts in einkristallinem hoch Bor-dotierten Diamant ergaben eine rätselhafte Situation, mit Ladungsträgerdichten bis um einen Faktor 10 höher als die Borkonzentration, die durch Sekundärionen-Massenspektroskopie (SIMS) bestimmt wurde. Basierend auf der Tatsache, dass der Hall-Koeffizient in gestrecktem Silizium stark durch den reentranten Charakter der Fermi-Oberfläche geprägt ist, wurde ein ähnlicher Vorschlag erbracht, der oben genannte Diskrepanz zwischen Hall- und SIMS-Messungen erklären kann.

Wie bereits erwähnt, spielt die Granularität eine wichtige Rolle in Bezug auf den Metall-Isolator-Übergang und die Supraleitung in hoch bor-dotierten nanokristallinem Diamant. Der Transport bei tiefen Temperaturen folgt demjenigen erwartet für ein metallisches oder nichtleitendes granuläres System, je nach dem Zusammenspiel zwischen intergranulärer und intragranulärer Leitfähigkeit. Der Metall-Isolator-Übergang findet an einer kritischen Leitfähigkeit g_c statt. Die Granularität beeinflusst auch deutlich die supraleitenden Eigenschaften durch die Einführung der supraleitenden Energielücke Δ und der Josephson-Kopplung J zwischen supraleitenden Körnern. Ein Peak im Magnetwiderstand kann durch supraleitende Fluktuationen und die Granularität des Systems erklärt werden.

Hoch Bor-dotiertes einkristallines Silizium gilt als Modell-System und der Metall-Isolator-Übergang wurde ausgiebig in diesem System untersucht, mit einer kritischen Borkonzentration von $n_B \approx 4 \times 10^{18}\ cm^{-3}$. Fortschritte wurden auf dem Gebiet der Herstellung erzielt und Laser-Doping-Techniken ergaben Zugang zu Proben mit viel höherer Borkonzentration ($n_B \approx 10^{21}\ cm^{-3}$). Der Transport bei tiefen Temperaturen solcher durch *gas immersion laser doping* hergestellten Proben zeigten einen supraleitenden Übergang bei sehr tiefen Temperaturen.

Der Metall-Isolator-Übergang wurde schon in n-Typ 4H Siliziumkarbid untersucht, metallische Leitfähigkeit wurde noch nicht in p-Typ 4H Siliziumkarbid gefunden. In unserem Fall wurden hoch Aluminium-dotierte Siliziumkarbid-Proben durch eine vapour-liquid-solid (VLS) Technik hergestellt, mit Konzentrationen bis zu $n_{Al} \approx 8.7 \times 10^{20}\ cm^{-3}$. Transportmessungen bei tiefen Temperaturen und temperaturabhängige Raman-Spektroskopie geben experimentellen Nachweis für den Metall-Isolator-Übergang. Darüberhinaus werden vorläufige Ergebnisse über die LO-Phonon-Plasmon-Kopplung in aluminium-dotierten 4H Siliziumkarbid (erstmalig) gezeigt.

Résumé

Au cours de cette thèse, la transition métal-isolant et la supraconductivité ont été étudiés dans le diamant monocristallin fortement dopé au bore et des matériaux voisins. La découverte de la supraconductivité dans le diamant fortement dopé au bore en 2004 a motivé, avec l'idée de rendre un semiconducteur métallique en le dopant suffisamment, l'étude détaillée du transport à basse température dans ce système. Cela a également donné un regain d'intérêt pour la transition métal-isolant et la supraconductivité dans d'autres éléments du groupe IV à liaisons covalents, ce qui conduit à l'étude du silicium monocristallin fortement dopé au bore ainsi du carbure de silicium 4H fortement dopé à l'aluminium. Une autre idée était de tester les propriétés supraconductrices dans le diamant nanocristallin fortement dopé au bore afin de confirmer la robustesse de cet effet. En outre, l'étude de la transition métal-isolant dans ce système a mis en évidence l'importance de l'aspect granulaire sur les propriétés de transport à basse température.

La synthèse bien contrôlée des échantillons de diamant fortement dopé au bore nous a permis d'étudier en détail la transition métal-isolant induite par le dopage. La concentration critique de bore n_c pour la transition métal-isolant s'est avéré être la même que pour la transition normal-supraconducteur. Tous les échantillons métalliques ont été trouvés supraconducteurs et nous avons été en mesure d'établir un lien entre l'apparition de la supraconductivité et la proximité de la transition métal-isolant. A cet effet, une approche en loi d'échelle basée sur le transport à basse température a été proposée.

En outre, nous avons essayé d'étudier l'origine de la supraconductivité dans le diamant monocristallin fortement dopé au bore. Des échantillons avec substitution isotopique ont été élaborés pour la première fois dans notre groupe. Les deux types de substitution (concernant la matrice et le dopant) ont été utilisés, ce qui donne à côté de la série standard $^{12}C^{11}B$ les deux séries en substitution isotopique : $^{13}C^{11}B$ et $^{13}C^{10}B$. Toutefois, les résultats sur le transport à basse température et la supraconductivité n'ont pas été concluants, même s'ils ouvrent la voie et motivent une étude plus détaillée. Des mesures de spectroscopie Raman sur les échantillons en substitution

isotopique ont permis l'attribution du pic observé à faible nombre d'onde (autour de 500 cm^{-1}) à un mode de vibration associé aux dimères de bore. Ceux-ci se sont révélés d'être électriquement inactifs et jouent un rôle important pour les études en fonction de la concentration totale de bore.

Des mesures d'effet Hall sur les échantillons de diamant monocristallin fortement dopé au bore ont créé une situation troublante. La concentration de porteurs mesurée par effet Hall est jusqu'à un facteur 10 supérieure à la concentration de bore déterminée par spectroscopie de masse des ions secondaires (SIMS). Compte tenu du fait que le coefficient de Hall dans le silicium contraint est fortement influencé par la nature réentrante de la surface de Fermi, une approche similaire est proposée pour expliquer l'écart mentionné entre mesures d'effet Hall et mesures de SIMS.

Comme nous l'avons déjà mentionné, la granularité joue un rôle important dans le cas du diamant nanocristallin fortement dopé au bore. Le transport à basse température suit celui attendu pour un système granulaire métallique ou isolant, en fonction de l'interaction de conductance intergranulaire et intragranulaire. La transition métal-isolant a lieu à une conductance critique g_c. La granularité influence également de manière significative les propriétés supraconductrices par l'introduction du gap supraconducteur Δ et du couplage Josephson J entre les grains. Un pic en magnétorésistance a été observé qui peut être expliqué par des fluctuations supraconduteurs et la granularité du système.

Le silicium monocristallin dopé au bore a servi comme modèle de référence et la transition métal-isolant a été étudié en détail dans ce système. Toutefois, jusqu'à 2006, aucune transition supraconductrice n'a été observée. Beaucoup de progrès ont été faits au niveau de la fabrication des échantillons et des techniques à dopage par laser (par ex. *GILD*) ont donné accès à des échantillons avec des concentrations de bore beaucoup plus élevées ($n_B \approx 10^{21}\ cm^{-3}$). Nous avons étudié le transport à basse température de tels échantillons, dont certains ont révélé une transition supraconductrice.

Bien que la transition métal-isolant ait été étudié dans le carbure de silicium 4H de type n, la métallicité n'ait pas été trouvée expérimentalement pour le carbure de silicium 4H de type p. Dans notre cas, des échantillons de carbure de silicium 4H fortement dopé à l'aluminium ont été élaborés par une technique VLS avec des concentrations jusqu'à $n_{Al} \approx 8.7 \times 10^{20}\ cm^{-3}$. Le transport et la spectroscopie Raman en fonction de la température montrent clairement la preuve expérimentale de la transition métal-isolant dans ce système. En outre, des résultats préliminaires sur le couplage LO-phonon-plasmon sont montrés pour la première fois dans le carbure de silicium 4H dopé à l'aluminium.

Summary

During this PhD project, the metal-insulator transition and superconductivity of highly boron-doped single crystal diamond and related materials have been investigated. The discovery of superconductivity in this material in 2004 together with the idea to render a semiconductor metallic upon doping sufficiently, initiated and motivated the detailed study of its low temperature transport. It also yielded renewed interest in the metal-insulator transition and superconductivity in other covalently-bonded group IV elements, leading to the investigation of highly boron-doped cubic single crystal silicon and also highly aluminum-doped 4H silicon carbide. Another idea was to test the superconducting properties of highly boron-doped nanocrystalline diamond to confirm the robustness of this effect. The study of the metal-insulator transition in this system further revealed the importance of the granularity of this system.

In the case of highly boron-doped single crystal diamond films, the well-controlled synthesis of the samples allowed us to study in detail the doping-induced metal-insulator transition. The critical boron concentration n_c for the metal-insulator transition was found to be the same as for the normal-superconductor transition. All metallic samples have been found to be superconducting and we were able to link the occurence of superconductivity to the proximity to the metal-insulator transition. For this purpose, a scaling law approach based on low temperature transport was proposed.

Furthermore, we tried to study the nature of the superconductivity in highly boron-doped single crystal diamond. Isotopically substituted samples have been grown for the first time in our group. Both types of substitution (including host lattice and dopant) were performed, yielding beside the standard $^{12}C^{11}B$ samples the isotopically controlled $^{13}C^{11}B$ and $^{13}C^{10}B$ series. However, the results on the low temperature transport and superconductivity were not conclusive, but pave the way for a more detailed study. Raman spectroscopy measurements on the isotopically substituted series suggest that the feature occuring at low wavenumbers ($\approx$ 500 cm^{-1}) is the A1g vibrational mode associated with boron dimers, which have been shown to be

electrically inactive and play an important role for studies as a function of total boron concentration.

Usual Hall effect measurements yielded a puzzling situation in metallic boron-doped diamond samples, leading to carrier concentrations up to a factor 10 higher than the boron concentration determined by secondary ion mass spectroscopy (SIMS). Based on the fact that the Hall coefficient in strained silicon is greatly influenced by the re-entrant nature of its Fermi surface, a similar approach is proposed to explain the above mentioned discrepancy between Hall and SIMS measurements.

As already mentioned, the granularity plays an important role in the case of highly boron-doped nanocrystalline diamond films. The low temperature transport follows the one expected for a granular metal or insulator, depending on the interplay of intergranular and intragranular (tunneling) conductance. The metal-insulator transition takes place at a critical conductance g_c. The granularity also influences significantly the superconducting properties by introducing the superconducting gap Δ in the grain and Josephson coupling J between superconducting grains. A peak in magnetoresistance is observed which can be explained by superconducting fluctuations and the granularity of the system.

Highly boron-doped cubic silicon served as a model system and the metal-insulator transition has been studied extensively in this system, revealing a critical concentration $n_B \approx 4 \times 10^{18}\ cm^{-3}$. However, until recently, no superconducting transition has been observed. Progress on the field of fabrication has been made and laser doping techniques gave access to samples with much higher boron concentrations ($n_B \approx 10^{21}\ cm^{-3}$). We studied the low temperature transport of such samples grown by *gas immersion laser doping*, some of which yielded a superconducting transition at very low temperatures.

Whereas the metal-insulator transition has been studied in n-type 4H silicon carbide, metallicity has not been found experimentally for highly-doped p-type 4H silicon carbide. In our case, highly aluminum-doped samples have been grown by a vapour-liquid-solid (VLS) technique with concentrations up to $n_{Al} \approx 8.7 \times 10^{20}\ cm^{-3}$. Low temperature transport and temperature dependent Raman spectroscopy clearly reveal experimental evidence for the metal-insulator transition in this system. Furthermore, preliminary results on the LO-phonon-plasmon coupling are shown for the first time in aluminum-doped 4H SiC by Raman spectroscopy.

1. Introduction

The electrical conductivity is probably the observable physical property which spans the widest range, starting from approximately $10^{-22}\ \Omega^{-1}cm^{-1}$ in the best insulators to around $10^{10}\ \Omega^{-1}cm^{-1}$ in pure metals (neglecting the phenomenon of superconductivity) [1, 2]. There are numerous experimental situations where materials can change from highly conducting metals into highly resistive insulators [3, 4, 5, 6, 7, 8, 9, 10]. These metal-insulator transitions can be induced by continuous changes of control parameters such as composition or pressure, etc. In one of the first publications [4] Mott mentioned that *The aim of this paper is to give a more detailed treatment of this problem* (the difference between metals and non-metals) *and to apply it to the behavior of a semiconductor containing a high concentration of impurity centers.*

1.1. Metal-insulator transition in doped semiconductors

In the beginning of semiconductor physics, uncontrolled impurities masked the discovery of physical laws. Experiments on pure crystals provided new insights and led to the development of semiconductor theory (effective mass, impurity states, transport). The term *doping* came up to indicate that the impurities introduced can be controlled to a certain extent. An impurity can be either a donor or an acceptor. At finite temperatures, a donor impurity may be ionized (depending on the activation energy) by donating an electron to the conduction band. An acceptor impurity captures one electron from the crystal, leaving a hole in the valence band. Donors and acceptors in semiconductors are responsible for conductivity by electrons or holes, respectively. In the energy-band diagram the donor and acceptor levels are situated in the forbidden gap close to the bottom of the conduction band or close to the top of the valence band, respectively. Although amorphous (i.e. non-periodic) semiconductors do exist, the basic approach to describe the properties of the energy bands and eigenstates of a pure semiconductor deals with a periodic potential (with periodicity of the Bravais

lattice of the crystal) and Bloch's theorem in the independent electron approximation, as a solution of the Schrödinger equation for a single electron,

$$H\psi = \left(-\frac{\hbar^2}{2m}\nabla^2 + U(\vec{r})\right)\psi = E\psi \tag{1.1}$$

where $U(\vec{r}+\vec{R}) = U(\vec{r})$ for all Bravais lattice vectors $\vec{R}$. The eigenstates ψ of the one-electron Hamiltonian H in Eq. 1.1 can be chosen to have the form of a plane wave times a function with the periodicity of the Bravais lattice:

$$\psi_{n\vec{k}}(\vec{r}) = e^{i\vec{k}\cdot\vec{r}}u_{n\vec{k}}(\vec{r}) \tag{1.2}$$

The proximity of a donor level to the bottom of the conduction band (similar reasoning for an acceptor level) implies that an excess electron is weakly bound to the donor center. The impurity center can be seen as a point charge and one can assume a central potential for the electron (or hole) motion, where

$$U(r) = \frac{1}{4\pi\epsilon_0\epsilon_r}\frac{e^2}{r} \tag{1.3}$$

with e the electron charge, r the distance of the center, and ϵ_r the dielectric permittivity of the material. This resembles the problem of a hydrogen atom, except that the product $-e^2$ of the nuclear and electronic charges has to be replaced by $-e^2/\epsilon_r$, and the free electron mass m, by the effective mass m^*. Thus the radius of the first Bohr orbit, $a_0 = \hbar^2/me^2$, becomes

$$a_0^* = \frac{m}{m^*}\epsilon_r a_0 \tag{1.4}$$

Therefore, in high dielectric constant semiconductors one could easily vary the average spacing between impurity atoms, looking for the metal-insulator transition envisioned in Mott's picture, which is based on the overlap of electronic wavefunctions. One has to consider an ensemble of hydrogen atoms positioned in a regular array (lattice). If the lattice spacing is large compared to the Bohr radius, electron wavefunctions do not significantly overlap. A finite amount of energy is necessary for electrons to hop from one site to the other due to electron-electron repulsion, better known as the Hubbard correlation energy U [11, 12, 13]. Therefore, the system is insulating at T= 0 K. In the other limit, for a lattice spacing small compared to the Bohr radius, electron wavefunctions overlap. The ground state can be described by a half-filled band and the system is a metal at T= 0 K. The system undergoes a metal-

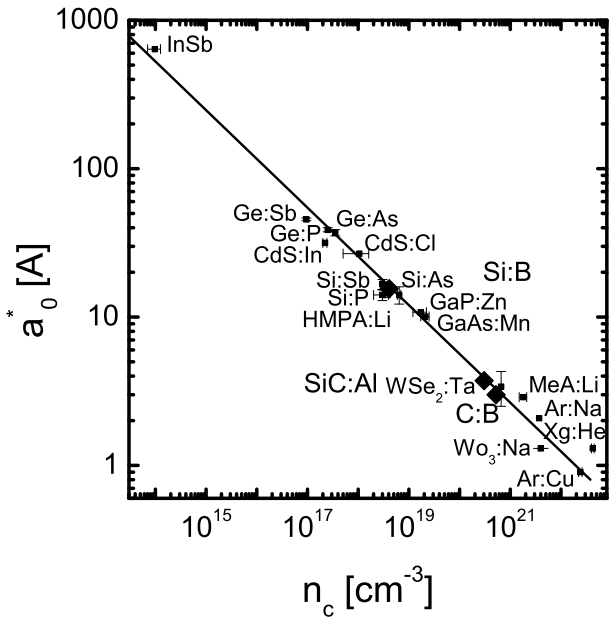

Figure 1.1.: Experimental data for the critical carrier concentration n_c and the effective Bohr radius a_0^* at the metal-insulator transition in several systems, including doped semiconductors, metal ammonia (and related systems), expanded metals, and metal-noble gas systems. Taken from Ref. 8. The theorectical values for the systems studied in this work (C:B, Si:B, and 4H-SiC:Al) are added, in good agreement with the experimentally obtained values.

insulator transition depending on the density of impurity atoms if electron correlations are taken into account. This can be applied to doped semiconductors. For weakly doped semiconductors, the electronic states at the Fermi level, if any, are localized and the transport at low temperature follows an activated behaviour. In heavily doped semiconductors the electronic states are delocalized and the transport is of metallic type.

Electronic states involved in transport are spatially extended in the metal but are localized in the insulator. On the one side, as already mentioned, this localization may be due to strong electron-electron repulsion (the so-called Mott-Hubbard transition [11, 12, 13]. On the other side, Anderson [14] has shown that localization may be due to static disorder, even in the absence of electron interactions (the so-called Anderson transition). In the case of doped semiconductors, introducing more and more impurity atoms reduces the average spacing between impurity atoms and, thus, enhances the overlap of the wavefunctions, but the random placement of the substitutional impurity

atoms also creates a certain random potential and, thus, disorder. As in many other cases of metal-insulator transitions more than one mechanism is present, each of which is quite simple in principle. But even in the limiting cases, a theoretical solution is not easy to obtain and the theoretical understanding of the metal-insulator transition is far from satisfactory.

Disregarding all of these inherent problems and complexities, there remain certain simple criteria for the occurence of a metal-insulator transition. One of these criteria is the already mentioned idea of Mott that by lowering the density of carriers, the screened Coulomb interaction gets stronger and, thus, leads to localization [5, 6, 7] of the electron wavefunction. Therefore when the carrier concentration, or equivalently the average spacing between impurity atoms, is changed, insulating states appear at a certain critical concentration n_c. Mott [5] suggested the following condition to hold:

$$n_c^{1/3} a_0^* \leq 0.25 \tag{1.5}$$

where a_0^* is the effective Bohr radius (see Eq. 1.4) and n_c is the critical carrier concentration at the metal-insulator transition at T= 0 K. Fig. 1.1 summarizes some of the experimental data including doped semiconductors (donor systems), metal ammonia (and related systems), expanded metals, and metal-noble gas systems [8]. These system all obey the linear relationship (log-log representation) of Eq. 1.5, which is truly remarkable. For acceptor systems, a single value of the effective Bohr radius a_0^* to describe the hole wave function is of questionable validity due to ambiguities associated with the hydrogenic model for the valence band holes [15]. Nevertheless, an approach to determine an appropriate value of the effective Bohr radius for acceptors is to assume a hydrogenic model and use the experimentally determined activation energy E_{act}, via the relationship

$$E_{act} = \frac{e^2}{2\epsilon_r a_0^*} \tag{1.6}$$

For boron-doped silicon Si:B with an activation energy of $E_{act} = 44\ meV$ this leads for example to a_0^* [Si:B] $= 1.55\ nm$. Therefore, the experimentally determined critical carrier concentration of $n_{c,exp}$ [Si:B] $= 4.06 \times 10^{18}\ cm^{-3}$ [16] is quite close to the theoretically predicted value of $n_{c,th}$ [Si:B] $= 4.2 \times 10^{18}\ cm^{-3}$, obtained from Eq. 1.5. Similar reasoning for boron-doped diamond ($E_{act} = 380\ meV$ [17, 18], $\epsilon_r = 5.7$) leads to $n_{c,th}$ [C:B] $= 4.3 \times 10^{20}\ cm^{-3}$ [19], quite close to the experimentally determined value of about $n_{c,exp}$ [C:B] $= 4.5 \times 10^{20}\ cm^{-3}$ in this work (see Fig. 1.1). In the case of

aluminum-doped silicon carbide, one therefore finds $n_{c,th}$ [SiC:Al] $= 3.0 \times 10^{20}\ cm^{-3}$ (using $\epsilon_r = 9.7$ and $E_{act} = 200\ meV$), also quite close to the experimentally determined interval $6.4 < n_{c,exp}$ [SiC:Al] $< 8.7 \times 10^{20}\ cm^{-3}$ of this work.

Another useful criterion is the idea of a minimum metallic conductivity, σ_{min}, that a metal can support [20, 6, 7]. This corresponds to the situation where the mean free path is equal to the de Broglie wavelength of the electrons at the Fermi energy. Mott's idea was based on arguments developed earlier by Ioffe and Regel [21] for the breakdown of the theory of electronic conduction in semiconductors. The conventional Boltzmann transport theory becomes meaningless when the mean free path l becomes comparable to the interatomic spacing d, leading to

$$\sigma_{min} = Ce^2/\hbar d \tag{1.7}$$

where the constant C can vary between 0.03 and 0.1, depending on the theoretical model used [7]. Therefore, Mott [5, 20] proposed that the metal-insulator transition in a perfect crystalline material at T= 0 K is discontinous, with a minimum metallic conductivity at the transition.

Abrahams et al. [22] have, however, predicted a continuous metal-insulator transition on the basis of a scaling theory of non-interacting electrons in a disordered system, and their results question the existence of σ_{min} [23, 24]. Low temperature conductivity data for phosphorous- and boron-doped silicon (Si:P, Si:B) can be taken as strong experimental evidence for a continuous metal-insulator transition in doped semiconductors at T= 0 K [25, 16]. At fixed (very low) temperature, the conductivity changes continuously with the dopant concentration and, in addition, the extrapolated zero-temperature conductivity $\sigma(0)$ varies continuously. Mobius [26, 27] questioned the reliability of such 0 K extrapolations and suggested that the findings did not disprove the existence of a finite σ_{min} at the transition. His analysis pointed out that while the continuous conductivity transition is predicted for non-interacting disordered electrons, just on the insulating side of the transition the Coulomb interaction is getting more important. Futhermore, it is also possible that 3 mK may not be a low enough temperature to fully probe the metal-insulator transition in doped semiconductors. Mott's minimum metallic conductivity (σ_{min}) criterion has also been criticized by Cohen and Jortner [28], who argued that there was an inhomogeneous regime near the critical concentration n_c. They suggested classical percolation theory would describe conduction along metallic channels and, thus, the zero-temperature conductivity $\sigma(0)$ would continuously drop to zero as the width of the metallic channels decreases when

one approaches n_c. Mott responded [29] that one could not divide the sample into insulating and metallic regions and gave theoretical reasons for this. The presence of a high degree of disorder may cancel the discontinuous nature of the metal-insulator transition, but the inclusion of strong correlation in scaling models could conversely change a continuous transition to a discontinuous one [30, 31].

In spite of such difficulties, however, σ_{min} continues to be a useful experimental criterion at least at the high temperature limit [9, 26, 32, 33, 34]. As pointed out by Fritzsche [35], σ_{min} appears to satisfactorily represent the value of conductivity where the activation energy for conduction disappears.

1.2. Superconductivity: General remarks

As already mentioned, conductivity values have been observed over a very wide range. The very first approaches to describe the electronic transport were based on the approximate and ideal case of the independent electron. Experimentally observed behaviours demonstrating deviations from this ideal picture were explained by more sophisticated theories including, for example, electron-electron interactions. In many metals (without magnetic ordering) a spectacular failure of the independent electron approximation sets in at very low temperature, in the electronially ordered state known today as superconducting state. The most striking features of a superconductor are the following:

1. A superconductor behaves as if it had no measurable DC electrical resistivity (below the critical current necessary to break up the superconducting ground state).

2. A superconductor behaves like a perfect diamagnet, the response to an externally applied magnetic field leading to surface currents and to the expulsion of the magnetic field (Meissner effect).

3. A superconductor behaves as if there was a gap (exception: gapless superconductors) in energy of width 2Δ centered around the Fermi energy in the set of allowed one-electron levels (directly observable in electron tunneling experiments).

Note that zero resistance alone is not a criterion for global superconductivity to occur, since a single filamentary superconducting pathway through the sample alone

leads to apparent zero resistivity by shortcircuiting the sample. Supplementary experimental evidence from a.c. susceptibility measurements indicate the expulsion of the magnetic field (no bulk superconductivity is needed). Only a measurable anomaly in specific heat measurements probes superconducting order in the bulk of the sample.

Superconductivity is not peculiar to a few metals. It appears in more than 20 of the elements (in bulk form and at ambient pressure), in thousands of alloys, in several organic conductors, in many conducting oxides (including the high T_c materials, and also in a few (doped) semiconductors.

Superconductivity was first discovered by H.K. Onnes who studied the electronic transport of mercury at low temperatures and found a jump to zero resistivity [36]. In spite of tremendous efforts, both from the experimental and the theoretical sides, the effect remained a puzzle for almost half a century, and was studied only in terms of phenomenological theories [37, 38] which held some success in accounting for some of the experimental findings but did not have microscopic theoretical justification.

The first clue towards a microscopic theory was proposed by Cooper [39], who showed that electrons can pair up in the presence of the Fermi sea, due to a phonon-mediated effective attractive interaction between them. Later on Bardeen, Cooper, and Schrieffer [40] showed that superconductivity can be understood by means of a phase-coherent, macroscopic wavefunction composed of simultaneous pairing of all the electrons in the vicinity of the Fermi surface, which is the basis of the so-called BCS theory of superconductivity. Their ideas were then followed by those of Bogoliubov [41, 42] and Gork'ov [43], which cast them within the formalism of the many-body Green's functions. Since then, superconductivity has been a central area of study in condensed matter physics, as one of the few examples in which a truly many-body quantum phenomena which comes about from electron-electron interactions, gives rise to macroscopic (and easily detectable) effects.

The BCS theory [40] was the first to successfully account for the properties of pure superconductors, as well as for alloy systems $A_{1-x}B_x$, as long as the doping concentration, x, is small [44] (see below). In its simplest form the BCS theory makes two oversimplifications in the basic Hamiltonian that describes the conduction electrons. The conduction electrons are treated in the free electron approximation and band structure effects are ignored. The rather complicated attractive interaction between electrons near the Fermi energy is further simplified to an effective interaction V_0. In reality, the complex interaction is the sum of an instantaneous Coulomb repulsion and an attractive, time-dependent electron-phonon interaction.

The most prominent characteristics that distinguishes one superconductor from an-

other is the superconductive transition temperature, T_c. Following BCS theory, in zero magnetic field, superconducting ordering sets in below a critical temperature given by

$$T_c = 0.85\Theta_D exp\left(-\frac{1}{N(E_F)V_0}\right) \tag{1.8}$$

where Θ_D is the Debye temperature and $N(E_F)$ is the density of states at the Fermi level. This expression is accurate only when $N(E_F)V_0$ is small (so-called weak coupling limit). A similar expression is predicted for the zero-temperature energy gap $\Delta(0)$. The ratio

$$\frac{\Delta(0)}{k_B T_c} = 1.76 \tag{1.9}$$

gives a fundamental formula independent of the phenomenological parameters.

Several formulations of superconductivity followed the BCS theory, the constant effective net interaction V_0 was replaced by more realistic potentials. Eliashberg [45] developed the modern expression for the superconducting gap equation, which is characterized by two parameters, λ and μ. The first corresponds to the phonon-mediated interaction which is defined as

$$\lambda = 2\int \frac{g\left(\Omega\right) F\left(\Omega\right)}{\Omega} d\Omega \tag{1.10}$$

where $g\left(\Omega\right)$ is the square of the electron-phonon matrix element and $F(\Omega)$ is the phonon density of states. μ represents the repulsive Coulomb interaction and can be written as

$$\mu = 2\int V\left(\Omega\right) d\Omega \tag{1.11}$$

McMillan [46] solved the Eliashberg equation numerically and thereby determined a semi-empirical expression for the critical temperature T_c following

$$T_c = \frac{\hbar\omega_{ln}}{1.2} exp\left(\frac{-1.04\left(1+\lambda\right)}{\lambda - \mu^*\left(1+0.62\lambda\right)}\right) \tag{1.12}$$

where μ^* is the Coulomb pseudo-potential which includes retardation effects, given by

$$\mu^* = \frac{\mu}{1+\mu\ln\left(E_F/k_B\Theta_D\right)} \tag{1.13}$$

and ω_{ln} is a logarithmically averaged frequency weighted with the electron-phonon interaction via the Eliashberg funtion $\alpha^2 F(\omega)$

$$\omega_{ln} = exp\left\{\frac{2}{\lambda}\int_0^\infty ln(\omega)\frac{\alpha^2 F(\omega)}{\omega^2}d\omega\right\} \tag{1.14}$$

Hereby, E_F is the Fermi energy. Note that for small λ Eq. 1.12 reduces to the BCS expression in Eq. 1.8 if $N(E_F)V_0$ is identified as $\lambda - \mu^*$.

As already indicated above, the starting point of the theory of disordered superconductors is due to Anderson [44], who showed that weak disorder (that is for $k_F l \gg 1$, where k_F is the Fermi wavevector and l is the mean-free path) has no profound effect on the thermodynamic properties of superconductors, leaving the energy gap Δ and the critical temperature T_c unchanged. This is because instead of Cooper-pairing of time-reversed states of opposite momenta and spin, the pairing occurs between time-reversed eigen-functions of the disordered potential, and this ground state yields a self-consistency equation for Δ which is identical to that of the clean system. As will be shown later, highly boron-doped single crystal diamond (also silicon) is compatible with the BCS theory and, thus, the disorder introduced by the impurity atoms can be considered weak in the above mentioned meaning. Therefore we shall focus only on this limit.

Obviously, disorder may also be introduced by a change in microstructure from single crystal material to poly- or nanocrystalline materials. In general, granular conductors form a class of materials with tunable electronic properties, composed of close-packed granules. Only recently progress has been made in the understanding of electronic properties of metallic granules [47]. As will be discussed later in detail, metallic granular systems are characterized by several physical quantities such as the intragranular conductance g_0, the intergranular (tunneling) conductance g, the Coulomb charging energy E_c, and the mean level spacing δ. Superconductivity can be placed in the same context, quantified by adding the superconducting gap Δ of a material of a single granule, as well as the Josephson coupling J between the grains. Anderson [44] showed that a BCS-like approach is valid for small grains, provided the average distance between levels, δ, is smaller than the superconducting gap Δ ($\delta \ll \Delta$). However, the global properties of the granular system may be significantly different from the equivalent single crystal material, depending on the interplay of the above mentioned physical quantities (e.g. one speaks of a granular system if $g \ll g_0$).

1.3. Motivation

With the breakthrough of the microscopic BCS theory, the search for new systems exhibiting superconducting properties started. Theoretical predictions for the occurence of a superconducting state in degenerate semiconductors or semimetals were made early on [48, 49, 50, 51]. One motivation for the study of degenerate semiconductors was based on the detailed informations available for the band structure, and on the effects of uniaxial strain or hydrostatic pressure [52, 53]. Therefore, superconductivity could then be observed as a function of band-structure changes and changes in the number of carriers alone [54]. In particular, it was proposed that a many-valley band structure should favor superconductivity due to additional attractive interaction by intervalley phonons [49]. Type II superconducting transitions were indeed observed in several systems like self-doped GeTe [55], SnTe, and reduced $SrTiO_3$ [56, 57], with critical temperatures in the range 50 to 500 mK. The studies included specific heat measurements as well as $H_c(T_c)$ phase diagrams [58, 59, 60]. Further investigations dealt with the dependence of the critical temperature T_c on the carrier concentration. For the two p-type materials GeTe and SnTe [61], the small increase of the critical temperature T_c at higher carrier concentration was explained by an increased screening of the attractive (valley phonon-mediated) coupling. The same argument was used in the case of n-type $SrTiO_3$ in order to explain the maximum T_c [62]. Shortly after, tunneling spectroscopy was performed at various temperatures on superconducting GeTe, leading to a ratio $2\Delta/k_BT_c$ of about 4.3 close to the theoretically predicted value of 3.5 [63]. Similar results have been obtained for $SrTiO_3$ with a ratio of about 3.3, also confirming the theoretically predicted value by BCS [64]. All these results were considered at that time to further validate the BCS theory of superconductivity. However, probably due to the discovery of other interesting systems with much higher critical temperatures T_c, superconductivity in degenerate semiconductors was not further explored. Only recently, a renewed interest was caused by the surprising discovery of superconductivity in highly boron-doped diamond by Ekimov et. al in 2004 [65].

In the general context of the metal-insulator transition in doped semiconductors and superconductivity, several systems have been studied in this work. Chapter 2 deals with highly boron-doped single crystal diamond films grown by microwave plasma assisted chemical vapor deposition (MPCVD) fabricated in our laboratory (CNRS Grenoble, Institut Néel). The metal-insulator transition in this system will be studied in some detail, and a link between the superconductivity and the proximity of the

metal-insulator transition is suggested. Several attempts have been made in order to corroborate the BCS-like nature of the superconductivity occuring in this system. Preliminary results concerning the isotopic substitution (of carbon C as well as boron B) will be presented. Furthermore, the discrepancy between the carrier concentration measured by Hall effect and the boron concentration determined from secondary ion mass spectroscopy (SIMS) will be addressed, and a possible link to the structural properties of the epilayers established.

In Chapter 3, the electronic properties of highly boron-doped nanocrystalline diamond films (MPCVD, provided by O. Williams from the IMO, Hasselt, Belgium) are studied at low temperatures. As will be seen, compared to single crystal diamond, the granularity of the nanocrystalline diamond films plays an essential role for the metal-insulator transition as well as for the superconductivity in this system.

Beside highly boron-doped diamond, two more related materials have been studied and will be presented in Chapter 4 and 5. Heavily boron-doped silicon thin films (provided by D. Débarre and J. Boulmer from the IEF, Orsay) grown by Gas Immersion Laser Doping (GILD) were carefully characterized, and the occurence of superconductivity at very low temperatures will be presented in Chapter 4.

Chapter 5 deals with the experimental observation of a doping-induced metal-insulator transition in highly aluminum-doped 4H silicon carbide (samples provided by G. Ferro from the LMI, Lyon) grown from a vapour-liquid-solid (VLS) technique.

This PhD project will be concluded by Chapter 6, where a brief outlook will be presented.

Bibliography

[1] J. Bardeen, J. Appl. Phys. **11**, 88 (1940).

[2] C. Kittel, *Introduction to Solid State Physics* (John Wiley, London, 2nd edn., 1963).

[3] N.F. Mott, Proc. Phys. Soc. **A 62**, 416 (1949).

[4] N.F. Mott, Can. J. Phys. **34**, 1356 (1956).

[5] N.F. Mott, Phil. Mag. **6**, 287 (1961).

[6] N.F. Mott, *Metal-Insulator Transition* (Taylor & Francis, London, 1974).

[7] N.F. Mott, *Metal-Insulator Transition* (Taylor & Francis, London, 2nd edn., 1990).

[8] P.P. Edwards and M.J. Sienko, Phys. Rev. B **17**, 2575 (1978).

[9] P.P. Edwards and M.J. Sienko, Int. Rev. Phys. Chem. **3**, 83 (1983).

[10] P.P. Edwards and C.N.R. Rao, *The Metallic and Non-metallic States of Matter* (Taylor & Francis, London, 1985).

[11] J. Hubbard, Proc. Roy. Soc. **A 276**, 238 (1963).

[12] J. Hubbard, Proc. Roy. Soc. **A 277**, 237 (1964).

[13] J. Hubbard, Proc. Roy. Soc. **A 281**, 401 (1964).

[14] P.W. Anderson, Phys. Rev. **109**, 1492 (1958).

[15] J.A. Chroboczek, F.H. Pollak, and H.F. Staunton, Phil. Mag. B **50**, 119 (1984).

[16] P.-H. Dai, Y. Zhang, and M.P. Sarachik, Phys. Rev. Lett. **66**, 1914 (1991).

[17] A. T. Collins, *The Physics of Diamond* (IOS Press, Amsterdam, 1997).

[18] K. Thonke, Semicond. Sci. Technol. **18**, S20 (2003).

[19] A.W. S. Williams, E.C. Lightowlers, and A.T. Collins, J. Phys. C **3**, 1727 (1970).

[20] N.F. Mott, Phil. Mag. **26**, 1015 (1972).

[21] A.F. Ioffe and A.R. Regel, Prog. Semicond. **4**, 237 (1960).

[22] E. Abrahams, P.W. Anderson, D.C. Liccardello, and T.V. Ramakrishnan, Phys. Rev. Lett. **42**, 693 (1979).

[23] P.A. Lee and T.V. Ramakrishnan, Rev. Mod. Phys. **57**, 287 (1985).

[24] T.V. Ramakrishnan, *The Metallic and Non-metallic States of Matter* (Taylor & Francis, London, 1985).

[25] G.A. Thomas, J. Phys. Chem. **88**, 3749 (1983).

[26] A. Mobius, J. Phys. C: Solid State Phys. **18**, 4639 (1985).

[27] A. Mobius, Phys. Rev. B **40**, 4194 (1989).

[28] M.H. Cohen and J. Jortner, Phys. Rev. Lett. **30**, 699 (1973).

[29] N.F. Mott, Phys. Rev. Lett. **71**, 466 (1973).

[30] N.F. Mott, Phil. Mag. B **37**, 377 (1978).

[31] N.F. Mott, Proc. Roy. Soc. A **382**, 1 (1982).

[32] C.N.R. Rao and P. Ganguly, *The Metallic and Non-metallic States of Matter* (Taylor & Francis, London, 1985).

[33] I. Shlimak and M. Kaveh, Phys. Rev. B **58**, 15333 (1998).

[34] A. Möbius, C. Frenzel, R. Thielsch, R. Rosenbaum, C.J. Adkin, M. Schreiber, H.D. Bauer, R. Grötzschel, V. Hoffmann, T. Krieg, N. Matz, H. Vinzelberg, and M. Witcomb, Phys. Rev. B **60**, 14209 (1999).

[35] H. Fritzsche, *Metal-Nonmetal Transition in Disordered Systems* (Scottish Universities Summer School in Physics, Edinburgh, 1978).

[36] H.K. Onnes, Leiden Commun. **119b**, **120b**, **122b**, **124c** (1911).

[37] F. London and H. London, Proc. Roy. Soc. A **149**, 71 (1935).

[38] V. L. Ginzburg and L. D. Landau, Zh. Eksp. Teor. Fiz. **20**, 1064 (1950).

[39] L.N. Cooper, Phys. Rev. **104**, 1189 (1956).

[40] J. Bardeen, L.N. Cooper, and J.R. Schrieffer, Phys. Rev. **108**, 1175 (1957).

[41] N.N. Bogoliubov, Zh. Eksp. Teor. Fiz. **34**, 58 (1958).

[42] N.N. Bogoliubov, Zh. Eksp. Teor. Fiz. **34**, 73 (1958).

[43] L.P. Gor'kov, Zh. Eksp. Teor. Fiz. **34**, 735 (1958).

[44] P.W. Anderson, J. Phys. Chem. Solids **11**, 26 (1959).

[45] G.M. Eliashberg, Sov. Phys. JETP **11**, 696 (1960).

[46] W.L. McMillan, Phys. Rev. **167**, 331 (1968).

[47] I.S. Beloborodov, A.V. Lopatin, V.M. Vinokur, and K.B. Efetov, Rev. Mod. Phys. **79** 469 (2007).

[48] D. Pines, Phys. Rev. **109**, 280 (1958).

[49] M.L. Cohen, Phys. Rev. **134**, A511 (1964).

[50] M.L. Cohen, Rev. Mod. Phys. **36**, 240 (1964).

[51] C.S. Koonce and M.L. Cohen, Phys. Rev. **177**, 707 (1969).

[52] E.R. Pfeiffer and J.F. Schooley, Phys. Rev. Lett. **19**, 783 (1967).

[53] P.B. Allen, Sol. State Comm. **13**, 411 (1973).

[54] J.W. Garland, Phys. Rev. **153**, 460 (1967).

[55] R.A. Hein, J.W. Gibson, R. Mazelsky, R.C. Miller, and J.K. Hulm, Phys. Rev. Lett. **12**, 320 (1964).

[56] J.F. Schooley, W.R. Hosler, and M.L. Cohen, Phys. Rev. Lett. **12**, 474 (1964).

[57] C.S. Koonce, M.L. Cohen, J.F. Schooley, W.R. Hosler, and E.R. Pfeiffer, Phys. Rev. **163**, 380 (1967).

[58] L. Finegold, Phys. Rev. Lett. **13**, 233 (1964).

[59] E. Ambler, J.H. Colwell, W.R. Hosler, and J.F. Schooley, Phys. Rev. **148**, 280 (1966).

[60] R.A. Hein and P.H.E. Meijer, Phys. Rev. **179**, 497 (1969).

[61] P.B. Allen and M.L. Cohen, Phys. Rev. **177**, 704 (1969).

[62] J.F. Schooley, W.R. Hosler, E. Ambler, and J.H. Becker, Phys. Rev. Lett. **14**, 305 (1965).

[63] P.J. Stiles, L. Esaki and J.F. Schooley, Phys. Lett. **23**, 206 (1966).

[64] G. Binnig and H.E. Hoenig, Sol. State Comm. **14**, 597 (1974).

[65] E.A. Ekimov, V.A. Sidorov, E.D. Bauer, N.N. Mel'nik, N.J. Curro, J.D. Thompson, and S.M. Stishov, Nature **428**, 542 (2004).

2. Heavily boron-doped single crystal diamond (C:B)

Diamond is the sp^3-bonded form of carbon and crystallises in a face-centered cubic crystal structure, consisting of two interpenetrating sublattices, whereby one lattice is shifted one quarter along the cube diagonal. At room temperature and ambient pressure, diamond is a metastable form of carbon. The stable form is graphite, the sp^2-bonded form of carbon. Due to its sp^2-bonded structure, graphite is electrically conductive, in contrast to intrinsic diamond. Although the standard enthalpies of diamond and graphite only differ by 2.9 kJ/mol [1], a large activation barrier separates the two phases, preventing any interconversion at ambient temperature and pressure. The very strong covalent bond is partly responsible for the unique properties of diamond. In Tab. 2.1 some of the outstanding properties of diamond are summarized and compared with those of other materials.

As can be seen from Tab. 2.1, the wide bandgap semiconductors are superior to Si in most of their properties. Key issues for industrial applications are properties like thermal conductivity, breakdown field, and electron and hole mobility. The successful application of chemical vapour deposition (CVD) to diamond growth opened up ways to large area deposition. Its simplicity, versatility and low operating costs make it an attractive technique for industrial applications. In addition, the extreme hardness of diamond, its chemical inertness, and biocompatibility make it also ideal for a large variety of applications in other domains, ranging from wear-resistive coatings to biomedical implants.

In order to make diamond a competitive material for technological applications with respect to the well established semiconductors like Si or GaAs, one has to overcome some severe problems. The use of single crystalline diamond is hindered by the lack of an inexpensive substrate for (homo-)epitaxial growth. Therefore, many efforts have been dedicated to grow high quality polycrystalline and nanocrystalline material. Nevertheless, these contain grain boundaries, twins, stacking faults, and other defects, which all reduce the lifetime and mobilities of carriers. Active devices have

Material	Band gap	Dielectric constant	Break down field	Electron mobility	Hole mobility	Thermal conductivity	Debye temperature
	$E_G[eV]$	$\epsilon(\omega = 0)$	$F_B[\frac{V}{cm}]$	$\mu_e[\frac{cm^2}{Vs}]$	$\mu_h[\frac{cm^2}{Vs}]$	$\lambda[\frac{W}{cmK}]$	$\theta_D[K]$
Si	1.12 i	11.7	3×10^5	1400	450	1.3	640
$4H - SiC$	3.23 i	9.66	$3 - 5 \times 10^6$	900	120	3.7	1300
$6H - SiC$	3.0 i	9.66	$3 - 5 \times 10^6$	400	90	4.9	1200
InP	1.34 d	12.5	5×10^5	5400	200	0.68	425
$GaAs$	1.43 d	12.9	4×10^5	8500	400	0.55	360
GaP	2.26 i	11.1	1×10^6	250	150	1.1	445
GaN	3.2 d	8.9	5×10^6	1000	350	1.3	600
$GaSb$	0.73 d	15.7	5×10^4	3000	1000	0.32	266
AlN	6.2 d	8.5	$1.2 - 1.8 \times 10^6$	300	14	2.85	1150
$Diamond$	5.47 i	5.7	1×10^7	2200	1800	22	1860

Table 2.1.: Physical properties of important semiconductors. In the band gap column i and d denote an indirect and direct band gap, respectively. The values are given, if temperature dependent, at room temperature [2].

been demonstrated using homoepitaxially grown diamond on natural or synthetic diamond substrates but, to date, there have been no affirmed reports of heteroepitaxial growth of device-quality diamond on non-diamond substrates.

Another problem for electronic device applications is the difficulty in obtaining n-type doping. P-type doping is relatively easy achieved by simply adding a small amount of boron to the CVD process gas mixture. Due to its comparable atomic size, boron can easily be introduced as an acceptor into the diamond lattice, leading to p-type conductivity with an activation energy of 370 meV. The close packing and rigidity of the diamond lattice makes doping with atoms larger than C very difficult. In the case of donors, one should not call them shallow donors. Nitrogen, the most common donor, introduces a level at 1.7 eV below the conduction band [3] and phosphorous, the shallowest of all known donors in diamond, has an activation energy of 0.6 eV [4].

Furthermore the simple crystallograpic structure as well as the absence of magnetism make single crystal diamond a likely model-system for the study of low temperature transport and electronic phase transitions.

2.1. State of the art and motivation

After the discovery of superconductivity in 2004 by Ekimov et al. in a heavily boron-doped polycrystalline diamond sample prepared by a high pressure/high temperature

process [5], this behaviour was then confirmed for heavily boron-doped polycrystalline [6, 7] and single crystalline [8] diamond films grown by microwave plasma enhanced chemical vepour deposition (MPECVD), and later on also in films prepared by a chemical transport reaction method [9], hot filament-assisted CVD [10], as well as in heavily boron-doped nanocrystalline diamond films [11]. Up to now, critical temperatures T_c up to 10 K (in a few cases) have been found [6, 10, 12, 13, 14]. The exact values not only depend on the preparation method and the conditions used for growth. The T_c value also depends on the experimental technique used to measure the superconducting transition, probably leading to overestimates in some cases. The orientation of the substrate seemed to affect superconductivity in some cases [13, 15], but a complete understanding is still lacking. Most experimental [7, 16, 17, 18, 19] and theoretical works [20, 21, 22, 23, 24] suggest a standard BCS approach involving a phonon-mediated pairing mechanism.

The diamond lattice consists of tetragonally coordinated sp^3-bonded carbon atoms (so-called σ-bonding) with very short covalent bonds which are responsible for the extreme hardness of the material and also for the high Debye temperature. It is now well understood that superconductivity in magnesium diboride MgB_2 [25] (with critical temperatures up to 39 K) comes from the very good coupling of phonons with the holes at the top of the σ-bonding bands [26, 27, 28]. Moreover, sp^3 hybridization is supposed to play an essential role for the superconductivity found in silicon-based clathrates [29, 30, 31]. While in MgB_2 the metallic bands are two-dimensional and couple to two optical phonon modes, in diamond they are three-dimensional and couple to three zone-centre optical modes. Despite a very large electron-phonon coupling potential V_0 for diamond [32, 33], the three-dimensional nature reduces its density of states $N(E_F)$ compared to MgB_2. Therefore, theoretical calculations lead to an electron-phonon coupling $\lambda = N(E_F)V_0$ of about 0.4 to 0.5 [20, 21, 22, 23, 24], quite smaller than $\lambda \approx 1$ in MgB_2, explaining the somehow smaller critical temperatures seen in diamond. Thereby, density functional theory calculations in the virtual crystal approximation (VCA) as well as supercell calculations use the calculated electronic and vibrational band structure to compute the electron-phonon spectral function (also called Eliashberg function) in order to extract the electron-phonon coupling λ. As the screening parameter μ^* is not accessible by these calculations, typical values in the range 0.1 to 0.15 have been used [20, 21, 22, 23, 24]. These values were taken either because they are typical for usual metals (note, however, that for usual metals the relation $E_F/k_B\Theta_D \gg 1$ holds), or were in good agreement with experimentally observed critical temperatures T_c (related to λ and μ^* by the McMillan formula [34]). While

VCA calculations point toward a coupling of the valence electron by optical phonon states at the centre of the Brioullin zone (due to symmetry) [20, 21, 22], supercell calculations indicated the importance of localized vibrational modes related to boron atoms to the overall electron-phonon coupling [23, 24], which has been confirmed recently including disorder-related effects [35]. However, theoretical calculations predict a doping dependence of the critical temperature T_c which is not reproduced experimentally, so the BCS-type estimate of this critical temperature is not an evidence for a BCS mechanism. Application of a recently developed parameter-free approach where the Coulomb potential μ^* has not to be adjusted [36] should be applied to the diamond case to further corroborate the BCS mechanism or not.

In order to prove the application of a BCS theoretical approach for the superconductivity in highly boron-doped diamond, effects of isotopic substitution with direct influence on the vibronic energies and, thus, the electron-phonon coupling, on the critical temperature T_c should be studied. These experiments are difficult to perform, a first approach will be discussed in Sec. 2.4. Beside this, measurements of the superconducting band gap 2Δ reveal the compatibility to the BCS theory. Below the critical temperature T_c, a gap (2Δ) centered around the Fermi level opens up in the density of states. This has been observed by point contact tunneling spectroscopy [37], by optical reflectance in the far infrared [18], by laser-excited photoemission spectroscopy [38], and by scanning tunneling spectroscopy [17, 39, 40, 41]. For experiments carried out at temperatures close to the critical temperature T_c, a V-shaped gap has been observed for single crystal diamond ({100} [37] and {111} [38] orientation) as well as for polycrystalline diamond [40]. Scanning tunneling spectroscopy measurements carried out at much lower temperatures give evidence of a standard BCS lineshape [17, 39]. Fig. 2.1(a) shows the temperature dependence of the energy gap, and a ratio of $2\Delta/k_BT_c$ of about 3.5 very close to the BCS value in the weak coupling limit through phonons was deduced from this temperature dependent spectroscopy [17, 41]. The scanning tunneling spectroscopy measurement in Fig. 2.1(b) shows the vortices obtained in highly boron-doped diamond, clearly revealing the type II nature of superconductivity in this system.

Moreover, electron-phonon coupling is expected to soften specific vibrational modes (phonon softening), which has been studied by inelastic X-ray scattering (IXS) on a free-standing 100 μm thick polycrystalline sample [42, 43]. The IXS data collected along the direction {100} and {111} of the Brillouin zone indicate that the softening is most pronounced at the zone center Γ point, much smaller than values predicted by VCA calculations but in good agreement with supercell calculations. Cardona

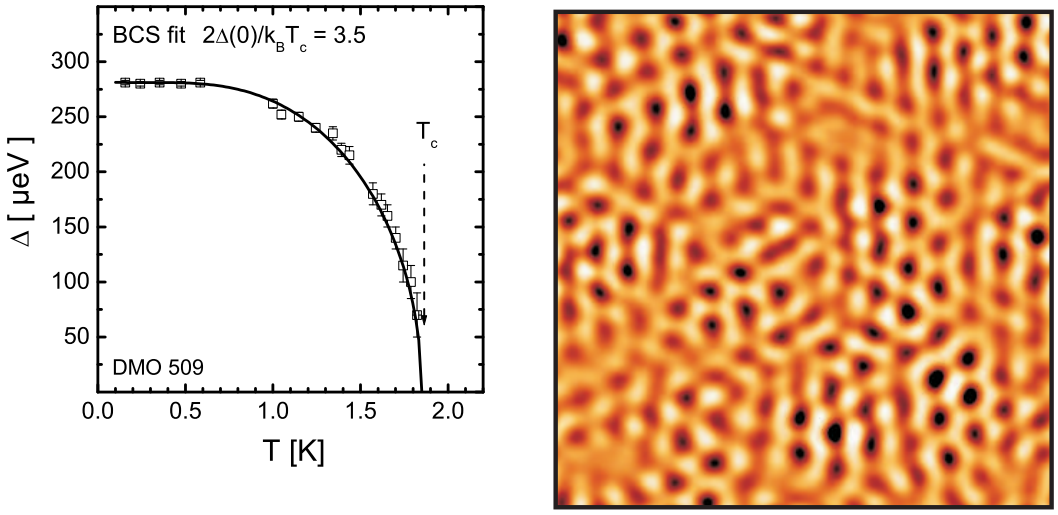

(a) (b)

Figure 2.1.: (a) Temperature dependent scanning tunneling spectroscopy measurements of the energy gap opening up in the superconducting state. Results are in very good agreement with the expected BCS values [17, 68]; (b) Vortex image obtained on a highly boron-doped single crystal diamond sample, clearly showing the type II nature of superconductivity [17, 68].

et al. suggest [32, 33] that the {110} direction is energetically favoured for carrier population. A detailed analysis of IXS data collected on homoepitaxial thick (25 μm) layers grown by us (throughout the Brillouin zone) is underway in order to confirm and complement existing results [42, 43], which can be compared to results from second order Raman scattering. A strong phonon softening is expected in the case of a spheroid Fermi surface where energy-conserving phonon scattering is possible. IXS data indirectly confirm the electronic structure of metallic diamond films. Supercell calculations indicate that the electronic band structure of highly boron-doped diamond differs only slightly from that of undoped diamond, doping inducing a rigid shift of the Fermi level into the diamond valence band (degenerate metal) [23, 44]. This was confirmed experimentally by angular resolved photoemission spectroscopy (ARPES) [16]. The Fermi level is situated in the diamond valence band, indicating a well-defined spheroid (to first order) Fermi surface around the Γ point, in agreement with supercell calculations.

Phase diagrams of the critical magnetic field H_c versus the critical temperature T_c indicate that highly boron-doped diamond is a type II superconductor [5, 6, 8]. This was further confirmed by scanning tunneling spectroscopy measurements at low tem-

perature clearly showing vortices arranged in a so-called Abrikosov lattice [17]. The coherence length ξ has been estimated either from the low temperature part of the phase diagram or from the slope dH_{c2}/dT at small fields close to the critical temperature T_c. Accordingly, a coherence length ξ of about 10 nm was found for polycrystalline HPHT bulk diamond [5], 10 to 30 nm for polycrystalline MPCVD diamond films [7], and 15 to 20 nm for {100}-oriented single crystal MPCVD diamond films [8, 37]. Similar values have been obtained in this work. Winzer et al. estimated the mean free path l from conductivity and Hall effect measurements carried out at 4.2 K and found $l \approx 0.5$ nm < 10 nm $= \xi$. Together with the estimated London penetration length λ_L fo 150 nm, one clearly sees $l \ll \xi \ll \lambda_L$, indicating that superconducting diamond is in the dirty limit [7]. This was further confirmed by ARPES measurements revealing small values of the mean free path $l \approx 0.5$ and 0.9 nm [16], and infrared spectroscopy leading to $l \approx 2.5$ and 4 nm much smaller than the coherence length ξ [8, 37] as well as $\lambda_L \approx 50$ nm [18] comparable to the value estimated by Winzer et al. [7].

As already mentioned, the discovery of superconductivity in highly boron-doped diamond initiated a lot of experimental and theoretical efforts. The confirmation of superconducting properties of samples (from single crystal to poly- and nanocrystalline films) grown by several different growth techniques shows the robustness of this effect. However, the nature of the superconductivity and the compatibility with the BCS theory still remain to be confirmed. In this context, this Chapter is divided as follows: in Sec. 2.2 we report on the structural properties and growth conditions of our homoepitaxial samples. Sec. 2.3 deals with the doping-induced metal-insulator transition in highly boron-doped single crystal diamond. All metallic samples also show superconducting properties, and a link between these two topics is suggested based on a scaling theoretical approach of the metal-insulator transition. In Sec. 2.4 we discuss preliminary results obtained on isotopically substituted samples in order to provide further information about the pairing mechanism in highly boron-doped diamond. Finally, Sec. 2.5 is devoted to the puzzling situation concerning the Hall effect in highly boron-doped single crystal diamond. In some cases, the carrier concentration determined by Hall measurements exceeds the boron concentration measured by secondary ion mass spectroscopy (SIMS) by a factor up to 10.

2.2. Sample preparation and structural properties

As already mentioned, diamond is said to be metastable, that is kinetically stable but not thermodynamically stable. Therefore, knowledge of the conditions under which natural diamond is formed suggests that diamond can be obtained by heating carbon under very high pressure (see Ref. 45 and references therein). This process forms the basis of the high-pressure/high-temperature (HPHT) growth technique (up to 15 GPa and 3000 K), first adapted by General Electric Company in 1955 for industrial production [46]. Presence of a suitable metal catalyst (e.g. Ni or Co) reduces the necessary growth pressure and temperature to 7 GPa and 2000 K, respectively (see Fig. 2.2(a)). The diamond crystals thus produced are limited in size (a few millimeters), and are mostly used for industrial processes which take advantage of the hardness and wear resistance properties of diamond, such as cutting and machining tools and the polishing and grinding of optics.

A breakthrough towards large area deposition was achieved by the successful application of chemical vapour deposition (CVD) to diamond growth [47, 48, 49, 50, 51, 52, 53]. The technique generally involves growing a solid from a reactive gas mixture which supplies the necessary active species (carbon in the case of diamond) onto a controlled surface (substrate), as can be seen schematically in Fig. 2.2(b). The gas mixture passes through an activation region (most commonly used: hot filament or microwave plasma) which provides energy. This causes molecules to fragment into reactive radicals and atoms. These reactive fragments continue to mix and complete a complex set of chemical reactions before reaching the substrate surface. At this point the species either adsorb and react with the surface, desorb again back into the gas phase, or diffuse around close to the surface until an appropriate reaction site is found. If surface reaction occurs, one possible process, if all the conditions are suitable, is the growth of diamond. In contrast to HPHT, CVD is generally used at or below ambient pressure (in our case 30 to 50 Torr).

Diamond synthesis advanced in the late 1960s, when J. Angus' group discovered that the presence of atomic hydrogen during the deposition process would lead to preferential etching of the graphite, rather than diamond [48]. Normal conditions for diamond growth in a CVD process involve a precursor gas (usually CH_4) which is highly diluted in hydrogen. The substrate is held at temperatures above 500 °C, in order to provide a high mobility of the radicals on the substrate surface. A number of studies have been performed to try to identify the growth species [54], and the general consensus is now that methyl, CH_3, is the important radical. Gas phase hydrogen

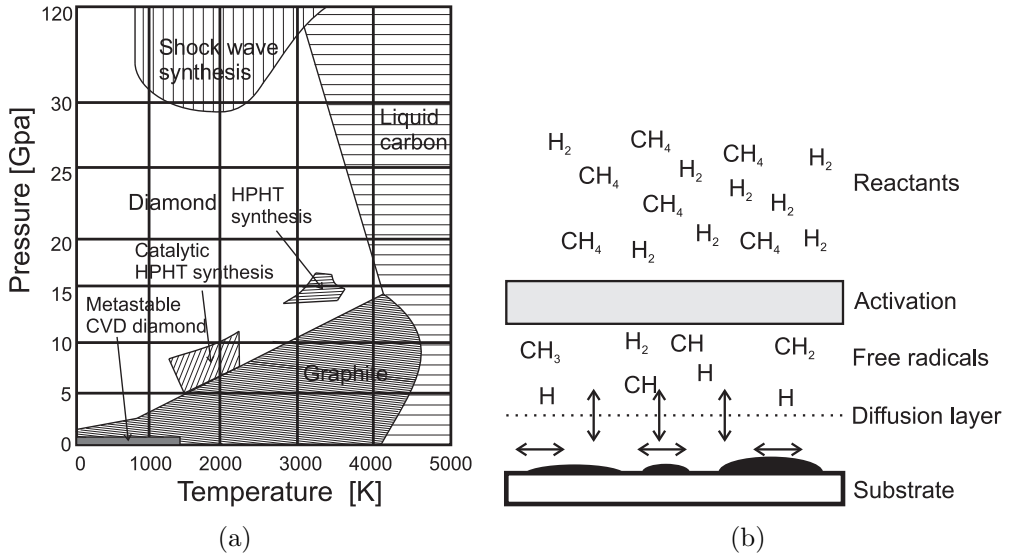

Figure 2.2.: (a) Thermodynamic phase diagram for the growth of diamond; (b) Schematic description of the processes involved in CVD growth of diamond.

atoms play a crucial role during growth of CVD diamond (see Fig. 2.2(b)). They undergo H abstraction reactions with stable gas-phase hydrocarbon molecules, producing highly reactive carbon-containing radical species. This is important, since stable hydrocarbon molecules do not react to cause diamond growth. The reactive radicals, especially methyl, CH_3, can diffuse to the substrate surface and react, forming the C-C bond necessary to build the diamond lattice. Furthermore, H-atoms terminate the 'dangling' carbon bonds on the growing diamond surface and prevent them from cross-linking, thereby reconstructing it into a graphite-like surface. As already mentioned, atomic hydrogen etches both diamond and graphite but, under typical CVD conditions, the rate of diamond growth exceeds its etch rate whilst for other forms of carbon (graphite, for example) the opposite is true. This is believed to be the basis for the selective preferential deposition of diamond.

Fig. 2.3 shows a schematic view of the growth chamber used for this work. This MPCVD growth chamber was built up by E. Gheeraert [55] and P. Gonon [56], principally based on the model of a japanese prototype used at NIRIM (National Institute for Research on Inorganic Materials) by Kamo et al.[52]. The growth chamber consists of an inner and an outer fused silica (quartz) tube, the sample holder is placed on the inner quartz tube at the intersection with the waveguide. A microwave plasma generator (Metal Process model G2V2) operating at a standard frequency of 2.45 GHz supplies an adjustable microwave power in the range of 0 to 2000 W. The horizontal position of the plasma can be adjusted by the hollow-faced piston (standing wave tun-

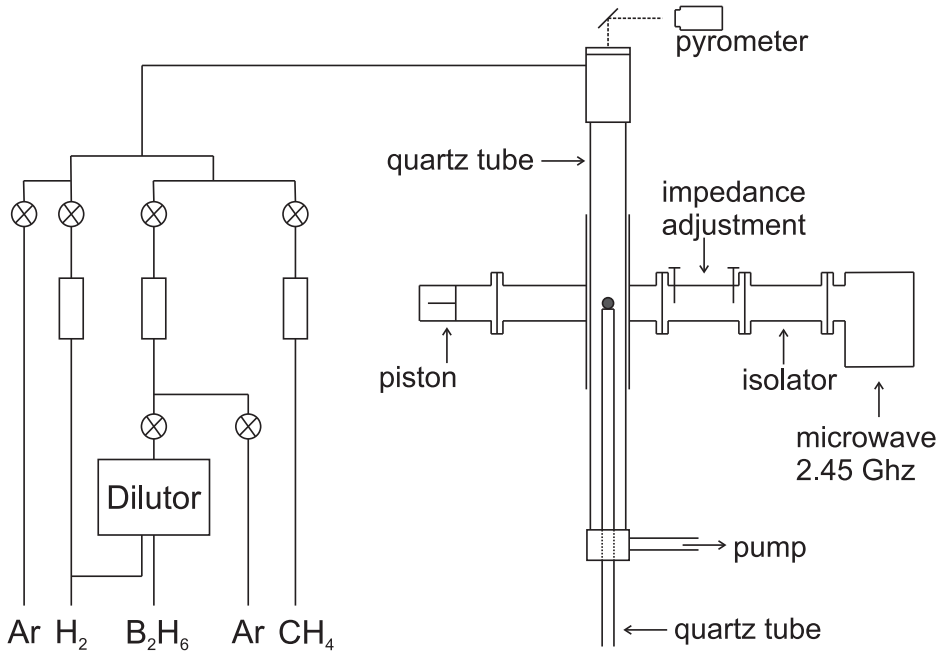

Figure 2.3.: Schematic description of the MPCVD growth chamber used for the elaboration of highly-doped single crystal diamond epilayers at the Institut Néel, CNRS Grenoble, France.

ing), the reflected power (water cooled with the isolator) can be minimized by adapting the impedance. The growth chamber is connected to a pump system at the lower part, consisting of a primary pump and a high vacuum turbo pump. While the primary pump is used for the circulation of the gas mixture, the secondary pump ensures a base pressure below 10^{-5} Torr before introduction of the gas mixture and therefore prevents incorporation of other impurities. A single wavelength optical pyrometer is used for reading the temperature. The sample holder consists of a $1 \times 1\ cm^2$ silicon piece overgrown with non-intentionally doped polycrystalline diamond (in order to avoid incorporation of silicon from the sample holder as impurity during growth). The emission of the silicon substrate holder in the infrared, corrected by the transmission through the optical window, is collected by the pyrometer, using an effective emissivity of 0.4.

Several features have been added to the growth chamber in order to optimize the quality of the grown layers. From March 2004 on, a dilutor has been installed which allows to control the concentration of B_2H_6 in the gas mixture with a higher precision compared to formerly grown samples. This has significantly improved the reproducibility of the samples, and, furthermore, the three-stage dilution system is also suited to the growth of very weakly-doped layers with boron concentrations of the order of

10^{15} cm^{-3}. In november 2005, a gas purifier was installed on the hydrogen line (N60). The purity of hydrogen (main gas source during growth) is now better than 99,9999 % which limits the presence of impurities like water or nitrogen considerably. As will be seen later, the efficiency of boron incorporation increases when hydrogen is purer. Methane and diborane are not filtered, but their purity is claimed by the supplier to be 99,9995 % (N55).

One purpose of this work is to compare the physical properties of formerly grown samples with the growth direction {100} which have been grown before the installation of the dilutor and the hydrogen purifier with samples grown under ameliorated conditions. In addition to the growth direction {100}, also samples along directions {111} and {110} have been grown. The main steps concerning the sample growth are the substrate preparation and the growth conditions adapted for homoepitaxial growth, including parameters controlling the gas flow, the substrate temperature, the total pressure, etc.. Growth was realized on commercially available HPHT type Ib substrates provided by Sumitomo (Japan). Depending on the growth direction, the type Ib substrates had dimensions $3 \times 3 \times 0.3$ mm for {100}, $2 \times 2 \times 0.3$ mm for {111}, and $2.5 \times 2.5 \times 0.3$ mm for {110}, in contrast to the formerly grown samples for which the thickness of the substrate was 0.5 mm. The substrates have been polished by Sumitomo, the miscut varies from $< 0.3°$ for {100}, $< 3°$ for {111}, up to $\approx 8°$ for {110} substrates.

In order to minimize the amount of impurities on the substrate surface for the growth, a standardized cleaning process was used, consisting of the following steps:

1. The first step consists of consecutive ultrasonic cleaning of the substrate with 100 % acetone and ethanol (each up to 10 minutes), and a subsequent rinse under deionized water (18 $M\Omega$), in order to remove impurities of organic and lipophilic character.

2. The next step consists of an acid treatment for removal of impurities of metallic and organic nature. During two hours, the substrate is etched by a mixture of oxidizing acids ($HClO_4 : H_2SO_4 : HNO_3$) with volume proportions 1 : 3 : 4 at a temperature of about 100°C, followed by another mixture of $HF : HNO_3$ with oxidizing and reducing nature during 1 hour at the same temperature of 100°C. In between the two mixtures, extensive rinsing with deionized water is necessary.

3. A final rinsing step with deionized water with subsequent drying (nitrogen pistol) is necessary before one can put the substrate into the growth chamber.

In Tab. 2.2 the generally used growth procedure and conditions are summarized for the growth directions {100} and {111}. Before growth, the boron concentration of the gas mixture was carefully prepared with help of the dilutor. Then, at first, the

Growth direction	{100}	{111}
Hydrogen plasma		
Temperature [$°C$]	880	900
Pressure [$Torr$]	30	50
Gas flow H_2 [$sccm$]	100	200
Duration	2h00	0h30
Non-intentionally doped layer		
Temperature [$°C$]	830	900
Pressure [$Torr$]	30	50
CH_4/H_2 [%]	0.25	0.15
Duration	1h00	0h20
Boron-doped layer		
Temperature [$°C$]	830	900
Pressure [$Torr$]	30	50
CH_4/H_2	4	0.15 - 0.6
B/C [ppm]	100 - 2500	500 - 6000
Duration	0h40 - 24h00	0h10 - 3h30

Table 2.2.: Growth conditions used for the elaboration of highly boron-doped single crystal diamond at the Institut Néel, CNRS Grenoble, France.

substrate was treated by a hydrogen plasma as a final in situ cleaning step at about 900°C for a duration of 30 up to 120 minutes (depending on the growth direction, see Tab. 2.2). This was also used to stabilize the temperature and pressure of the growth chamber before introduction of the gas mixture for growth. Then, a non-intentionally doped buffer layer is grown in order to reduce the translation of defects from the substrate into the grown layer, and to adjust the lattice mismatch between the substrate and the boron-doped layer. The growth conditions for the buffer layer are shown in Tab. 2.2. Subsequently, the boron-doped epilayer is grown, with the appropriate growth conditions seen in Tab. 2.2. In general, the growth rate depends not only on the substrate orientation (higher growth rates for {111}-oriented substrates under similar condition), but also on the CH_4/H_2 ratio used for growth. The value $CH_4/H_2 = 4$ % was chosen for {100}-oriented growth in order to get acceptable values for the growth rate of about $1\mu m/h$.

In the case of highly-doped diamond films, the high resolution X-ray diffraction peaks from the substrate and the boron doped homoepitaxial films can be distinguished, as can be seen in Fig. 2.4 (for symmetrical reflection (004) and (111)). The spectra for formerly grown samples (DMO and CN series) are compared with spectra

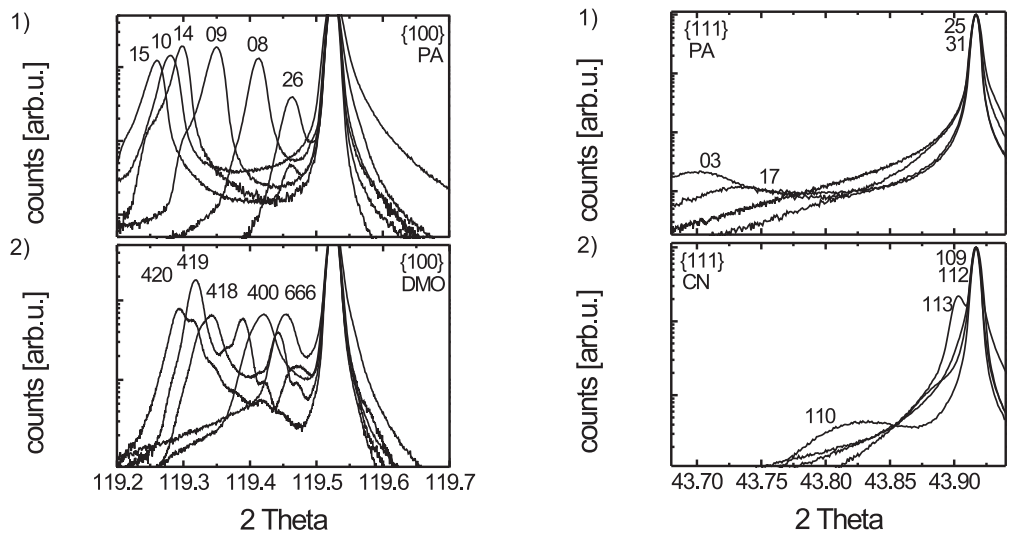

(a) (b)

Figure 2.4.: (a) (b) High resolution X-ray diffraction spectra obtained for highly-doped diamond films along the (004) or (111) Bragg reflection, respectively. Formerly grown sample (DMO or CN in (2)) are compared with the more recently grown samples (PA in (1)) under improved conditions.

on recently grown samples (PA) for the growth directions {100} and {111}, respectively. One clearly sees the better quality of the recently grown samples with respect to the FWHM of the diffraction peaks and the uniformity of the spectra.

In Fig. 2.5 a typically obtained reciprocal space map of an (100)-oriented homoepitaxial epilayer is presented. Reciprocal space mapping compares the shape and position of the film and substrate reciprocal lattice points and gives information such as layer tilt, strain, relaxation, lattice parameter, and mosaicity. The intensity contours show the symmetrical diffraction peak originating from the epilayer and from the diamond substrate. The boron-doped diamond epilayer shows no tilt with respect to the diamond substrate, confirming the coherent growth. The width of the rocking curve along the vertical axis (ω-scan) shows that the mosaicity of the HPHT type Ib substrate is maintained in the epilayer. The lineshape along the horizontal axis ($2\Theta - \omega$-scan) representing the strain distribution, becomes somewhat larger in the epilayer.

Recently, in order to get information not only along the symmetrical growth axis {100}, but also on planes inclined to the sample surface, reciprocal space maps around so-called asymmetric reflections have been performed. This is particularly important

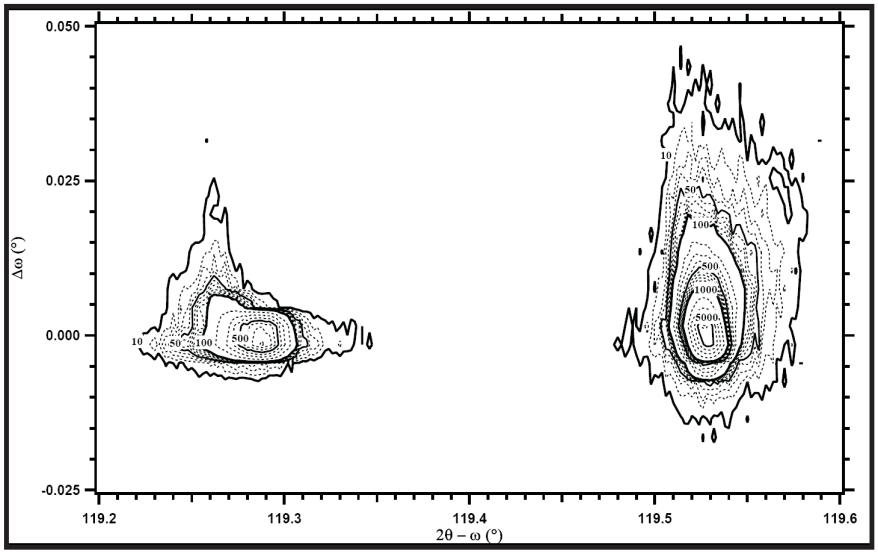

Figure 2.5.: Reciprocal space map of an (100)-oriented homoepitaxial epilayer for the (004) Bragg reflection. The mosaicity of the HPHT type Ib substrate is maintained in the epilayer, the strain distribution becomes larger in the epilayer.

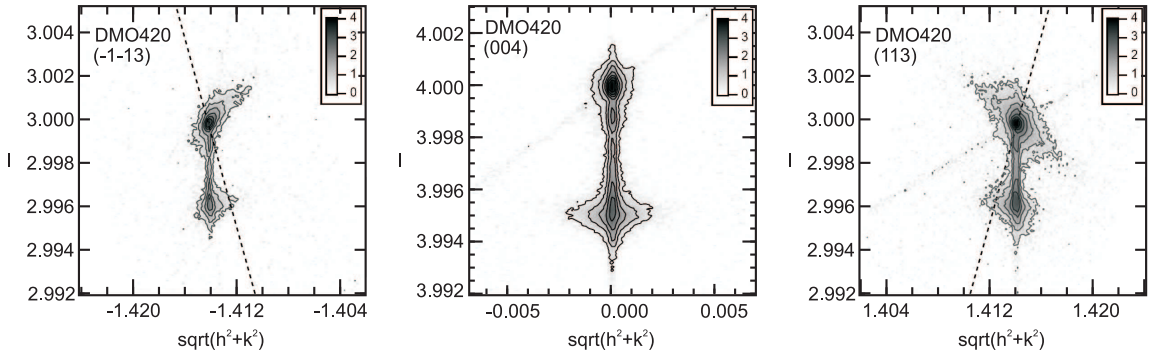

(a) (b) (c)

Figure 2.6.: Reciprocal space maps of sample DMO420 around the asymmetric reflections $\{\bar{1}\bar{1}3\}$ ((a)) and $\{113\}$ ((c)), as well as the symmetric reflection $\{004\}$ ((b)), indicating the in-plane lattice matching and the constrained growth of the epilayer.

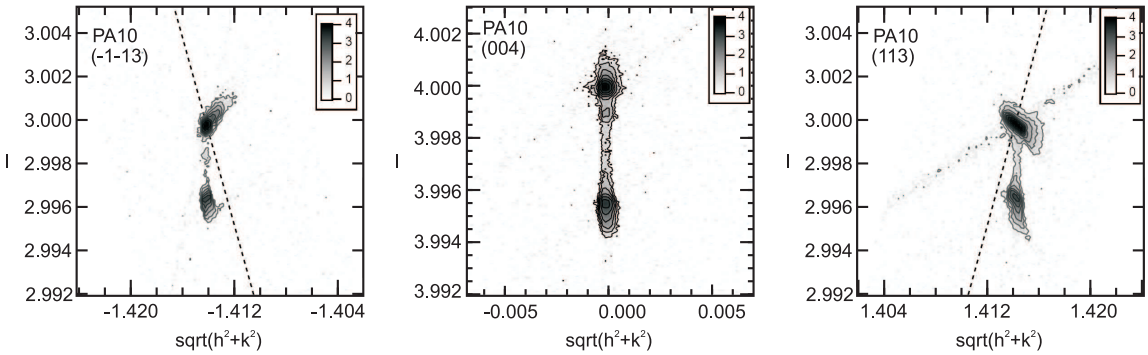

(a) (b) (c)

Figure 2.7.: Reciprocal space maps of sample PA10 around the asymmetric reflections $\{\bar{1}\bar{1}3\}$ ((a)) and $\{113\}$ ((c)), as well as the symmetric reflection $\{004\}$ ((b)), indicating the in-plane lattice matching and the constrained growth of the epilayer.

to obtain information about whether or not the epilayer has grown under relaxed or constrained conditions, as one can probe the in-plane lattice parameter change. In general, the position of a given reciprocal lattice point is specified by (h, k, l). These reciprocal lattice points can be separated into symmetric reflections with planes parallel to the surface and otherwise asymmetric reflections. In the following, we focus on samples oriented along $\{004\}$ and, thus, the symmetric reflections are described by $h = k = 0$ and $l \neq 0$ and the asymmetric reflections with general (h, k, l) values. In Fig. 2.6 and Fig. 2.7, reciprocal space maps are shown for both samples DMO420 and PA10, respectively, along the symmetric reflection $\{004\}$ as well as on the asymmetric reflections $\{113\}$ and $\{\bar{1}\bar{1}3\}$, respectively. (ω)-scans and $(2\Theta{-}\omega)$-scans were performed after alignment in the vicinity of these reflections. Hereby, the $(\omega, 2\Theta)$ data have been converted using

$$Q_{\parallel} = sin(\Theta)sin(\Theta - \omega) \tag{2.1}$$

$$Q_{\perp} = sin(\Theta)cos(\Theta - \omega) \tag{2.2}$$

where $Q_{\parallel}$ and $Q_{\perp}$ are related via

$$Q_{\parallel} = \frac{\lambda}{2a_{\parallel}}\sqrt{h^2 + k^2} \tag{2.3}$$

$$Q_{\perp} = \frac{\lambda}{2a_{\perp}}l \tag{2.4}$$

with $a_{\parallel}$ and $a_{\perp}$ the in-plane and out-of-plane lattice constant, respectively, and λ the used wavelength. When a thin film is deposited on a substrate, the film lattice may

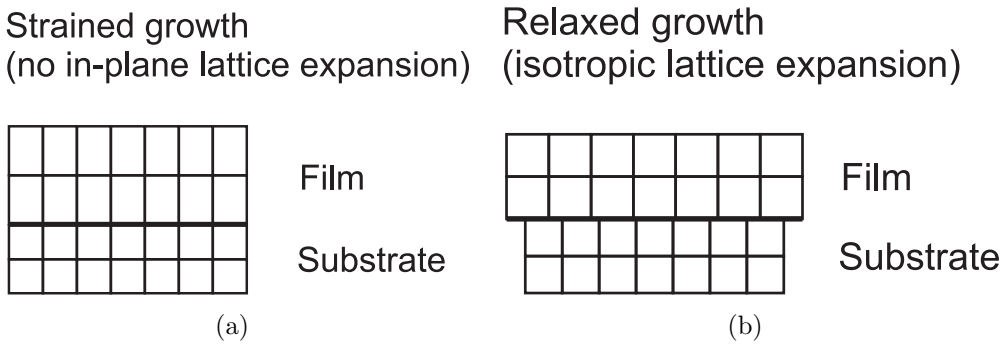

Figure 2.8.: Coherent growth of the epilayer on the substrate results either in (a) strained growth (with in-plane lattice matching) or (b) to relaxed growth (in-plane strain relaxed due to misfit dislocation).

be constrained to coincide with the substrate lattice (fully strained) or the film lattice may be completely free of the substrate lattice (fully relaxed). In our samples, data along the asymmetric reflection {113} and $\{\bar{1}\bar{1}3\}$, respectively, taken for the substrate and the epilayer, lie vertically above each other in reciprocal space. This indicates the matching of the in-plane lattice constant with the substrate. The dashed lines in Fig. 2.6 and Fig. 2.7 correspond to a radial line representing the fully relaxed case. A quantitative analysis of the in-plane lattice parameter is underway.

So, if one assumes that all epilayers grow coherently on the substrate (as shown above for two of them), that is without misfit dislocation which would relax the in-plane strain, the films are under perpendicular strain ($\delta a^{\perp}/a$), as is shown schematically in Fig. 2.8(a) in contrast to relaxed growth shown schematically in Fig. 2.8(b). The introduction of substitutional boron into diamond leads to an expansion $\delta a/a$ of the lattice parameter due to larger covalent radius of boron ($r_B = 0.088\ nm$) compared to that of carbon ($r_C = 0.077\ nm$). The measured lattice parameters $a^{\perp}_{epi}$ have to be corrected in order to calculate those of the epilayers in the relaxed state a_{epi}. Assuming that the epilayer is much thinner than the substrate, strain in the substrate can be neglected. By taking into account the strongly anisotropic elasticity of diamond, one gets for the lattice parameter in the relaxed state [57, 58] (depending on the substrate orientation)

$$\frac{\delta a}{a_{sub}} = \frac{a_{epi} - a_{sub}}{a_{sub}} = \frac{a^{\perp}_{epi} - a_{sub}}{a_{sub}} \frac{c_{11}}{c_{11} + 2c_{12}} = \gamma_{100} \frac{a^{\perp}_{epi} - a_{sub}}{a_{sub}} \quad \{100\} \tag{2.5}$$

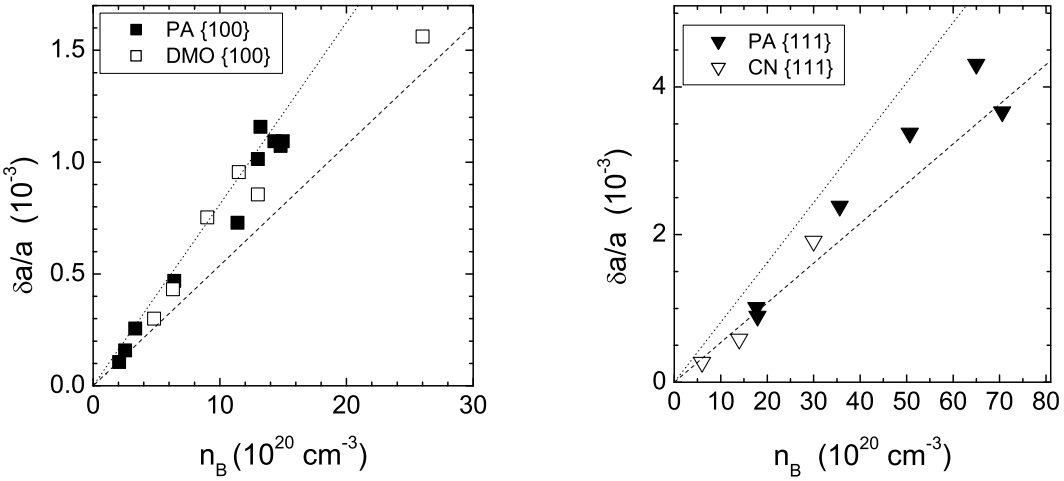

(a) (b)

Figure 2.9.: Calculated change of the lattice parameter in the relaxed state ($\delta a^{\perp}/a_{sub}$) with respect to the boron concentration n_B as determined from secondary ion mass spectroscopy (SIMS) (see Tab. 2.3 to 2.6) for the two growth directions {100} (a) and {111} (b), respectively, and for formerly grown samples (DMO and CN) and recently grown samples (PA).

$$\frac{\delta a}{a_{sub}} = \frac{a_{epi} - a_{sub}}{a_{sub}} = \frac{a_{epi}^{\perp} - a_{sub}}{a_{sub}} \frac{c_{11} + \frac{2}{3}C}{c_{11} + 2c_{12}} = \gamma_{111} \frac{a_{epi}^{\perp} - a_{sub}}{a_{sub}} \quad \{111\} \tag{2.6}$$

where c_{11}, c_{12}, and c_{44} are the elastic constants and $C = 2c_{44} - c_{11} + c_{12}$. In the case of diamond [59], $\gamma_{100} = 0.8113$ and $\gamma_{111} = 0.9136$. The perpendicular strains $a_{epi}^{\perp}/a_{sub}$ can be determined from the angle separation ($\Delta\Theta = \Theta_{sub} - \Theta_{epi}$) between the peak position of the diamond substrate Θ_{sub} and the boron-doped epilayer Θ_{epi} by

$$\frac{\delta a^{\perp}}{a_{sub}} = \frac{a_{epi}^{\perp} - a_{sub}}{a_{sub}} = \frac{\Delta\Theta}{tan(\Theta_{sub})} \tag{2.7}$$

The theoretical value of the peak position of the diamond substrate Θ_{sub} can be calculated using the Bragg condition

$$2d_{hkl}sin(\Theta_{hkl}) = n\lambda \quad with \quad d_{hkl} = \frac{a}{\sqrt{h^2 + k^2 + l^2}} \tag{2.8}$$

where a is the diamond lattice constant, $\{h, k, l\}$ the Miller indices of the diffraction planes, and λ the wavelength of the x-rays (see App. A.2). Therefore one gets $2\Theta_{100} =$

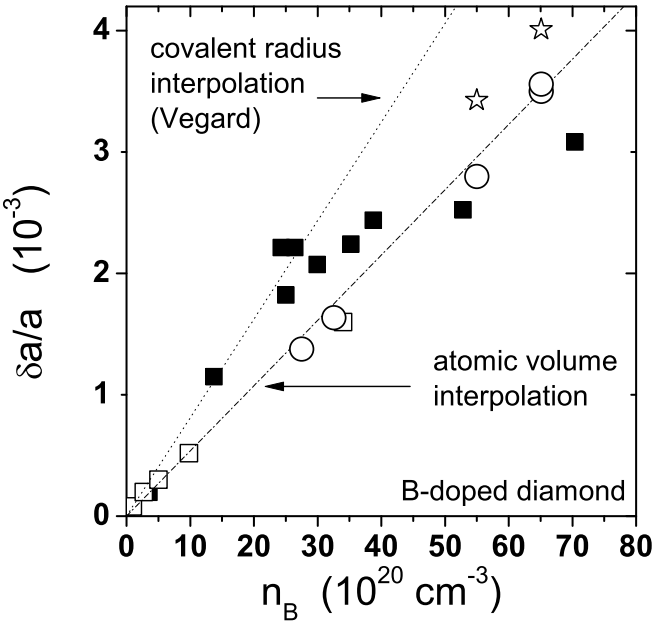

Figure 2.10.: Lattice parameter expansion as a function of the boron atomic density in C:B alloys. Full squares refer to XRD results published in Ref. 62 about HPHT crystals, and open squares to relaxed values deduced in Ref. 61 from XRD analysis of (100)-oriented epilayers grown by MPCVD. Other open symbols correspond to the results of ab initio calculations on supercells where either isolated boron atoms (circles) or boron pairs (stars) substituted carbon atoms. The straight lines are linear interpolations corresponding to randomly substitutional (dotted) and non substitutional or clustered (dash-dotted) incorporation of boron in diamond.

119.526 and $2\Theta_{111} = 43.917$.

The calculated change of the lattice parameter in the relaxed state ($\delta a^{\perp}/a_{sub}$) are shown in Fig. 2.9 with respect to the boron concentration n_B as determined from secondary ion mass spectroscopy (SIMS) (see Tab. 2.3 to 2.6) for the two growth directions {100} and {111}, respectively, and for formerly grown samples and recently grown samples. As already mentioned, as a result of the larger covalent radius of boron ($r_B = 0.088\ nm$) compared to that of carbon ($r_C = 0.077\ nm$), the introduction of boron into diamond leads to an expansion of the lattice parameter. Vegard [60] assumed that the cumulated difference between the covalent radii of the dopant and host atoms are uniformly distributed over all sites and induces a linear variation of the lattice parameter with the (in our case) boron concentration following

$$\frac{\delta a}{a} = \frac{r_B - r_C}{r_C n_C} [B] = \beta_{size} [B] \tag{2.9}$$

where n_C is the atomic density of diamond, i.e. $1.76 \times 10^{23} cm^{-3}$, leading to a numerical value of $\beta_{size} = 8.12 \times 10^{-25} cm^3$. In the case of (100)-oriented growth (Fig. 2.9(a)), the calculated values lie between two linear interpolations, with a high proportion of samples following Vegard's law up to about 1 at. %, corresponding to a higher value than previously reported [58, 61]. At higher boron concentrations, a weaker expansion has been reported, which can be attributed to the contribution of free holes and to the negative deformation potentials at the valence band maximum, or to the occurence of boron pairs or clusters. The weakening of the lattice expansion due to interstitial and/or aggregated incorporation of boron has been studied recently [62]. The weighted average of the specific atomic volumes of C (5.67 $Å^3/atom$) and B (7.28 $Å^3/atom$) results (in first order) in a linear variation of the type

$$\frac{\delta a}{a} = \beta_{vol} [B] \tag{2.10}$$

with $\beta_{vol} = 5.38 \times 10^{-25} cm^3$ [62], which corresponds to the lower linear interpolation in Fig. 2.10. More recently, ab initio calculations have been used to demonstrate the influence of substitutional isolated boron atoms as well as boron pairs on the lattice expansion [63]. As has been reported previously, at high boron concentrations the formation of boron pairs (B_2 dimers) are energetically favoured compared to interstitial incorporation or formation of B_n clusters [44]. Furthermore, these B_2 dimers are electrically inactive and do not contribute free holes as isolated boron atoms do. As can be seen in Fig. 2.10, the lattice expansion due to B_2 dimers (stars in Fig. 2.10) is lower than predicted by Vegard, and is found to be compatible with a linear expression of the type

$$\frac{\delta a}{a} = \beta_{pair} [BB] \tag{2.11}$$

with $\beta_{pair} = 12.4 \times 10^{-25} cm^3$ [63]. This contribution alone does not suffice to explain the low expansion values at high boron concentrations. An additional term from a free carrier contribution was first suggested by Bardeen and Shockley [64] and introduced by Yokota [65] through deformation potentials at the edge of the valence and conduction bands to describe the dependence with the high doping levels of the semiconductor lattice constant. Hereby, the lattice parameter corresponds to the minimum value of the total energy of the semiconductor, which includes an electronic component

from the variation of the free carrier concentration and an elastic component from that of the cell parameter. This corresponds to the contribution of isolated substitutional boron atoms (open circles in Fig. 2.10) which are electrically active and contribute free holes, leading to a depletion of the bonding states near the valence band maximum. A linear expression of type

$$\frac{\delta a}{a} = \frac{D_p}{3K}\,[h^+] = \beta_p\,[h^+] \tag{2.12}$$

can be used to describe this contribution, where D_p is the hydrostatic deformation potential at the top of the valence band [66] and K is the bulk elastic modulus of diamond ($K = 4.42 \times 10^7 N cm^{-2}$ [59]). Taking all these terms into account, one gets

$$\frac{\delta a}{a} = \beta_{size}\,[B] + \beta_{pair}\,[BB] + \frac{D_p}{3K}\,[h^+] \tag{2.13}$$

By coincidence, the data points obtained from the ab initio calculations for isolated boron atoms lie on the same linear interpolation (with β_{vol}) obtained for the specific volume approach of boron clusters. Assuming that the lower linear interpolation in Fig. 2.10 mimics results of calculations for systems free of boron pairs and where $[B] = h^+$, one can estimate $\beta_p = \beta_{vol} - \beta_{size} = -2.74 \times 10^{-25} cm^3$. This yields $D_p = -2.26\ eV$, in good agreement with former band struture calculations where $D_p = -2.4\ eV$ [67].

In the case of (111)-oriented growth (Fig. 2.9(b)), the experimental expansion values are always significantly lower than predicted by Vegard, even at relatively low boron content. The values are somewhat close to what is expected for boron pairing, probably indicating that such boron pairing is favoured for growth in direction {111}. This was already suggested previously [44, 15]. Furthermore, the presence of electrically inactive boron pairs is likely to explain the somewhat higher boron concentration threshold necessary to obtain metallicity and superconductivity in our (111)-oriented epilayers compared to (100)-oriented single crystal diamond films [68].

Sample	CH_4/H_2 [%]	B/C [ppm]	N_B [$10^{20}cm^{-3}$]	d [μm]	$\Delta(\Theta)$ [°]
$DMO\,\{100\}$					
411	4	1200	2.4	250	-
662	4	500	4.0	2500	-
666	4	705	4.8	2500	0.0364
400	4	800	6.3	2700	0.0523 (0.0125*)
418	4	1730	9.0	3000	0.0913 (0.0212*)
420	4	2200	11.5	2000	0.1158 (0.030*)
412	4	1600	12.0	3000	0.0237*
419	4	1845	13.0	3750	0.0268*
438	4	2000	16.0	900	0.0290*
507	4	1800	19.0	100	-
509	4	1800	26.0	75	0.1893

Table 2.3.: Overview of the formerly grown samples DMO along direction {100}. Beside information about the gas mixture used for growth, the boron concentration and the thickness determined from secondary ion mass spectroscopy (SIMS) is indicated, as well as results of the symmetrical HRXRD analysis (Results with * are obtained under experimental conditions using the $Mo\ K\alpha_1$ with a wavelength of $\lambda = 0.07093$ nm).

$CN\,\{111\}$	CH_4/H_2 [%]	B/C [ppm]	N_B [$10^{20}cm^{-3}$]	d [μm]	$\Delta(\Theta)$ [°]
109	0	3000	3.0	0.6	n.d.
110	5	10000	30.0	0.5	0.04835
112	8	6000	14.0	0.8	0.0148
113	10	4500	6.0	0.8	0.00687

Table 2.4.: Overview of the formerly grown samples CN along direction {111}. Beside information about the gas mixture used for growth, the boron concentration and the thickness determined from secondary ion mass spectroscopy (SIMS) is indicated, as well as results of the symmetrical HRXRD analysis.

Sample	CH_4/H_2 [%]	B/C [ppm]	N_B [$10^{20}cm^{-3}$]	d [μm]	$\Delta(\Theta)$ [°]
$PA\{100\}$					
06	4	100	2.05	2.0	0.0129
21	4	300	1.9	0.9	n.d.
27	4	350	2.5	≥ 20.0	0.01914
33	4	400	3.3	0.9	0.0256
36	4	430	4.9	≥ 20.0	0.03776
26	4	450	3.6 - 4.2	0.84	0.03107
08	4	600	6.4	2.0	0.0568
34	4	1000	12.6	≥ 20.0	0.0989
09	4	1200	11.4	3.8	0.0883
10	4	1500	13.0	4.2	0.1229
16	4	1500	18.0	≥ 20.0	0.1213
22	4	1500	13.2	0.75	0.14033
30	4	1500	14.0	1.5	0.13001
14	4	1800	12.9	3.7	0.1137
15	4	2000	14.8	3.5	0.13255
19	4	2500	40	1.2	0.2066
23	4	2500	45	2.0	0.24292

Table 2.5.: Overview of the more recently grown samples PA along direction {100}. Beside information about the gas mixture used for growth, the boron concentration and the thickness determined from secondary ion mass spectroscopy (SIMS) is indicated, as well as results of the symmetrical HRXRD analysis.

$PA\{111\}$	CH_4/H_2 [%]	B/C [ppm]	N_B [$10^{20}cm^{-3}$]	d [μm]	$\Delta(\Theta)$ [°]
01	0,15	6000	17.7	0.34	0.0256
28	0,15	6000	17.0	0.02	n.d.
07	0,3	1500	17.9	0.42	0.0226
02	0,3	6000	35.6	0.37	0.0603
11	0,45	6000	50.7	0.23	0.0854
20	0,6	500	4.5	0.35	n.d.
25	0,6	740	2.25	0.45	n.d.
31	0,6	1000	9.5	0.45	n.d.
03	0,6	6000	65.0	0.3	0.10895
17	0,6	6000	70.6	0.23	0.09265

Table 2.6.: Overview of the more recently grown samples PA along direction {111}. Beside information about the gas mixture used for growth, the boron concentration and the thickness determined from secondary ion mass spectroscopy (SIMS) is indicated, as well as results of the symmetrical HRXRD analysis.

2.3. Metal-insulator transition and superconductivity (C:B)

As already mentioned, in diamond the critical boron concentration of the metal-insulator transition coincides with the one necessary to obtain superconducting behaviour. This is illustrated by Fig. 2.11(a) which shows the temperature dependence of the resistivity for several (100)-oriented boron-doped single crystal diamond samples. Formerly and recently grown samples have been compared, and the boron concentration as determined from secondary ion mass spectroscopy (SIMS) is indicated. The low temperature transport changes from a clear insulating behaviour with a diverging resistivity when approaching T$\rightarrow$ 0 K to a metallic (and even superconducting) behaviour with a finite zero-temperature conductivity ($\sigma_0 \neq 0$) by increasing the boron concentration n_B from $n_B = 4.0 \times 10^{20}\ cm^{-3}$ to about $n_B = 4.8 \times 10^{20}\ cm^{-3}$. Within the 10 % uncertainty of SIMS one finds a critical boron concentration of approximately $n_c \approx 4.5 \times 10^{20}\ cm^{-3}$, which is in very good agreement with zero-temperature model calculations of the vanishing ionization energy or of the chemical potential for both the insulating and the metallic phase [37], yielding $n_c \approx 5.2 \times 10^{20}\ cm^{-3}$.

In Fig. 2.11(b), the resistivities obtained experimentally (at $T = 10K$) are compared with resistivity values calculated from a recently proposed generalized Drude approach, for both formerly and recently grown samples [69, 70]. The critical concentration for the doping-induced metal-insulator transition is estimated from these results and calculated using the dielectric function model with a Lorentz-Lorenz correction [71, 72, 69]. Within this approach, the static resistivity can be written as

$$\rho(0) = \frac{16\hbar k_F^3}{12\pi n_B E_F} \int_0^\infty Q^2 \frac{\partial\alpha(Q,W)/\partial W|_{W=0}}{\left[\epsilon + \alpha_1(Q,0)\right]^2} dQ \tag{2.14}$$

where $W = \hbar\omega/4E_F$, $Q = q/2k_F$, and α_1 and α_2 are related to the total dielectric function through

$$\epsilon_T(q,\omega) = \epsilon + \alpha_1(q,\omega) + i\alpha_2(q,\omega) \tag{2.15}$$

Hereby, ϵ is the dielectric constant, E_F is the Fermi energy, and k_F is the Fermi wave number. Furthermore, only a single valence band with an effective mass $m^* = 0.74$ and $\epsilon = 5.7$ has been considered, and it has been assumed that scattering arises from randomly distributed Coulomb impurities. This approach leads also to a critical boron concentration n_c on the order of $(4-5) \times 10^{20}\ cm^{-3}$, in good agreement with our ex-

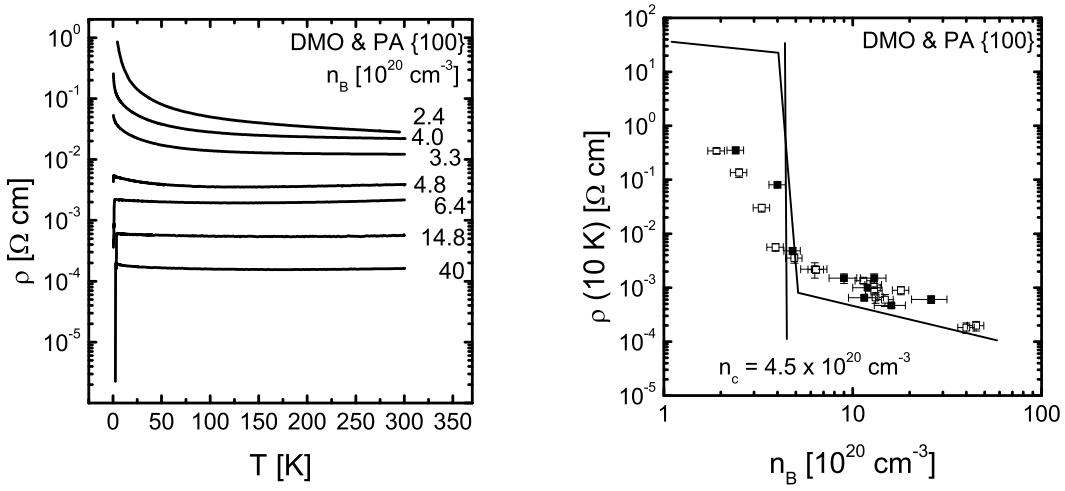

(a) (b)

Figure 2.11.: (a) Temperature dependence of the resistivity of several formerly grown (DMO) and more recently grown (PA) samples. The transition from insulating samples to metallic and superconducting samples is shown; (b) Resistivity (at T= 10 K) as a funtion of boron concentration deduced from SIMS for both sets of samples (DMO and PA). The solid line corresponds to calculations in the general Drude model. A metal-insulator transition is predicted for $n_B \approx 4.5 \times 10^{20}\ cm^{-3}$, in good agreement with experimental data.

perimentally obtained value. On the metallic side of the transition, the experimental values are slightly higher than the theoretically calculated values, as quantum interference effects which are likely to increase the resistivity have to be taken into account. On the insulating side of the transition, the experimental values are lower than the theoretically obtained values due to the fact that the theoretical approach does not take into account the presence of any hopping channel for electronic transport.

Previous analysis of the metal-insulator transition in ion-implanted boron-doped films had suggested a critical boron concentration n_c of about $4 \times 10^{21}\ cm^{-3}$ [73], about one order of magnitude higher than our experimentally and theoretically obtained values. This was probably due to the reduced doping efficiency coming from non-substitutional incorporation of boron in the diamond lattice, leading to the formation of interstitial boron and boron vacancy pairs [74]. The formation of B_2 dimers (on substitutional sites) yields deep gap states. Therefore these B_2 dimers are electrically inactive, thus not providing free carriers to the system [44]. Furthermore, the implantation process unavoidably results in the creation of defects in the mate-

rial and, thus, to the trapping of free carriers. By comparing our results obtained on highly boron-doped single crystal CVD diamond to experimental data obtained in 2005 on free-standing highly boron-doped polycrystalline CVD diamond, one finds a good agreement with values $1.76 \times 10^{20}\ cm^{-3} < n_c < 4.25 \times 10^{20}\ cm^{-3}$ [75] and $3.4 \times 10^{20}\ cm^{-3} < n_c < 5.5 \times 10^{20}\ cm^{-3}$ [7].

Below the critical boron concentration, the resistivity is rapidly increasing with decreasing temperature, and cannot be explained by a simply Boltzmann-like activated behaviour. A so-called hopping transport mechanism has to be taken into account, which requires the existence of localized states around the Fermi level. Hopping of carriers from one occupied localized state to another unoccupied localized state may yield a finite current density, and the probability that a carrier hops from an occupied to an unoccupied site, separated by a distance R, depends on the overlap of the wave functions of the two sites and on their energy difference ΔE. This probability Γ is given by

$$\Gamma \propto \exp\left(-2\alpha R\right) \exp\left(-\frac{\Delta E}{k_B T}\right) \tag{2.16}$$

which contains a factor, $\exp\left(-2\alpha R\right)$, describing the tunneling process between the occupied and unoccupied sites, with α the decay parameter of the localized wave function. $\xi = \frac{1}{\alpha}$ is also known as localization length. The interplay between thermal activation and tunneling processes leads to hopping transport [76, 77], characterized by a stretched exponential temperature dependence of the conductivity following

$$\sigma(T) = \sigma_0 \exp\left[-\left(\frac{T_0}{T}\right)^m\right] \tag{2.17}$$

with m depending on the hopping mechanism. In the case where $\frac{\Delta E}{k_B T} \ll 2\alpha R$, Γ is maximum for R minimum, which implies that carriers hop from one to the nearest-neighboring sites. For nearest-neighbour hopping (NNH) m equals unity for simple activated behaviour [78]. In contrast, variable range hopping assumes that the most probable hopping process is not to a nearest neighbour. Mott et al. suggested that the required thermal activation energy ΔE decreases with the hopping distance R_{Hopp} between two sites, while hopping over a large distance reduces the probability for tunneling. Optimizing Eq. 2.16 with respect to the hopping distance R_{Hopp} leads to $m = 1/4$ in Eq. 2.17 in the case of variable range hopping (VRH), as predicted by Mott [79]. Whether one has to deal with two- or three-dimensional hopping conduction depends on the dimensionality of the accessible states contributing to the hopping

transport, and we will focus here only on the three-dimensional case. Hereby, the optimization process of Eq. 2.16 gives us the following expressions for the T_0 value and the optimum hopping lenght R_{Hopp}:

$$T_0 = \left(\frac{512}{9\pi}\right)\left(\frac{1}{k_B N\left(E_F\right)\xi^3}\right), \qquad R_{Hopp} = \left(\frac{9}{8\pi}\right)^{\frac{\xi}{4}}\left(\frac{1}{N\left(E_F\right)k_B T}\right)^{\frac{1}{4}} \tag{2.18}$$

Mott assumed the density of states at the Fermi level, $N\left(E_F\right)$, to be constant [80], but the upper relationship is also valid for more sophisticated approaches taking into account the energy dependence of the density of states (e.g. bandtail approach) [81].

As can be seen in Fig. 2.12, we observe variable range hopping (VRH) taking $m = 1/4$ in Eq. 2.17 in the formerly as well as recently grown samples. The T_0 values range from 10600 K down to 180 K, continuously decreasing when approaching the metal-insulator transition from the insulating side. The slight difference between formerly and recently grown samples with respect to the slightly lower boron concentration in the case of recently grown samples for similar T_0 values can be explained by the higher doping efficiency in the latter due to higher purity during growth. One should also note the slightly higher conductivities obtained.

As shown in Fig. 2.12(a), the VRH law is observed clearly for both the conductivity $\sigma(T)$ and the Hall carrier concentration $n_H(T) = 1/R_H et$ (e the electronic charge, t the thickness of the sample) for the sample with $n_B = 2.4 \times 10^{20}\ cm^{-3}$. The T_0 and $T_{0,H}$ values extrapolated from the temperature dependence of the conductivity and the Hall carrier concentration are 3700 K and 500 K, respectively, yielding a ratio $T_{0,H}/T_0 \approx 0.13$. Variable range hopping occurs via phonon-assisted tunneling between localized states, so that a classical treatment of the Hall effect affecting carriers during hopping is not appropriate. Holstein showed that for multihopping processes it is possible to obtain a dependence of the jumping rate on magnetic field [82]. Based on the work of Holstein, Gruenewald et al. predicted [83], in the case of transport in three dimension, a temperature dependence of the Hall coefficient and the Hall mobility of the form

$$R_H(T) = R_{H,0}e^{(1-\delta)(T_0/T)^{1/4}}, \tag{2.19}$$

$$\mu_H(T) = \mu_{H,0}e^{-\delta(T_0/T)^{1/4}} \tag{2.20}$$

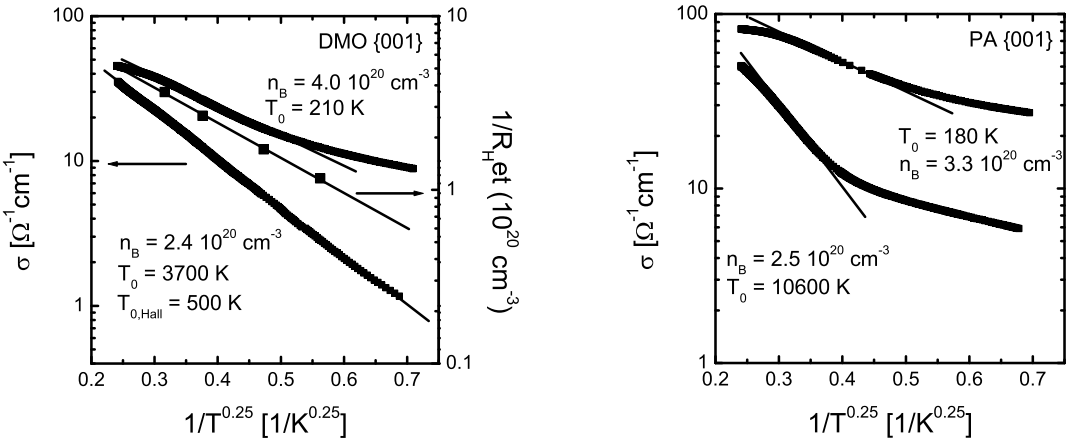

(a) (b)

Figure 2.12.: (a) Semilogarithmic plot of the conductivity and the inverse Hall coefficient as a function of $T^{-0.25}$ (typical for variable range hopping) for two formerly grown samples DMO with $n_B = 2.4 \times 10^{20}\ cm^{-3}$ and $n_B = 4.0 \times 10^{20}\ cm^{-3}$; (b). Similar plot as in (a) for two recently grown samples PA on the insulating side of the transition, with $n_B = 2.5 \times 10^{20}\ cm^{-3}$ and $n_B = 3.3 \times 10^{20}\ cm^{-3}$, respectively.

with $\delta = 3/8$. This prediction was later confirmed experimentally [84]. Thus, variable range hopping predicts that the conductivity $\sigma(T)$ as well as the Hall carrier concentration $n_H(T)$ depend on the temperature according to Eq. 2.17 ($m = 1/4$) and that the ratio $T_{0,H}/T_0 = (1-\delta)^{1/4} = (5/8)^{1/4} = 0.153$ (see Eq. 2.19), which is in good agreement with our experimental result $T_{0,H}/T_0 \approx 0.13$.

As already mentioned, T_0 is related to the localization length ξ and to the density of states at the Fermi level $N(E_F)$ through $T_0 = (C_M/k_B N(E_F)\,\xi^3)^{1/4}$, where C_M is a numerical constant. Percolation theory confirmed the initially by Mott proposed temperature dependence of the conductivity following Eq. 2.17 with $m = 1/4$, but there exists a discrepancy on the value of C_M ranging from 1 to 28 (for instance $(512/9\pi)^{1/4} = 2.08$ for the original Mott picture (see Eq. 2.18)) depending on the model used [85, 86, 87, 88, 89].

As the boron concentration increases, the wave functions of adjacent impurity centers overlap more and more, yielding to the formation of an impurity band. High concentration induces a large impurity bandwidth, corresponding to a large spread in the energy of the localized states of the impurity centers. The impurity bandwidth reflects two contributions: a homogeneous one due to the interaction between the

impurities (even in the case without disorder) and an inhomogeneous one due to the disorder-induced variation of inter-impurity distances and, thus, interaction potentials and associated energies. In the ideal case, the distance between the boron impurity is given by

$$r_{B-B} = (\frac{3}{4\pi n_B})^{1/3} \tag{2.21}$$

where n_B is the boron concentration. The magnitude of the Coulomb interaction between the impurity atoms gives information about the impurity band width w, and can be calculated as

$$w = \frac{e^2}{4\pi\epsilon_0\epsilon_r r_{B-B}} \tag{2.22}$$

where ϵ_r is the dielectric constant [90, 91]. The hopping distance R_{Hopp} and the hopping energy ϵ are related to each other by the three dimensional normalization equation of the one particle DOS $N(\epsilon)$ expression

$$\frac{4\pi}{3} R^3_{Hopp} \int_0^{\epsilon} N(\epsilon) d\epsilon = 1 \tag{2.23}$$

where ϵ is the one-particle energy measured from the Fermi energy E_F. The theory of variable range hopping assumes a constant density of states at the Fermi level, which can be estimated using Eq. 2.21 to Eq. 2.23 to

$$N(E_F) = \frac{n_B}{w} \tag{2.24}$$

Far away from the metal-insulator transition, the impurity centers are spatially well separated, and the localization length ξ can be assumed to be of the order of the Bohr radius a_B and one finds T_0 values on the order of 10^6 K, in good agreement with the value reported by Sato [91] ($(T_0)^{1/4} = 42\ K^{1/4}$). Close to the transition, the localization length ξ is expected to diverge, which would lead to very small T_0 values compared to the value far away from the transition. As can be seen schematically in Fig. 2.13, the driving parameter of the metal-insulator transition describing the distance from the transition point, can be expressed through the boron concentration n_B by $(|n_B/n_c - 1|)$ with n_c the critical boron concentration. The regime close to the transition (in terms of the driving parameter) can be described by two characteristic exponents, ν and η (see Ref. 34 and references therein). Phase A and B in Fig. 2.13 correspond to the insulating and metallic regime, respectively. As indicated, close to

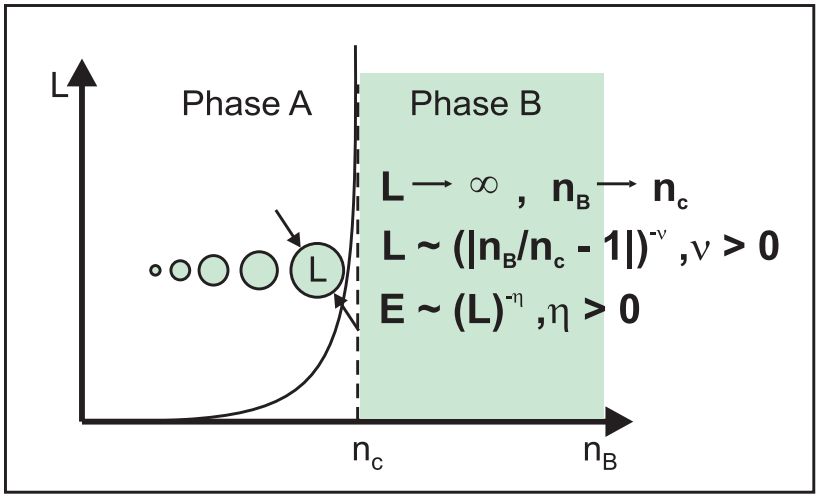

Figure 2.13.: Schematic description of the application of scaling laws to a phase transition between phase A and phase B. The transition is in our case driven by the boron concentration n_B. The typical length scale L of the system, directly connected to the localization length ξ, will diverge when approaching the transition with the first critical exponent ν. The second critical exponent η relates the energy scale to the length scale.

the transition small parts of phase A can coexist in phase B and vice versa. The typical length scale of the system, directly connected to the localization length ξ, will diverge when approaching the transition through

$$L \propto (|n_B/n_c - 1|)^{-\nu} \tag{2.25}$$

with the first critical exponent ν. The larger the coexisting part, the less probable is its occurence, leading us to a second expression relating the energy scale to the length scale via

$$E \propto L^{-\eta} = (|n_B/n_c - 1|)^{\nu\eta} \tag{2.26}$$

Both critical exponents ν and η used in Eq. 2.25 and Eq. 2.26 are positive by definition. Therefore, the 3D density of states at the Fermi level (see Eq. 2.24) is expected to scale as $L^{3-\eta}$, leading to a scaling behaviour of T_0 following

$$T_0 \propto E = L^{-\eta} = (|n_B/n_c - 1|)^{\nu\eta} \tag{2.27}$$

Taking $\nu, \eta > 0$, one finds a vanishing T_0 value by approaching the transition, which is in qualitative agreement with our experimental findings. Furthermore, assuming

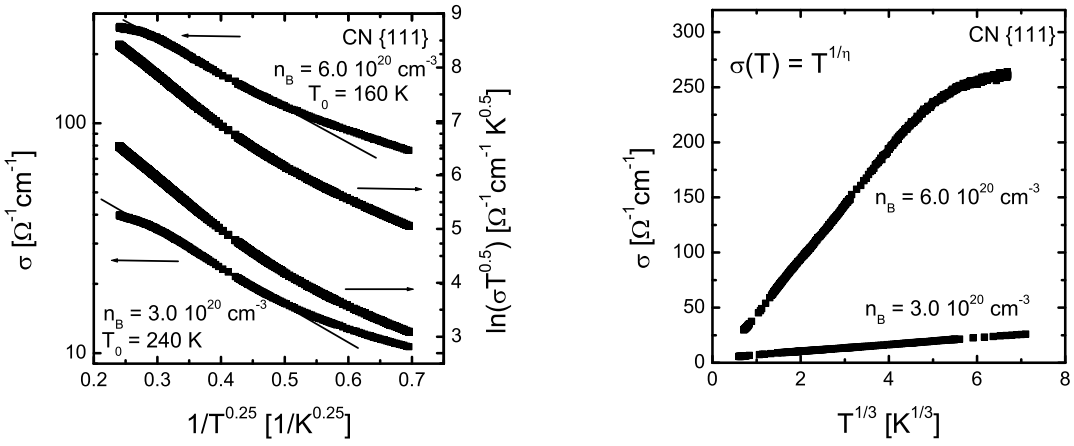

(a) (b)

Figure 2.14.: (a) Semilogarithmic representation of the conductivity for two samples (CN) as a function of $T^{-0.25}$ (VRH). Close to the transition, the T_0 values become smaller and the preexponential factor gains weight. $\sigma_0 \propto 1/T^s$ with $s = 1/2$ can account for the deviation from classical VRH at high temperatures; (b) The conductivity of the same samples than in (a) follow a power law $T^{1/3}$ at low temperature, clearly demonstrating the proximity of the samples to the metal-insulator transition.

$\nu \approx 1$, $\eta \approx 3$, and $n_c \approx 4.5 \times 10^{20}\ cm^{-3}$, the rescaled values of T_0 of all our samples are also in quantitative agreement with the theoretically estimated values, taking $T_0 \approx 10^6\ K$ far away from the transition [70].

Fig. 2.14(a) shows the temperature dependence of the conductivity for two highly boron doped single crystal diamond samples grown along the {111} direction, with boron concentrations $n_B = 3 \times 10^{20}\ cm^{-3}$ and $n_B = 6 \times 10^{20}\ cm^{-3}$, similar to what has been found for (100)-oriented films on the insulating side of the transition. The critical boron concentration for the metal-insulator transition is therefore slightly higher for (111)-oriented films than for (100)-oriented films, probably due to the more favourable formation of B_2 dimers, as already discussed in Chap. 2.2). Compared to its value far away from the transition, T_0 becomes very small close to the transition (240 K and 160 K in Fig. 2.14(a)). Thus, the variation of the exponential term $exp(-(T_0/T)^m)$ becomes small close to the metal-insulator transition and the temperature dependence of the prefactor σ_0 in Eq. 2.17 should be taken into account ($\sigma_0 \propto 1/T^s$). As can be seen Fig. 2.14(a), the small deviations from the variable range hopping regime (also seen in Fig. 2.12) at high temperatures can be well reproduced taking $s = 1/2$ as predicted in the Mott regime [77].

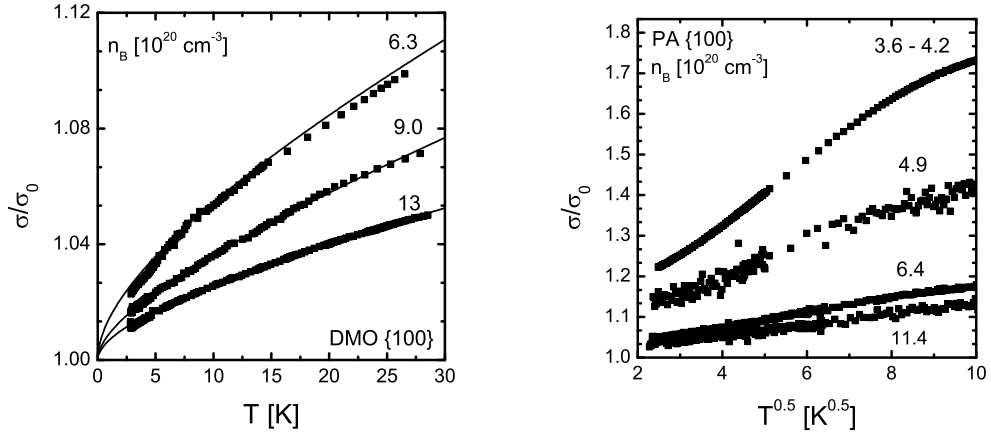

(a) (b)

Figure 2.15.: (a) Temperature dependence of the conductivity for formerly grown samples (DMO) on the metallic side of the transition. The solid lines are fits to the data following Eq. 2.29 typical for a disordered metal; (b) Equivalent square root representation of the temperature dependence of the conductivity for recently grown samples (PA) on the metallic side, indicating the dominance of the localization term at low temperatures.

As will be discussed in detail in Chap. 3.2, at low temperatures, the temperature dependence of the conductivity should show a crossover from the variable range hopping regime (with $m = 1/4$ in Eq. 2.17) to the so-called Efros-Shklovskii hopping regime (with $m = 1/2$ in Eq. 2.17) [92, 93, 94]. Electron-electron interactions lead to the formation of a so-called soft Coulomb gap Δ_{CG}, which reduces the number of states available for hopping [77]. In the case of boron-doped diamond, such a crossover has been reported by Tshepe et al. [73], and a progressive change from $m = 1/4$ at high temperatures to $m = 1/2$ and finally $m = 1$ (presence of a hard gap, see Ref. 77) at low temperatures has been reported by Sato et. al [91] for $n_B \approx 1.76 \times 10^{19}\ cm^{-3}$. Nevertheless, in our case, the deviations from the variable range hopping regime seen in Fig. 2.12 and Fig. 2.14(a) cannot be explained by a crossover to Efros-Shklovskii hopping regime due to a weaker temperature dependence. It is important to note that the Coulomb gap Δ_{CG} is also expected to vanish when approaching the transition (similar to Eq. 3.2). This leads to a vanishingly small region in which Efros-Shklovskii hopping could be observed. Finally, not much is known about the temperature dependence of the prefactor for this type of hopping.

In the critical regime of the transition [34], the conductivity σ is expected to scale

as

$$\sigma(T) \propto \frac{1}{L} \propto E^{1/\eta} \propto T^{1/\eta} \tag{2.28}$$

Tshepe at al. [73] reported that such a temperature dependence accounts very well for the deviation from variable range hopping at low temperatures, taking $\eta \approx 3$. Fig. 2.14(b) shows the power law dependence in temperature $T^{1/3}$ of the conductivity of the same samples as shown in Fig. 2.14(a) holding over a large range of temperatures, indicating a close vicinity to the metal-insulator transition. McMillan [34] suggested that $1 < \eta < 3$ depending on the relative importance of one-electron localization and many-body correlation and screening effects. Scaling analysis applied to disordered metals revealed $\eta \approx 2$ [95, 96], whereas in doped silicon $\eta \geq 3$ [88, 89], in good agreement with numerical calculations [97].

Fig. 2.15 shows the temperature dependence of the conductivity σ for metallic highly boron-doped single crystal diamond samples (Fig. 2.15(a) for formerly grown samples (DMO) with a linear scale in temperature, and Fig. 2.15(b) for recently grown (PA) samples in the more common $\sqrt{T}$ representation). Electron-electron interactions and localization effects typical for disordered metals (see Ref. 98 and references herein), are leading to

$$\sigma_T = \sigma_0 + A \times T^{1/2} + B \times T^{p/2} \tag{2.29}$$

where p is an index depending on the scattering mechanism. Thouless [99] argued that inelastic scattering introduces random fluctuations in the time evolution of an electronic state, which limit quantum interference necessary for localization. The inelastic scattering time $\tau_{in} \propto T^{-p}$ and, thus, the electron diffuses a distance $L_{Th} = (D\tau_{in})^{1/2} = aT^{-p/2}$ with $D = (v_F^2\tau/d)$ the diffusion constant. At lowest temperatures, the localization term dominates the interaction term with the $\sqrt{T}$ dependence because the index p is greater than one, depending on the inelastic scattering mechanism (The estimates for p are 3/2 and 2 for Coulomb interactions in the dirty and clean limit, respectively, and 3 in the case of electron-phonon scattering [98]). In the case of $Ge:Sb$, $p = 2$ (pure limit with electron-electron inelastic processes) gives a fairly good fit [100]. Considering $p = 2$, this is in good agreement with our experimental data (see Fig. 2.15), taking reasonable A ($\approx 1 - 10\ \Omega cm/K^{1/2}$) and B ($\approx 1 - 10\ \Omega cm/K$) values. The $\sqrt{T}$ dependence of the interaction term has already been found in doped semiconductors [101, 102], for $Si:P$ the coefficient A was found to change sign as a function of disorder which was succesfully explained using a Thomas-Fermi screening

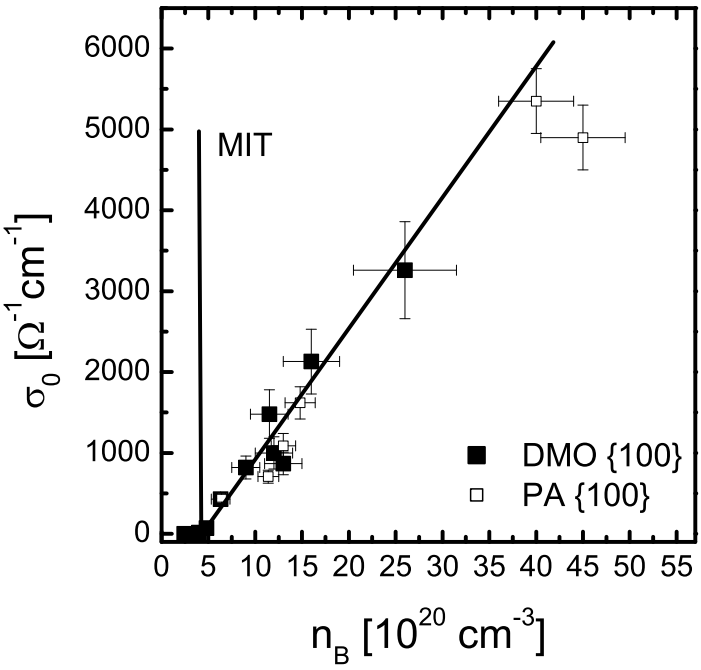

Figure 2.16.: Conductivity extrapolated to zero temperature as a function of the boron concentration n_B deduced from SIMS measurements in boron-doped diamond films (DMO and PA). The solid line corresponds to the prediction of the scaling theory of the metal-insulator transition with a critical exponent $\nu \approx 1$.

approximation [103].

As already mentioned, on the basis of scaling theoretical approaches, the typical length scale and energy scale are related to the driving parameter via critical exponents ν and η. For the three-dimensional case, the zero-temperature conductivity $\sigma(0)$ (see Eq. 2.29) is expected to scale with the same exponent as the coherence length ξ, following

$$\sigma_0 = \sigma(0) \propto 1/L = 0.1(e^2/\hbar)(1/L) = 0.1(e^2/\hbar)(1/a)(n_B/n_c - 1)^{-\nu} \tag{2.30}$$

where a is the Bohr radius (≈ 3.5 Å). Note that the prefactor $\sigma_M = 0.1(e^2/\hbar a)$ equals the minimum metallic conductivity introduced by Mott (see Eq. 1.7).

As can be seen in Fig. 2.16, the extrapolated zero-temperature conductivity $\sigma(0)$ scales almost linearly with the distance from the metal-insulator transition, measured in terms of the boron concentration n_B. The result $\nu \approx 1$ is in good agreement

with the theoretical prediction [104, 34]. This has also been found in many compensated semiconductors (Ge:Sb [105], Si:P,B [106], Ge:Ga,As [107]) and amorphous alloys [34, 95, 108, 109], as well as uncompensated Ge:Sb [110]. In contrast to this, $\nu \approx 0.5$ has been obtained with nominally uncompensated semiconductors (Si:P [111], Si:As [112, 113, 114], Ge:As [115], Si:B [116]) and turns out to be incompatible with theoretical predictions [98, 117]. More recently, higher order calculations of the scaling theory (exclusively with disorder and no interactions) predict $\nu \approx 1.3$ [118, 119, 120, 121], and is shown to be independent of the strength of spin-orbit interactions [122] (which should play a role in the case of Si:B where $\nu \approx 0.5$ was found [116]). It is therefore clear that the effect of disorder alone cannot explain the experimental results of $\nu \approx 0.5$ or 1. Chayes et al. combined the theories of Mott and Anderson and successfully set the lowest limit $\nu > 2/3$ [123]. In response to these discrepancies, several theoretical ideas supporting $\nu \approx 0.5$ have been proposed [88, 124, 125], but a complete understanding is still lacking. More recently, $\nu \approx 1.3$ was found in uncompensated Si:P [126]. Stupp et al. questioned the large critical region of concentration used for the extrapolation. The restriction to values of concentration for which A in Eq. 2.29 is positive leads to a scaling with a critical exponent $\nu \approx 1.3$ in agreement with theoretical predictions. Shlimak et al. [127] also found $\nu \approx 1$ for uncompensated Ge:As. Nevertheless, the exponents $\nu \approx 1 - 1.3$ claimed for melt-doped Si:P [126] and Ge:As [127] should be interpreted with great caution. Due to the spatial fluctuations of the dopant concentration (also segregation is a typical phenomenon), the definition of a critical region is difficult. Nevertheless, precise measurements on homogeneously doped, uncompensated Ge:Ga reveal $\nu \approx 0.5$ [128]. More recently, Itoh et al. presented a complete scaling analysis in compensated and uncompensated Ge:Ga [129]. The critical exponent characterizing the zero-temperature conductivity $\sigma(0)$ changes from $\nu \approx 0.5$ to $\nu \approx 1$ for uncompensated and compensated Ge:Ga, respectively, directly revealing the influence of the disorder on the critical exponent. As can be seen in Fig. 2.16, in the case of highly boron-doped single crystal diamond, the linear scaling of the extrapolated zero-temperature conductivity is not restricted to a small range of concentrations close to the critical carrier concentration n_c (as is the case of other studied systems like Si:P,B [116, 126] or Ge:Ga [128, 129]). One has to mention that the control of the boron concentration at these high dopant concentrations is rather difficult, as already indicated by the depth profile of Secondary Ion Mass Spectroscopy (SIMS) (10 % uncertainty). However, the scaling ansatz is not only qualitatively, but also quantitatively in good agreement with our experimental data, thereby using a Bohr radius of $a \approx 3.5$ Å. The robustness of the effect leads

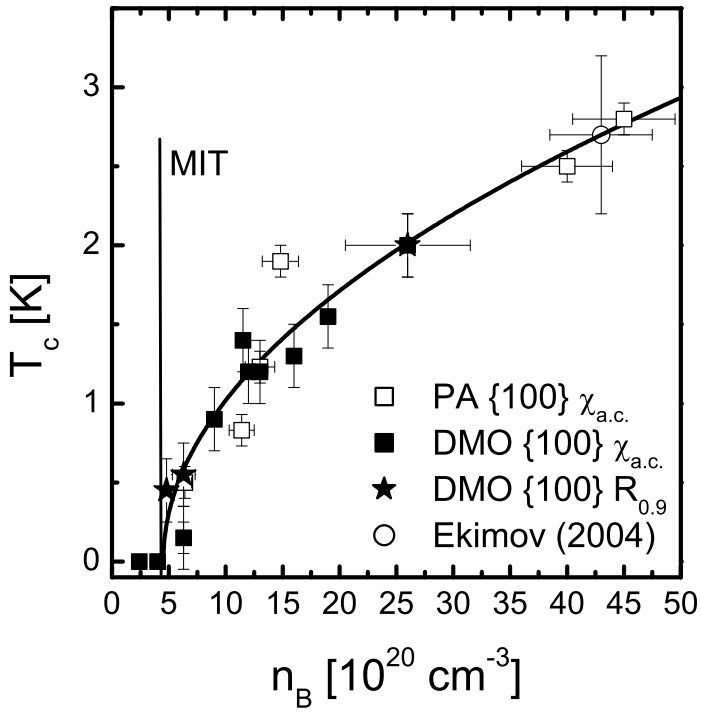

Figure 2.17.: Critical temperature T_c (as deduced from mainly a.c. susceptibility measurements or, if not possible, from resistivity measurements) as a function of the boron concentration n_B as determined from SIMS measurements in boron-doped diamond (DMO and PA). The open circle has been taken from Ekimov et. al [5]. The solid line corresponds to $T_c \approx (n_B/n_c - 1)^{0.5}$.

us to the conclusion that $\nu \approx 1$ is a good approximation, in good agreement with theoretical predictions. Previously, Tshepe et al. [73] obtained $\nu \approx 1.7$ in the case of boron-implanted films, which remains unexplained.

Superconductivity has been observed in all the metallic samples. Fig. 2.17 shows the critical temperature T_c with respect to the distance of the metal-insulator transition, measured again in terms of the boron concentration n_B. No superconducting transition was found in samples with $n_B < 4 \times 10^{20}\ cm^{-3}$ on the insulating side of the transition (see discussion on VRH above). The critical temperatures T_c shown in Fig. 2.17 have been mostly obtained from a.c. susceptibility measurements as the onset of diamagnetic screening. Transport measurements (90 % of the normal state resistance) have been used to determine the critical temperature T_c of sample DMO666 with $n_B = 4.8 \times 10^{20}\ cm^{-3}$, where no onset of diamagnetic screening could be observed down to 20 mK. Transport measurements tend to overestimate the critical temperature

(see comparison for sample DMO400 with $n_B = 6.3 \times 10^{20}\ cm^{-3}$ in Fig. 2.17) due to contributions from filamentary superconducting pathways shortcircuiting the bulk resistance. Very homogeneous samples (DMO509 with $n_B = 2.6 \times 10^{21}\ cm^{-3}$ lead to similar T_c values obtained by either a.c. susceptibility measurements or transport measurements, as well as in this case from tunneling spectroscopy measurements [17]. However, one should note that the critical temperature T_c values are remarkably large down to the metal-insulator transition ($T_c \approx 0.15 - 0.4$ K for $n_B/n_c \approx 1.1$). Such a T_c is actually observed in metals but for a carrier concentration up to a factor 100 to 1000 higher.

As already mentioned, BCS theory [130] predicts that the critical temperature T_c can be written as

$$T_c = 0.85\Theta_D exp\left(-\frac{1}{N(E_F)V_0}\right) \tag{2.31}$$

where Θ_D is the Debye temperature, $N(E_F)$ is the density of states at the Fermi level, and V_0 the effective interaction potential (valid for $N(E_F)V_0 \ll 1$). More realistic approaches take into account the attractive interaction between the electrons (due to electron-phonon coupling λ) on the one side and the Coulomb repulsion (μ) between them on the other side.

McMillan [131] solved the (more realistic) Eliashberg (gap) equation [132] numerically and thereby determined a semi-empirical expression for the critical temperature T_c following

$$T_c = T_{log} exp\left(\frac{-1.04\,(1+\lambda)}{\lambda - \mu^*\,(1+0.62\lambda)}\right) \tag{2.32}$$

with $T_{log} = \hbar\omega_{ln}/1.2$ (see Eq. 1.14), and μ^* is given by

$$\mu^* = \frac{\mu}{1 + \mu \ln\left(E_F/k_B\Theta_D\right)} \tag{2.33}$$

Hereby, E_F is the Fermi energy. As already mentioned, for small λ Eq. 2.32 reduces to the BCS expression in Eq. 2.31 if NV_0 is identified as $\lambda - \mu^*$. In metals, the typical electronic energy scale (identified with the Fermi energy E_F) is much larger than the typical lattice dynamics (identified with the Debye-temperature), so that $E_F/k_B\Theta_D \approx 100$. One finds $\mu^* \approx 1/ln(E_F/k_B\Theta_D) \approx 0.15$. In doped diamond, $E_F/k_B\Theta_D < 3$ and $\mu^* \approx \mu$. The low number of carriers is expected to lead only to poor screening of the Coulomb interactions and, thus, a reduction of μ is not expected, but the proximity to the metal-insulator transition provokes $\mu^* \propto \mu \to 0$ by

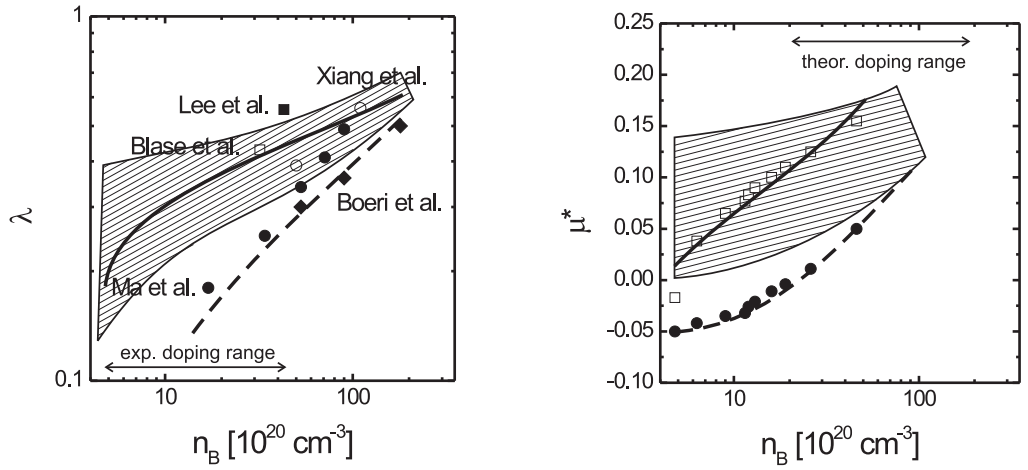

(a) (b)

Figure 2.18.: (a) λ parameter deduced from calculations in the supercell approximation ([23, 24]) and virtual crystal approximation ([20, 22, 21]). The solid and dashed line correspond to $\lambda \propto (n_B/n_c - 1)^{\beta}$ laws with $\beta \approx 0.2$ and 0.5, respectively; (b) The corresponding μ^* values are displayed (open squares and closed circles, respectively), obtained by introducing the experimental T_c values in the McMillan equation. The shaded areas correspond to ensembles $\{\lambda, \mu^*\}$ compatible with our T_c values.

approaching the transition. The parameter μ^* being much less accessible to theoretical calculations than the electron-phonon coupling λ, in most cases a standard value $\mu^* \approx 0.1 - 0.15$ is used [20, 21, 22, 24, 133], leading to T_c values (by using Eq. 2.32 and the calculated value for λ) of the order of a few Kelvin, in good agreement with experimental values. The theoretical values of the coupling constant λ are shown in Fig. 2.18(a), either obtained from ab-initio calculations in a supercell approximation [24, 133] (open symbols) or from virtual crystal approximations [20, 21, 22] (closed symbols). All calculations agree on a value of $\lambda \approx 0.4 - 0.5$ for $n_B \approx \times 10^{22}\ cm^{-3}$ (far away from the metal-insulator transition), the dispersion gets quite large in the experimentally available lower doping region ($n_B \approx \times 10^{20} - 10^{21}\ cm^{-3}$). Theoretical calculations in this doping regime are still missing due to computational limitations.

The influence of the proximity of the metal-insulator transition on the superconducting properties have been studied for a variety of disordered metals [96, 134, 135], revealing the importance of screening of the interaction potential. It has been shown that many disordered superconductors present a dramatic enhancement of their critical temperature when approaching the metal-insulator transition, starting from the pure system and making it more and more disordered (e.g. in the case of W [136], Zr

[137], Al [138], Pd [139], (MoSi, MoGe, WSi, WGe, SiAu) [134], oxide superconductors [135]). Morel and Anderson [140] included the effect of screening by expressing λ and μ^* (see Eq. 2.32 [131, 132]) in terms of the screened Coulomb potential, and compared them to experimental data on elemental metals/superconductors. Using a Coulomb electrostatic potential of the form $V(x) = \frac{e^2}{x} exp(-k_{TF}x)$, the Fourier transform can be written as

$$V(q, k_{TF}) = \frac{4\pi e^2}{k_{TF}^2 + q^2} \tag{2.34}$$

where k_{TF} is the Thomas-Fermi wavevector (related to the Thomas-Fermi screening length l_{TF} by $l_{TF} = 1/k_{TF}$). Integrating Eq. 1.10 and Eq. 1.11, Morel and Anderson found

$$\lambda = N\frac{4\pi e^2}{k_{TF}^2 + q_c^2} = NV_0 \tag{2.35}$$

and

$$\mu = ln(1 + \frac{q_c^2}{k_{TF}^2}) = -ln(\lambda) \tag{2.36}$$

where N is the density of states at the Fermi level, k_F the Fermi wavevector, and q_c a phonon cutoff. Hereby, $q_c = 2k_F$ was suggested by Anderson and Morel and by Pines [141], and $q_c^2 = 0.6q_D^2$ by de Gennes [142], where $q_D^2 = (3/4\pi)^{2/3}4\pi^2/a_0^2$ is related to the lattice constant a_0, leading to the simple result $q_c a_0 \approx 3$. In order to explain the dramatic enhancement of the critical temperature T_c, Soulen et al. [96] replaced the Thomas-Fermi wavevector k_{TF} by an approriate wavevector k_s directly related to the distance $r = (x - x_c)/x_c$ from the metal-insulator transition (driving parameter x with critical parameter x_c) as $k_s^2 \propto k_{TF}^2/(1 + b/r^2)$ (b a constant). Approaching the transition, V increases towards its unscreened value V_0, and accounts for the enhancement of the critical temperature T_c (see Eq. 2.31 and Eq. 2.32). The drop of the critical temperature T_c is explained by the drastic decrease of the density of states. Following scaling theory [131], the density of states N is expected to scale as

$$N \propto E^{-1}L^{-3} \propto L^{\eta-3} \propto (n_B/n_c - 1)^{\nu(3-\eta)} \tag{2.37}$$

where η and ν are the critical exponents for the typical energy and length scale, respectively ($E \propto 1/L^\eta$). For disordered metals, $\eta \approx 2$ and $\nu \approx 1$ were found [95, 96], and the linear drop of N leads to vanishingly small critical temperatures T_c close to the metal-insulator transition. Furthermore, Soulen et al. [96] assumed a Coulomb

potential $\mu^* \approx 0.15$, based on arguments presented above (see Eq. 2.33). As already mentioned, $E_F/k_B\Theta_D < 3$ in doped diamond and, therefore, one finds $\mu^* \approx \mu$ (see Eq. 2.33). The low number of carriers is expected to lead only to poor screening of the Coulomb interactions and, thus, a reduction of μ is not expected, but the proximity to the metal-insulator transition provokes $\mu^* \propto \mu \rightarrow 0$ by approaching the transition.

As already seen in Fig. 2.18(a), all theoretical calculations of the coupling constant λ have been performed for very high dopant concentrations. However, it is tempting to extrapolate these λ values towards the critical concentration n_c, assuming for instance that a scaling law applies to $\lambda \propto (n_B/n_c - 1)^{\beta}$. In contrast to the above mentioned examples of disordered superconductors for which an enhancement of the critical temperature T_c was found by approaching the transition, no such maximum T_c value has been observed so far. This can tentatively be explained by a negligible value of k_{TF} (or k_s) with respect to q_c in Eq. 2.34, and one expects $\lambda \propto N \propto (n_B/n_c - 1)^{\nu(3-\eta)}$ ($\beta = \nu(3-\eta)$). The solid and dashed line in Fig. 2.18(a) represent values for the coupling constant λ following $\lambda \propto (n_B/n_c - 1)^{\beta}$ with $\beta = 0.2$ and $\beta = 0.5$, respectively. In Fig. 2.18(b) the calculated μ^* values obtained from Eq. 2.32 are shown, using both sets of λ values. The λ values with $\beta = 0.5$ reproduce well the calculated λ values using the virtual crystal approximation [20, 21, 22], but as seen in Fig. 2.18(b) such a strong decrease of the coupling constant λ leads to unrealistic negative values for the Coulomb potential μ^*. The shaded regions in Fig. 2.18(a) and Fig. 2.18(b) indicate ensembles of $\{\lambda, \mu^*\}$ values compatible with experimental T_c values, as obtained by inverting Eq. 2.32. For λ values with $\beta = 0.2$ which are compatible with the theoretical results of supercell calculations [24, 133], inverting Eq. 2.32 gives smoothly decreasing μ^* values, in good agreement with scaling analysis fo the metal-insulator transition. The main point is that the coupling constant λ has to remain relatively large down to the transition in order to reproduce the high critical temperatures T_c without introducing unrealistic negative values for the Coulomb potential μ^*. Therefore, the value of β has to be very low (< 0.3), and, since $\beta = \nu(3-\eta)$ and $\nu \approx 1$, one obtains that $\eta \geq 2.7$, in good agreement with transport data in the critical region ($n_B \approx n_c$ and $\sigma(T) \propto T^{1/\eta}$).

2.4. Isotopic substitution in heavily boron-doped single crystal diamond: $^{13}C^{11}B$, $^{13}C^{10}B$

At the very beginning of superconductivity, the question whether the atomic mass of the lattice atoms plays an essential role for the superconductivity or not was already adressed by Onnes in 1922 [143] through the study of two isotopically different sorts of lead (Pb). However, with the insufficient precision in determining the superconducting transition temperature no dependence on atomic mass could be found [144], and one had to wait until 1950. Maxwell [145, 146] and at the same time Reynolds et. al [147, 148] showed that the superconducting transition temperature for mercury (Hg) followed

$$T_c \propto M^{-1/2} \tag{2.38}$$

with M the atomic mass of the by now available, well-controlled isotope variants of Hg. These results on superconducting Hg were very important at this time in substantiating the upcoming ideas of a phonon-mediated interaction [149, 150, 151, 152] playing an essential role later in the BCS theory [130]. Only recently, such a study on isotopically substituted highly boron-doped diamond (grown with HPHT method) was performed, clearly indicating the importance of the host lattice on the superconductivity [19]. This confirms the by most experimentalists and theorists believed phonon-mediated nature of superconductivity in this system. In order to give further insights on the topic, a parallel study of isotopically substituted diamond grown by MPCVD was performed.

2.4.1. Growth and structural properties of $^{13}C^{11}B$ and $^{13}C^{10}B$ diamond

Two series of isotopically substituted diamond films have been grown by MPCVD. The first one only substituted the host lattice carbon atom $^{12}C \rightarrow ^{13}C$ leaving the natural boron abundance of 80 % ^{11}B. In addition, the other series also substituted the boron dopant $^{11}B \rightarrow ^{10}B$. Therefore, three different types of isotopically substituted sets of samples have been grown: the normal $^{12}C^{11}B$ and the substituted $^{13}C^{11}B$ and $^{13}C^{10}B$. Both sets of substituted samples have been grown using standard growth conditions because no experience on this topic existed before in our laboratory. The corresponding gas source was exchanged by equivalent isotopically substituted gas source, with other words ^{13}C-containing methane CH_4 and ^{10}B-containing diborane B_2H_6 have been

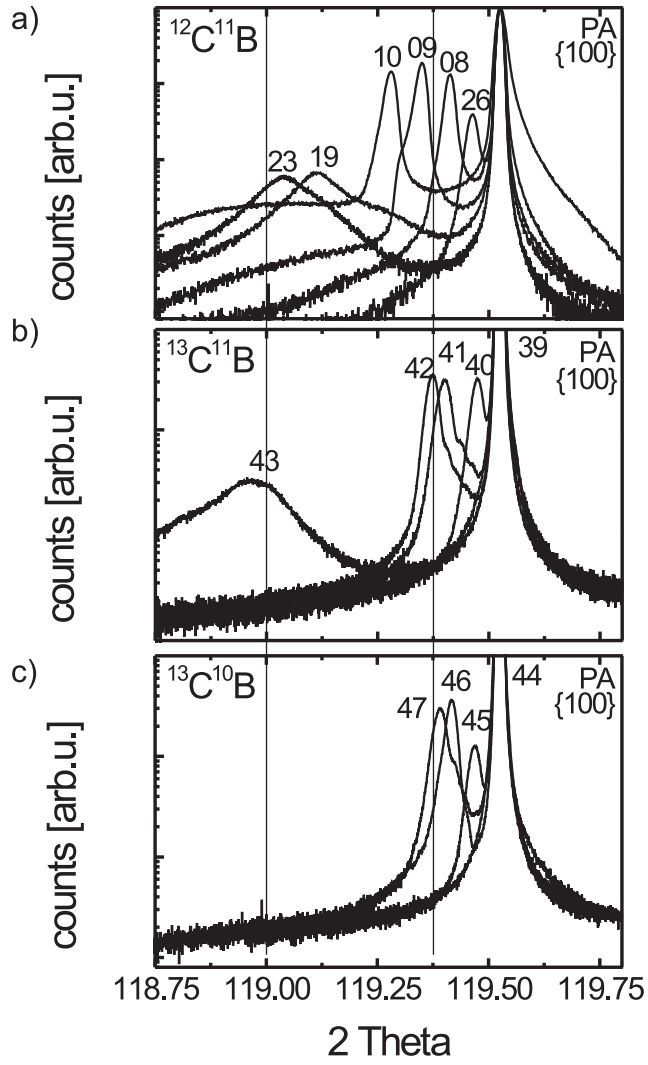

Figure 2.19.: High resolution X-ray diffraction spectra for the three sets of isotopically controlled samples. The good strutural quality is maintained in the two substituted series.

Sample PA	B/C $[ppm]$	d	$N_{^{11}B}$	$N_{^{10}B}$	$N_{B_{tot}}$
$^{13}C^{11}B$		$[\mu m]$	$[10^{20}cm^{-3}]$	$[10^{20}cm^{-3}]$	$[10^{20}cm^{-3}]$
38	0	-	-	-	-
39	300	0.75	1.6	0.4	2.0
40	600	0.84	4.0	0.9	4.9
41	1000	0.8	6.1	1.6	7.7
42	1200	0.9	7.4	1.8	9.2
43	1500	-	-	-	-
$^{13}C^{10}B$					
44	300	0.96	0.25	1.4	1.65
45	600	0.83	0.45	4.6	5.1
46	1000	0.8	0.35	7.4	7.7
47	1200	0.86	0.35	8.9	9.2

Table 2.7.: Overview of the isotopically substituted samples. The boron concentration of both boron isotopes and their sum (total boron concentration), as well as their thickness, as determined from SIMS measurements, is summarized.

used. For all samples grown with the standard source gases $^{12}CH_4$ and $^{11}B_2H_6$ one should note that these gases are not isotopically clean, and the natural abundance of ^{13}C is about 1.1 % and that of ^{10}B even much higher with about 19.9 %. Tab. 2.7 summarizes the results obtained from secondary ion mass spectroscopy (SIMS). As can be seen directly, the natural abundance of ^{10}B is kept maintained in all samples grown with the standard gas source $^{11}B_2H_6$, whereas for the $^{13}C^{10}B$ series the content of ^{11}B is about 5 % of the total boron concentration. The structural properties of both series have further been studied with high resolution X-ray diffraction and Raman spectroscopy.

Fig. 2.19 shows the HRXRD spectra for the three different series $^xC^yB$ along the (004) diffraction peak. The lineshape of both substituted series are comparable to the standard set of samples, indicating the good structural quality of the samples. The comparison of the HRXRD data as well as the results obtained from SIMS, the efficiency of boron incorporation in a wide doping range (up to 1200 ppm) is reduced for growth in a ^{13}C environment with respect to both boron isotopes. This is probably due to a higher impurity of the substituted gas source. Small amounts of oxygen are known to reduce the incorporation efficiency of boron because of preferentially formation of volatile boron oxides on the growing surface. However, the high boron incorporation (as estimated from HRXRD comparison with samples PA19 and PA25, 2500 ppm) in sample PA43 (with 1500 ppm) thus remains unexplained.

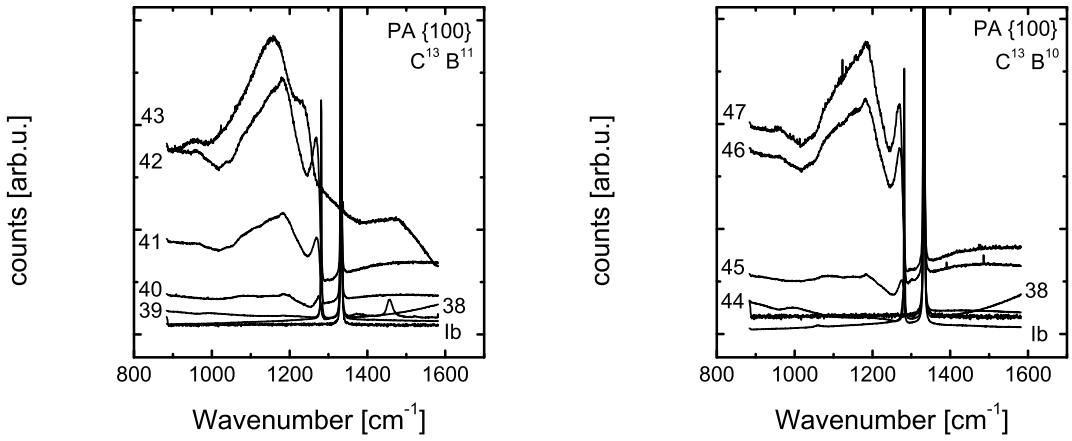

(a) (b)

Figure 2.20.: Visible Raman spectra (633 nm) for both series of isotopically substituted samples: (a) $^{13}C^{11}B$ and (b) $^{13}C^{10}B$. In comparison to a ^{12}C HPHT Ib substrate (natural abundance of 19.9 % ^{10}B), the zone center phonon frequency ω_0 is shifted down to about 1282 cm^{-1} for both ^{13}C substituted series of samples, indicating a high degree of isotopic purity for the carbon host lattice. Also shown is the already discussed Fano resonance occurring at higher doping levels, indicating a large number of free carriers.

Fig. 2.20 shows the Raman spectra (633 nm) obtained on both series of isotopically substituted samples. As already mentioned, the strong covalent bonding and the light mass of the constituent atoms result in a large frequency for the zone center mode. By the control of the isotopic composition of CVD diamond via that of the gas employed, the study of the properties of diamond in which its isotopic composition plays a special role was possible. Several examples are thermal conductivity [153], lattice parameter [154], indirect gap [155], multiphonon infrared spectroscopy [156], and Raman [157, 158, 159] and Brillouin [160, 161] scattering. Chrenko [157] and Hass et. al [158] studied the frequency of the zone center optical phonon (ω_0) in a series of samples which ranged in isotopic composition from $x = 0.011$ to 0.99, with x the atomic fraction of ^{13}C. The decrease in ω_0 is found to follow a $(M_x)^{-1/2}$ dependence as expected from the virtual crystal approximation (VCA), with $M_x = xM_{13}+(1-x)M_{12}$. Therefore, ω_0 is found to be about 1332.5 cm^{-1} for isotopically pure ^{12}C diamond and 1282 cm^{-1} for isotopically pure ^{13}C diamond. One important result shown in Fig. 2.20 is that ω_0 is shifted down to about 1282 cm^{-1} for both ^{13}C substituted series of samples, indicating a high degree of isotopic purity for the carbon host lattice. For several samples, the contribution from the substrate can be seen, situated as a

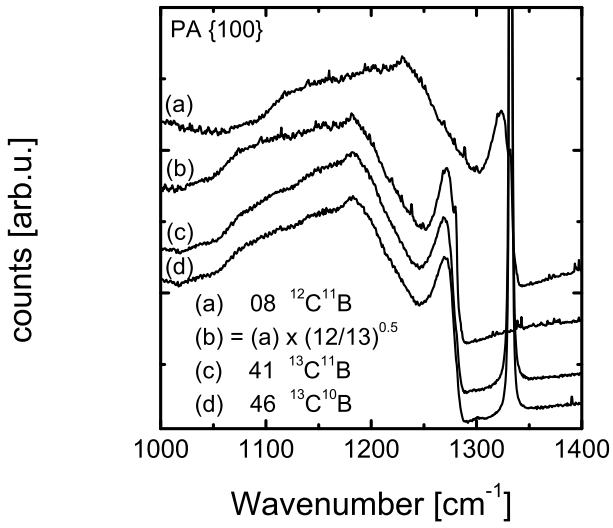

Figure 2.21.: Raman spectra of three comparable samples in boron concentration, but originating from the three different isotopically substituted series of samples. The Raman spectrum of sample PA08 is shifted to lower wavenumber by a factor $\sqrt{12/13}$, taking into account the change of mass of the carbon host lattice. All features correspond to carbon-related phonon modes. No effect of boron substitution can be seen.

response around 1332 cm^{-1}. Also shown in Fig. 2.20 is the Fano resonance occurring at higher doping levels. The Fano effect arises when quantum interference takes place between a discrete energy state (phonon) and a continuum of energy states (electrons), and gives rise to characteristically asymmetric lineshapes [162]. For the isotopically substituted samples, their lineshape is similar to the one obtained for samples grown with the standard source gases, and is a clear feature indicating a high density of free carriers.

In Fig. 2.21, the Raman spectra of three samples with similar boron concentrations in the range from 1000 cm^{-1} to 1400 cm^{-1} are compared. One sample of each isotopically substituted series has been chosen in order to check the influence of the isotopic substitution on the frequencies of the specific phonon modes. For better illustration, the Raman spectrum of sample PA08 is shifted to lower wavenumber by a factor $\sqrt{12/13}$, taking into account the change of mass of the carbon host lattice. It is important to note that all features seen in Fig. 2.21 correspond to carbon-related phonon modes and do not change upon substitution of the boron isotope.

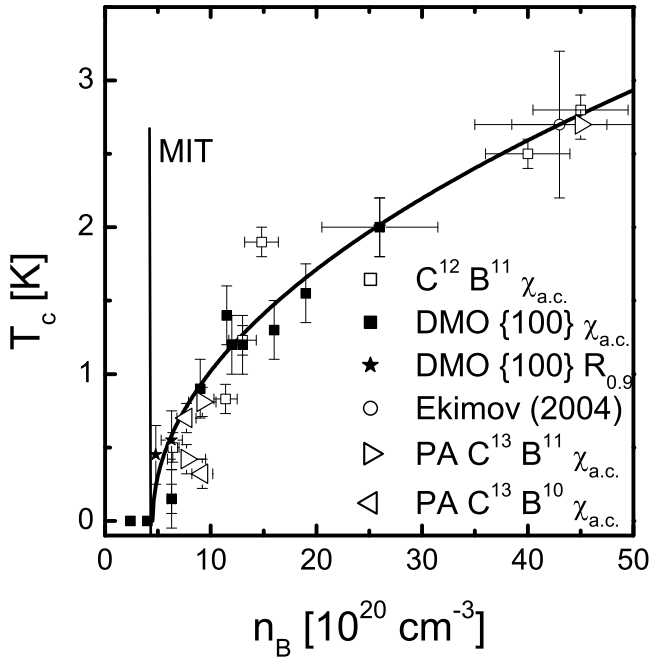

Figure 2.22.: Critical temperature T_c (as deduced from mainly a.c. susceptibility measurements or, if not possible, from resistivity measurements) as a function of the boron concentration n_B as determined from SIMS measurements in boron-doped diamond (DMO and PA) as shwon in Fig. 2.17. In addition, T_c values of both series of isotopically substituted samples are added, but the variation of T_c is not conclusive.

2.4.2. Isotopic substitution and superconductivity

If the above mentioned transition from the normal to the superconducting state in Hg were purely electronic, there should be no dependence upon the nuclear masses. This dependence of the critical temperature for superconductivity upon isotopic mass was the first direct evidence for interaction between the electrons and the lattice, and supported the BCS theory of lattice coupling of electron pairs. It is quite remarkable that an electrical phenomenon like the transition to zero resistivity should involve a purely mechanical property of the lattice.

The isotope effect of the superconducting critical temperature T_c is best described in terms of the isotope coefficient α defined by the relation $T_c \propto M^{-\alpha}$, where M is the atomic mass. Therefore, assuming the dependence of the critical temperature T_c on the atomic mass M is given, one gets

$$\alpha = -\frac{dlnT_c}{dlnM} \tag{2.39}$$

As was already mentioned before, in BCS theory the critical temperature T_c is given by

$$T_c = 0.85\Theta_D exp\left(-\frac{1}{N(E_F)V_0}\right) \tag{2.40}$$

where $\Theta_D \propto \omega_c \propto M^{-1/2}$ is the Debye temperature, directly depending on the lattice vibrations and the atomic mass of the lattice. In the exponential term, the electron-phonon coupling $\lambda = N(E_F)V_0$ enters. It can be shown in a general way that the coupling parameter λ does not depend on the isotopic mass [163]. Therefore, Eq. 2.40 and Eq. 2.39 are leading to classical BCS result $\alpha = 1/2$, in good agreement with the value obtained for many conventional superconductors. The more sophisticated expression for the critical temperature obtained by McMillan [131]

$$T_c = T_{log} exp\left(\frac{-1.04\,(1+\lambda)}{\lambda - \mu^*\,(1+0.62\lambda)}\right) \tag{2.41}$$

where μ^* is given by

$$\mu^* = \frac{\mu}{1+\mu\ln\left(E_F/k_B\Theta_D\right)} \tag{2.42}$$

takes into account the interplay between attractive coupling (λ) and repulsive Coulomb interactions (μ^*). Application of Eq. 2.39 to Eq. 2.41 gives the more complicated expression for the isotope coefficient α

$$\alpha = \frac{1}{2}\left[1 - \frac{1.04\,(1+\lambda)\,(1+0.62\lambda)}{\left[\lambda - \mu^*\,(1+0.62\lambda)\right]^2}\mu^{*2}\right] \tag{2.43}$$

which reduces to the classical BCS result 1/2 for $\mu^* = 0$ and is, in general, less than this when μ^* is finite. So the isotope coefficient will be close to its ideal value when the electron-phonon coulping λ gets much larger than the Coulomb interaction potential μ^*, which is expected for an electron-phonon system with large T_c.

Fig. 2.22 shows the dependence of the critical temperature T_c as determined from a.c. susceptibility measurements on the total boron concentration n_B measured by SIMS. The total boron concentration was obtained as a sum of the two contributions arising from the two boron isotopes ^{11}B and ^{10}B ($n_{B,tot} = n_{^{11}B} + n_{^{10}B}$). As can be seen from Fig. 2.22, only two of the isotopically substituted samples show a signifi-

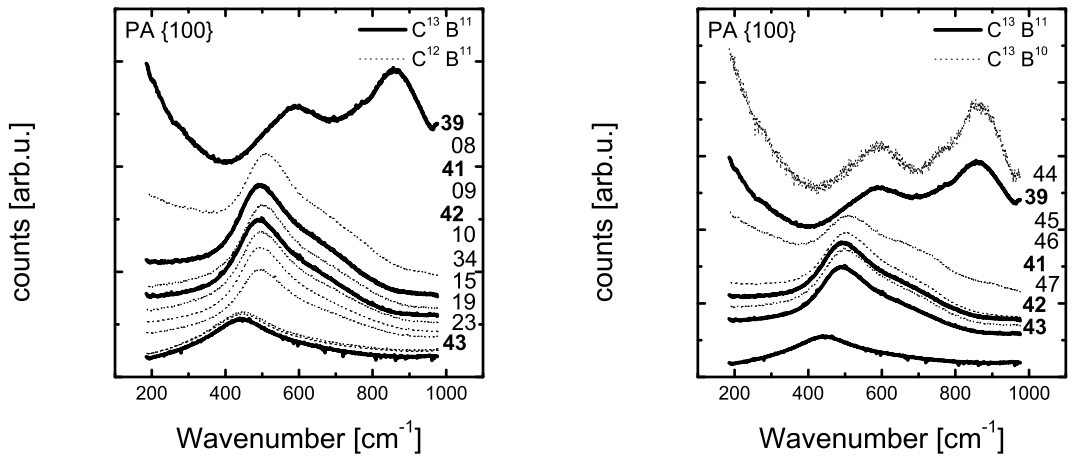

(a) (b)

Figure 2.23.: Visible Raman spectra (633 nm) for both series of isotopically substituted samples in the low wavenumber range. (a) compares the isotopically substituted $^{13}C^{11}B$ series with the reference $^{12}C^{11}B$ series and (b) compares both isotopically substituted series $^{13}C^{11}B$ and $^{13}C^{10}B$.

cant reduction of the critical temperature T_c with respect to the uncertainty in the boron concentration, as expected from the higher atomic mass. These preliminary results show that a phonon-mediated interaction between electrons may account for the superconductivity in highly boron-doped diamond. However, the elaboration of a more adequate series of samples with the corresponding range of boron concentrations should be feasible now and stimulates subsequent work on this interesting topic. The isotopic substitution and its effect on the superconductivity in highly boron-doped diamond remain to play a key role in order to determine wether or not BCS theory accounts for the superconductivity in this system.

2.4.3. Isotopic substitution and existence of boron dimers B_2

Most experiments favor a standard BCS picture involving a phonon-mediated pairing mechanism. Due to the high concentrations of boron atoms in the diamond host lattice, theoretical calculations have addressed the impact of boron clustering on the electronic structure and to the relevance of boron related vibrational modes to the electron-phonon coupling.

Ab initio supercell calculations [44] suggest that a significant fraction of boron atoms may form boron dimers (B_2), which has already been mentioned in the context of SIMS

and HRXRD analysis. This is based on thermodynamical energetical considerations for various neutral and charged defect structures and confirm earlier theoretical work on the formation of boron dimers [166, 167, 168]. Several local vibrational modes have been associated with the existence of such dimers, the most prominent being the Raman active A1g stretching modes at low wavenumbers. As was shown previously, the A1g stretching mode has a parallel-polarized character [164]. The calculations on the B_2-related vibrational modes indicate that upon disorder one should expect a rather broad feature in the $450 - 550\ cm^{-1}$ range of the Raman spectra [164, 165]. Fig. 2.23 shows the Raman spectra of a large set of isotopically well-controlled samples in the low wavenumber range. Comparing Fig. 2.23 and the above presented Raman spectra obtained at higher wavenumbers (see Fig. 2.20), a pronounced but not quite symmetric peak around $500\ cm^{-1}$ and a second weaker feature at $1000\ cm^{-1}$ are present, as well as the already discussed Fano resonance around the softened zone-center optical mode. Neither of the two broad peaks at $500\ cm^{-1}$ and $1000\ cm^{-1}$ is involved in this Fano interference, clearly indicating that these vibrational modes hardly couple to the electronic states. Supercell calculations further confirm that boron dimers are electrically inactive and that dimer-related phonon modes do not couple to the hole states at the top of the valence band [44]. Therefore, in the high doping range the rather smooth evolution of the critical temperature T_c for the superconducting transition probably reflects the presence of electrically inactive B_2 dimers.

All these conclusions are based on theoretical considerations and until now, no direct experimental evidence could be given in order to corroborate the formation of such B_2 dimers. These calculations cannot rule out the presence of other types of defects and the related vibrational modes. For instance, boron situated interstitially in the diamond lattice also contributes to low energy modes ($370 - 450\ cm^{-1}$) [167], but the high formation energy of such a defect do not play in favour in order to account for the very strong Raman peak at about $500\ cm^{-1}$ [168]. Also, vibrational modes in the $500 - 600\ cm^{-1}$ energy range can arise from the presence of $B - C$ stretching modes [24, 44], which contribute significantly to the electron-phonon coupling. However, this is not consistent with the above presented Raman study. From a theoretical point of view, future calculations should be able to display the effect of disorder in order to get more insight into the electronic properties of a random distribution of dimers and isolated boron atoms. From the experimental point of view, isotopic substitution is necessary to confirm the contribution of boron atoms to the vibrational modes.

Fig. 2.23 showed the comparison of Raman spectra obtained on several isotopically substituted samples. In Fig. 2.24 the dependence of the peak position of the low

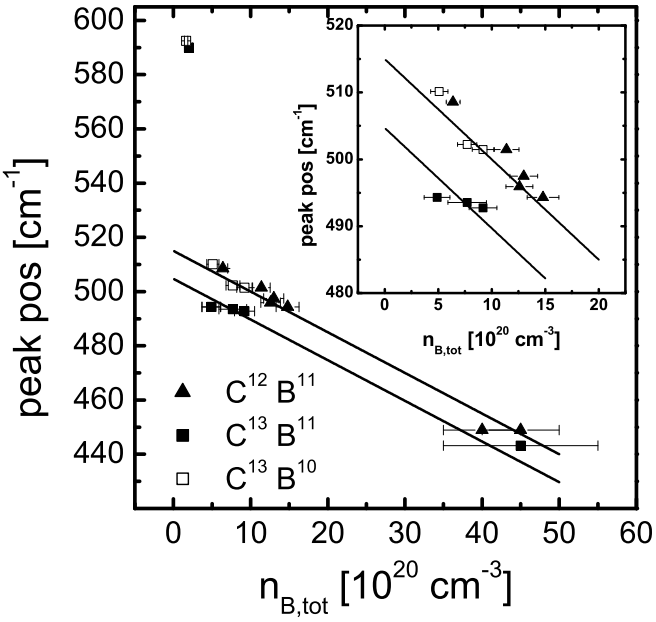

Figure 2.24.: Dependence of the peak position of the low wavenumber feature seen in Fig. 2.23 on the total boron concentration n_B determined from SIMS is shown for the same sets of samples.

wavenumber feature seen in Fig. 2.23 on the total boron concentration n_B determined from SIMS is shown for the same sets of samples. The origin of the low wavenumber peak for electrically insulating must be different for the one of metallic samples. The probed volume is much larger in case of insulating samples, and the low wavenumber peak is likely related to a defect-activated transversal acoustic phonon mode. The inset of Fig. 2.23 zooms out the peak position for metallic samples grown under well-controlled conditions. For the metallic samples, the probed volume is much smaller and the obtained signal strictly related to the epilayer. A rather smooth decrease in wavenumber is obtained on the metallic side of the metal-insulator transition. As pointed out by theoretical calculations, the B_2-related vibrational modes are rather sensitive to the chemical environment in the large doping limit [44]. It is expected that, upon additional hole-doping, the associated modes should be softened. Furthermore, one can see a clear difference in the peak position for the different set of samples with respect to similar boron concentrations in the sample. Both isotopically substituted $^{12}C^{11}B$ and $^{13}C^{10}B$ samples seem to behave in a similar way whereas the peak position of $^{13}C^{11}B$ samples is reduced compared to the other two series.

It becomes clear that from the experimental point of view it is difficult to identify the

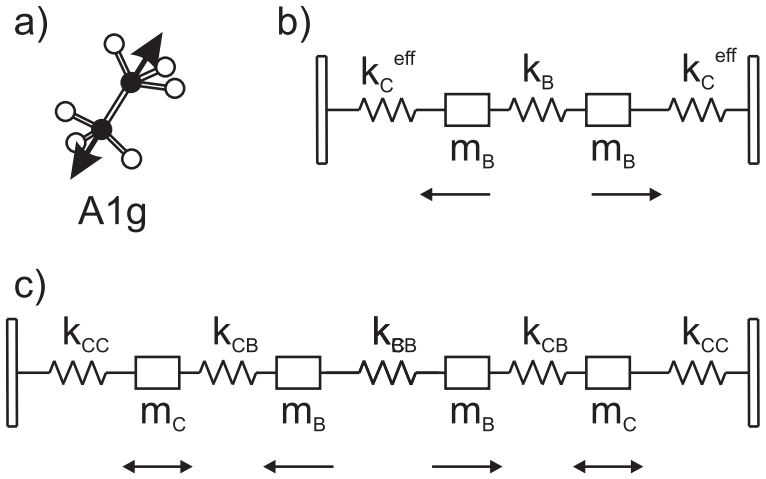

Figure 2.25.: (a) Schematic description of the vibrational mode A1g; (b) Simplified picture equivalent to situation (a), the boron atoms coupled to the rest of the host lattice via the effective coupling constant k_c^{eff}; (c) Similar representation of (a) and (b), taking into account nearest neighbour environment.

origin of the vibrational mode around 500 cm^{-1}. Both types of isotopic substitution ($^{13}C \rightarrow^{12} C$ and $^{11}B \rightarrow^{10} B$) lead to the same shift in frequency. The ratio of the corresponding wavenumbers (straight lines in Fig. 2.23 are guide to the eyes) has a value of 0.98, quite close to both approximations $\sqrt{12/13} \approx 0.961$ and $\sqrt{10/11} \approx 0.953$ using the simplest dependence $\omega = \sqrt{k/m}$ for the frequency (k being the force constant and m the mass). However, based on the combined Raman study and theoretical calculations we will focus on B_2 dimers. Fig. 2.25 (a) shows the associated A1g stretching mode. We will show that the diamond host lattice plays an essential role in the determination of this vibrational mode. Fig. 2.25 (b) shows a rather simplified picture corresponding to this stretching mode. The first neighbours to the boron atoms are kept fixed and interact only via the force constant k_C. This linear approximation is a good representation of the real three-dimensional vibration because the sum of the projections of the three first neighbours onto the $B-B$ direction equals one as a consequence of geometry. The eigenfrequency $\omega_{1,BB}$ of the stretching mode ($x_1 = -x_2$ with x_1 and x_2 the relative position of the left and rigth boron atom) simple model shown in Fig. 2.25 (b) can be calculated and the following relationship holds

$$\omega_{1,BB}^2 = \frac{2k_B + k_C^{eff}}{m_B} \tag{2.44}$$

where k_B and k_C^{eff} are the force constants as shown in Fig. 2.25 (b), and m_B the mass representing the boron atom. One can already see from Eq. 2.44 that the first

neighbours to the B_2 dimer play an essential role via the force constant k_C^{eff}. In order to connect k_C^{eff} to the chemical environment surrounding the first neighbour carbon atoms, one can take a look to the already more complicated model shown in Fig. 2.25 (c). The mass m_C of the first neighbours appear and one distinguishes between three different types of force constants: k_{BB} $(= k_B)$ between two boron atoms, k_{CB} between the boron atom and the first neighbours, and k_{CC} connects these to the rest of the host lattice. The solution to this problem is a bit more complicated, but can be compared to the simpler model of Fig. 2.25 (b) by making two simplifications. The first neighbour carbon atoms follow the boron stretching mode with the same frequency $\omega_{2,BB}$, and in the limit of fixed first neighbours (corresponding to the wall in Fig. 2.25 (b)) $\omega_{2,BB}$ can be written as

$$\omega_{2,BB}^2 = \frac{2k_{BB}}{m_B} + \left(\frac{1}{m_B} + \frac{1}{m_C}\right) k_{CB} \tag{2.45}$$

One should note that with the upper simplifications k_{CC} does not appear in Eq. 2.45, but $\omega_{2,BB}$ can be directly compared to $\omega_{1,BB}$ of Eq. 2.44, leading to

$$k_C^{eff} = k_{CB}\left(1 + \frac{m_B}{m_C}\right) \tag{2.46}$$

k_C^{eff} not only depends on the carbon atomic mass, but also on the boron atomic mass. Using Eq. 2.44, one further gets for the ratios

$$\frac{\omega(12,11)}{\omega(13,10)} = \frac{10}{11}\frac{2k_{11} + k_{12,11}}{2k_{10} + k_{13,10}} \approx 1 \tag{2.47}$$

$$\frac{\omega(12,11)}{\omega(13,11)} = \frac{11}{11}\frac{2k_{11} + k_{12,11}}{2k_{11} + k_{13,11}} \approx \frac{1}{0.98^2} \approx 1.04 \tag{2.48}$$

$$\frac{\omega(13,10)}{\omega(13,11)} = \frac{11}{10}\frac{2k_{10} + k_{13,10}}{2k_{11} + k_{13,11}} \approx \frac{1}{0.98^2} \approx 1.04 \tag{2.49}$$

Introducing the change of k_C with its chemical environment via Eq. 2.46, one obtains two independent equations with three open variables $k_{BB,11}$, $k_{BB,10}$, and k_{CB}. Therefore an adequate choice of these three parameters can fullfill the upper equations, and account for the experimental findings. The above mentioned models are only simplified versions of the real situation. However, the agreement with our experimental data on the different series of isotopically substituted samples leads us to the conclusion that the broad feature seen in Raman around 500 cm^{-1} can be attributed to the vibrational A1g stretching mode related to B_2 dimers.

Further insights could be obtained by taking into account the missing series of isotopically substituted samples with the combination $^{12}C^{10}B$. Unfortunately it was not possible to elaborate such a series during this work, but is highly motivated together with a more detailed study of the isotope effect on the superconducting properties.

2.5. Hall effect in heavily boron-doped single crystal diamond

Based on its exceptional electronic and thermal properties, diamond is an attractive material for electronic devices working at high temperature. Diamond films can now be grown at low temperature and low pressure by chemical vapor deposition (CVD), which allows the achievement of such devices. The active carrier concentration and mobility are important parameters for semiconductor materials when using them for device applications. The key feature of Hall effect measurements is the ability to determine the carrier density, the carrier type, and the mobility. The Hall effect is a phenomenon that occurs in a conductor carrying a current when it is placed in a magnetic field perpendicular to the current [169]. The charge carriers in the conductor become deflected by the magnetic field and give rise to an electric field (Hall voltage) that is perpendicular to both the current and magnetic field (see App. A.4). Hall theory [170, 171] predicts the Hall coefficient R_H as

$$R_H = \frac{r_H \left(p - b^2 n\right)}{q \left(p + bn\right)^2} \tag{2.50}$$

where $b = \mu_n/\mu_p$ the ratio of the mobilities and n and p the density of the electrons and holes, respectively. r_H is the Hall scattering factor. For extrinsic p-type material with $p \gg n$, Eq. 2.50 reduces to

$$R_H = \frac{r_H}{qp} \tag{2.51}$$

and r_H is defined as the ratio of the Hall mobility μ_H to the drift mobility μ. A knowledge of the Hall coefficient leads to a determination of the carrier type as well as the carrier density. The Hall factor r_H depends on the scattering mechanism, temperature, magnetic field, and also on the band structure. The range of values for r_H varies from 1.1 for acoustic deformation potential scattering to 1.9 for ionized impurity scattering in the non-degenerate case [172]. New characteristics like strain and alloying change the valence band structure and an extra scattering process, alloy

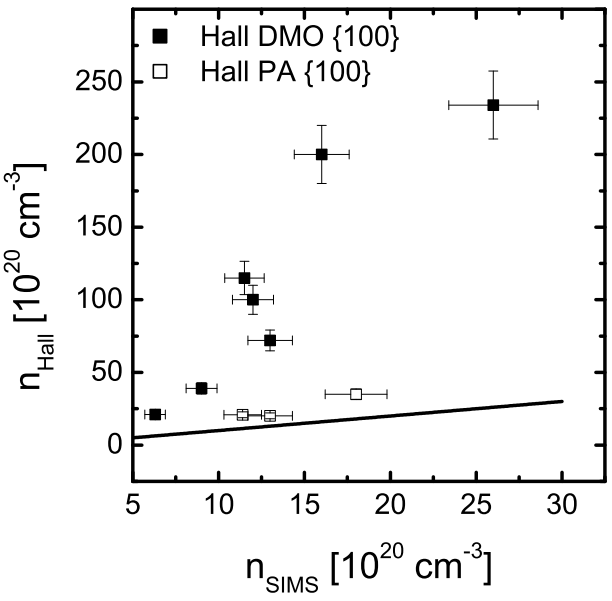

Figure 2.26.: Hall carrier concentration n_{Hall} as a function of the boron concentration $n_B = n_{SIMS}$ as determined from SIMS measurements for several formerly grown DMO and more recently grown PA samples. One clearly sees an up to a factor 12 discrepancy for older samples, giving up a puzzling situation. The solid line corresponds to the situation $n_{Hall} = n_{SIMS}$.

disorder scattering, may be present. Until recently, little was known of the influence of these new characteristics on the Hall mobility and Hall factor. The influence of strain on the Hall factor has been investigated for undoped strained Si, strained $Si_{1-x}Ge_x$, and relaxed $Si_{1-x}Ge_x$ [173, 174, 175].

Fig. 2.26 shows the carrier concentration n_{Hall} measured from Hall effect as a function of the boron concentration n_{SIMS} as determined from secondary ion mass spectroscopy (SIMS) for several formerly and recently grown samples on the metallic side of the transition. For formerly grown samples (DMO) a large discrepancy can be seen between both concentrations, with up to a factor 10 for γ, which gives up a puzzling situation.

In the following, several contributions to the Hall effect are taken into account in order to explain their influence and impact on the Hall effect measurements. As will be seen, Eq. 2.50 and Eq. 2.51 are valid in the case of a uniformly doped layer, but have to be modified in order to take into account the distribution of dopants as seen from the depth profile of SIMS. However, the more sophisticated method cannot account for the observed large discrepancy. Another possibility already mentioned is the influence

of the electronic band structure on the Hall scattering factor r_H. Eq. 2.51 is valid for the special case of a spheroid Fermi surface, and has to be modified to account for the warped electronic valence band structure of diamond. In addition, an outlook will be given on the influence of strain on the electronic band structure of diamond and its influence on the Hall scattering factor r_H. However, the striking difference between results obtained on formerly grown (DMO) and recently grown (PA) samples is not yet understood, a more detailed study of the strain distribution and its influence on the electronic band structure is necessary.

2.5.1. Hall effect in layered structures

The Hall coefficient is determined experimentally as

$$R_H = \frac{dV_H}{BI} \tag{2.52}$$

where d is the sample thickness, V_H the Hall voltage, B the magnetic field, and I the current (see Appendix). The thickness d is well defined for uniformly doped wafers. In contrast, a non-uniform distribution of dopants (as seen from the depth profile in secondary ion mass spectroscopy) can complicate the situation. While standard four-point probe measurements characterize the sheet resistance only, a combination with Hall effect or van der Pauw measurements allow separation of the carrier sheet density and mobility contributions to the sheet resistance. In the case of highly boron-doped (p-type with $p \gg n$ in Eq. 2.50) diamond, one gets an effective carrier concentration $p_{eff} = r_H/qR_H$ with $r_H = \langle\tau^2\rangle / \langle\tau\rangle^2$ (τ being the mean time between carrier collisions, and in general a certain relationship $\tau \propto E^{-\alpha}$). In uniformly doped layers p_{eff} conincides with the carrier concentration, but results from Hall effect measurements on non-uniformly doped layers are more difficult to understand. The resistivity and mobility varies with the film thickness as the carrier or doping density does. A Hall effect measurement gives only information about the average values of carrier density, mobility, and resistivity. Taking into account a spatially varying carrier density $p(t)$ and mobility $\mu_p(t)$, the sheet resistance R_{sh} and the Hall coefficient R_H can be written as [176]

$$R_{sh}(t) = \frac{1}{\sigma_{sh}(t)} = \frac{1}{q\int_0^t p(x)\mu_p(x)dx} \tag{2.53}$$

and

$$R_H(t) = \frac{\int_0^t p(x)\mu_p^2(x)dx}{q(\int_0^t p(x)\mu_p(x)dx)^2} \tag{2.54}$$

assuming $r_H = 1$, which simplifies to Eq. 2.51 for $p(x) = p = const$ (note that $[p] = cm^{-3}$) and $\mu_p(x) = \mu = const$ ($[\mu] = cm^2/Vs$). To determine resistivity and mobility profiles, Hall effect measurements have to be performed as a function of the film thickness. This can be achieved by removing thin portions of the film by etching and subsequent measurement of the Hall coefficient. Profiles have been obtained for GaAs by application of electrolytic etching [177], but a more common method to remove in a reliable way thin portions of the film is by use of anodic oxidation and a subsequent oxide step [178]. In this case of our diamond samples, a controlled removal is not yet optimized and, thus, a study of the depth profile of the resistivity and mobility profiles was not yet feasible.

An estimate of the error introduced by omitting the spatial variation of the doping density and mobility can be obtained by taking a look to the simplest case of a two layer structure. Assuming an upper and lower layer of thickness d_1 and d_2 with conductivities σ_1 and σ_2, respectively, one finds [179, 180]

$$R_H = R_{H1}\frac{d_1}{d}(\frac{\sigma_1}{\sigma})^2 + R_{H2}\frac{d_2}{d}(\frac{\sigma_2}{\sigma})^2 \tag{2.55}$$

with $d = d_1 + d_2$ and $\sigma = \sigma_1 d_1/d + \sigma_2 d_2/d$, and $R_{H1,2}$ the Hall constant of layer 1 and 2, respectively. Imagine the case of a more heavily doped upper layer with $\sigma_1 \gg \sigma_2$, so that

$$\sigma \approx \frac{d_1\sigma_1}{d} \ , \quad R_H = \frac{R_{H1}d}{d_1} \tag{2.56}$$

and the Hall measurement characterizes the upper layer, leading to a misleading underestimation of the conductivity σ_1 and overstimation of the Hall coefficient R_{H1} (factor d_1/d). This has been experimentally observed in HgCdTe [181], but cannot account for the discrepancy shown in Fig. 2.26 for highly boron-doped single crystal diamond (by taking into account the contribution from the substrate).

Equivalent to Eq. 2.55, Eq. 2.54 leads for a two layer structure with carrier concentration P_1 and P_2 (note that $P_i = p_i d_i$ and $[P_i] = cm^{-2}$), respectively, to the following weighted averages for the effective hole density P [182]

$$P = \frac{(P_1\mu_1 + P_2\mu_2)^2}{P_1\mu_1^2 + P_2\mu_2^2} \tag{2.57}$$

and Hall mobility μ_H

$$\mu_H = \frac{P_1\mu_1^2 + P_2\mu_2^2}{P_1\mu_1 + P_2\mu_2} \tag{2.58}$$

As can be seen immediately, for large mobility variations throughout the layer, P will be significantly less than $P_1 + P_2$, and μ_H will lie between μ_1 and μ_2. Therefore, it is possible that the mobility of an inhomogeneous samples is higher than the expected bulk mobility. Recently, this effect has been observed in boron-doped single crystal diamond [183, 184]. However, following Eq. 2.57, the average number of carriers P cannot exceed the dopant concentration as for instance determined by SIMS and, thus, other effects have to be taken into account in order to explain this puzzling situation.

2.5.2. Influence of band structure on the Hall effect

The Hall scattering factor r_H is defined as the ratio of the Hall mobility μ_H to the drift mobility μ and affects the experimentally accessible Hall coefficient R_H via $R_H = r_H/qp$ (for $p \gg n$). An equivalent expression based on the relaxation time τ between scattering events leads to $r_H = \langle\tau^2\rangle / \langle\tau\rangle^2$. The relaxation time is obtained as the reciprocal sum of the total scattering rates, and has a typical dependence on the eigenstate energy ($\tau \propto E^{-\alpha}$, α depending on the scattering mechanism) [185]. In Fig. 2.27, the influence of electric and magnetic fields on electrons in a Brillouin zone approach is shown in order to derive the typical equations for the Hall effect, and to get first insights about the importance of the Fermi surface shape on the Hall effect measurements (see Ref. 186).

In part Fig. 2.27(a), the effect of an electric field alone is shown. The simplest case of a spherical Fermi surface is assumed, and the zone center corresponds to the lowest energy value (typical for a conduction band minimum at Γ). The net result of an applied electric field E (in the positive x-direction) is a shift of the electron distribution by $-eE\tau$, and an increase of the number of electrons in quantum states in the Brillouin zone near region A and in decrease of the number near region B. The velocities (defined as the gradient of the energy distribution) near A have a component to the left, near B to the right. An average momentum P corresponging to the unbalance in the velocity distribution results in a net current to the right (due to the negative charge of the electron) in the direction of the electric field.

Fig. 2.27(b) shows the case where also a perpendicular magnetic field is applied to the situation shown in Fig. 2.27(a). The vector force $-e(\vec{v} \times \vec{B})$ on the electron will result in a changing momentum. Since the force is perpendicular to $\vec{v}$, this results in

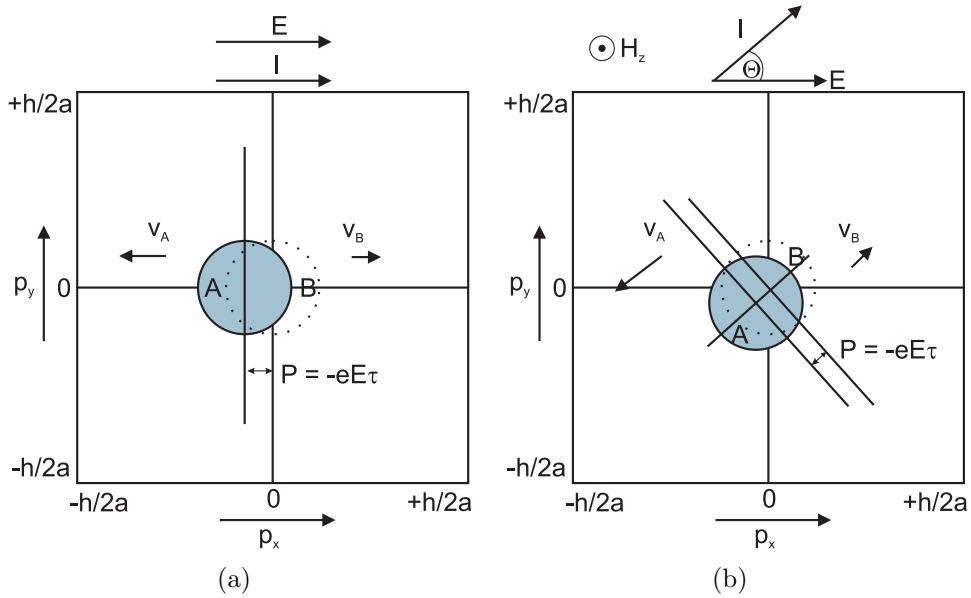

Figure 2.27.: The influence of (a) electric and (b) magnetic fields on electrons in a Brioullin zone approach is shown in order to derive the typical equations for the Hall effect. A spherical Fermi surface is assumed, and the zone center corresponds to the lowest energy value (typical for a conduction band minimum at Γ).

a flow of representative points along the energy contours and the force $\vec{F}$ does not change the energy as it acts perpendicular to the motion $\vec{s}$ ($\vec{F} \cdot \vec{s} = 0$). Note that due to the Pauli principle the flow does not change the density of the points and, thus, remains incompressible. This results in a counterclockwise shift (in the case of holes clockwise) of points in A and the average velocity vector will make an angle Θ with the electric field direction as indicated in Fig. 2.27(b). In terms of relaxation times, it is easy to understand that the angle Θ between the current and the electric field is given by the magnetron frequency times the mean free time. This can be seen from the change in current dI due to the N electrons ($n = N/V$ the density)

$$dI = (ne^2/m)\vec{E}dt - (e/m)\vec{I} \times \vec{B}dt \tag{2.59}$$

and the steady state condition that the sum of all changes is zero, giving

$$(ne^2/m)\vec{E}dt - (e/m)\vec{I} \times \vec{B}dt - \vec{I}dt/\tau = 0 \tag{2.60}$$

where $-\vec{I}dt/\tau$ is the change of current due to collisions. Taking the electric field $\vec{E} = E\vec{e_x}$ in x-direction and the magnetic field $\vec{B} = B\vec{e_z}$ in z-direction one finds the usual equations for the Hall effect

$$I_x = (ne^2\tau/m)E_x = \sigma E_x \tag{2.61}$$

and

$$0 = \sigma E_y - (-I_x B_z)(e\tau/m) \tag{2.62}$$

The Hall coefficient R_H is found to be $R_H = E_y/I_x B_z = -e\tau/m\sigma = \mu/\sigma = -1/en$ (Note that the charge $q = -e$ for electrons was used). Furthermore, for small angles Θ one finds $\Theta = E_y/E_x = e\tau B_z/m = \mu_H B_z$ which defines the Hall mobility $\mu_H = \Theta/B_z$. In general, the Hall mobility won't be equal to the mobility required in the expression for conductivity. The Hall scattering factor $r_H = \mu_H/\mu$ is introduced and depends on the detailed band structure. A more general relaxation time approximation leads to the following expression for the current density j induced by an external electromagnetic field (E,B) [173, 175, 187, 188]

$$j_i = \sum_j \sigma_{ij} E_j + \sum_{jk} \sigma_{ijk} E_j B_k + \cdots \tag{2.63}$$

where i,j,$k = x$,y,z, and one gets

$$\sigma_{xx} = -\frac{e^2}{4\pi^3} \int \tau v_x^2 \frac{\partial f_0}{\partial E} d^3k \tag{2.64}$$

and

$$\sigma_{xyz} = \frac{e^3}{\hbar 4\pi^3} \int \tau^2 v_x \frac{\partial f_0}{\partial E} \left[v_x \frac{\partial v_y}{\partial k_y} - v_y \frac{\partial v_y}{\partial k_x} \right] d^3k \tag{2.65}$$

where

$$\vec{v} = \frac{1}{\hbar} \vec{\nabla}_k E(\vec{k}) \tag{2.66}$$

is the velocity, $E(\vec{k})$ the energy dispersion relation, and f_0 is the distribution function at its equilibrium (for instance Boltzmann or Fermi-Dirac). The drift and Hall mobility μ and μ_H in this approximation are obtained as

$$\mu_{d,xx} = \frac{\sigma_{xx}}{ne}, \quad \mu_{H,xyz} = \frac{\sigma_{xyz}}{ne\mu_{d,xx}} \tag{2.67}$$

with n the carrier concentration. The Hall factor r_H is defined as the ratio $\mu_{H,xyz}/\mu_{d,xx}$, and for a parabolic conduction band with $E = \hbar^2 k^2/2m^*$, one obtains the already

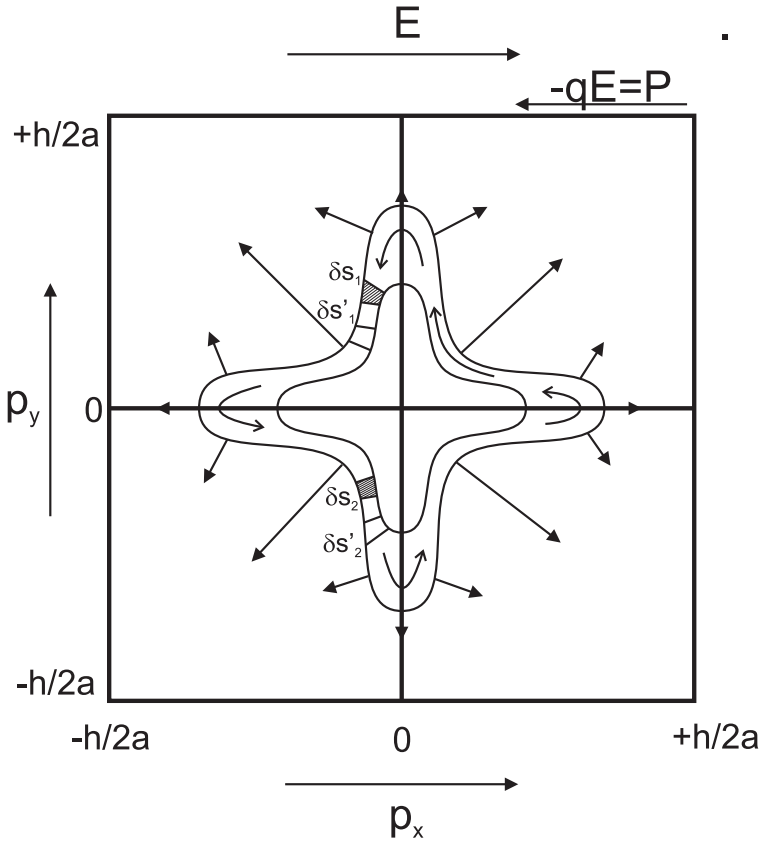

Figure 2.28.: Re-entrant energy surface in the $k_z = 0$ plane in the Brillouin zone. Regions with a large component v_x become important. The y-component of the average velocity plays an important role for the Hall effect.

above mentioned common result

$$r_H = \frac{\mu_{H,xyz}}{\mu_{d,xx}} = \frac{nm^*}{\hbar^2} \frac{\int \frac{d^3k}{4\pi^3} \tau^2 k_x^2 \frac{\partial f_0}{\partial E}}{\left[\int \frac{d^3k}{4\pi^3} \tau k_x^2 \frac{\partial f_0}{\partial E}\right]^2} = \frac{\langle \tau^2 \rangle}{\langle \tau \rangle^2} \tag{2.68}$$

Eq. 2.68 has to be modified in order to account for an arbitrary shape of the Fermi surface, as shown schematically in Fig. 2.28 [186]. This figure represents again the $k_z = 0$ plane in the Brillouin zone for a re-entrant energy surface. In this case, the velocity vector varies in magnitude for a contour of constant energy. From Eq. 2.64 and Eq. 2.65 it becomes clear that regions with a large component v_x become important. As in the above mentioned case of a parabolic energy distribution, a magnetic field implies a flow along the contours of constant energy, in the direction of the arrows shown in Fig. 2.28. Electrons in quantum states in δs_1 and δs_2 will be displaced towards $\delta s_1'$ and $\delta s_2'$, respectively. In contrast to the parabolic case discussed before, these displacements result in a net increase in the $+y$-component of the average velocity.

In other words, the electron rotates in the clockwise direction rather than in the counterclockwise direction as would have been the case for a spheric Fermi surface, and, thus, can give a contribution normally associated to the presence of holes. In summary, a reduction of the value $r_H = \mu_H/\mu$ to values smaller than 1 is probably due to the re-entrant shape of the Fermi surface.

Analogous to the case for electrons, a similar behaviour can occur for holes in the valence band. The Hall scattering factor r_H has been studied in the case of undoped strained Si [175], as well as strained $Si_{1-x}Ge_x$ [173, 174, 175], and relaxed $Si_{1-x}Ge_x$ [175]. In that case, a three-band model has been used, and Eq. 2.64 and Eq. 2.65 need to be evaluated for the energy dispersion describing the light hole band (lh), the heavy hole band (hh), and the spin-orbit band (so). Eq. 2.67 reads then

$$\mu^n_{d,xx} = \frac{\sigma^n_{xx}}{ne}, \quad \mu^n_{H,xyz} = \frac{\sigma^n_{xyz}}{ne\mu^n_{d,xx}} \tag{2.69}$$

for $n = lh$, hh, and so. The Hall scattering factor can thus be written as

$$r_H = \frac{(p_{so} + p_{lh} + p_{hh})(p_{so}\mu^{so}\mu^{so}_H + p_{lh}\mu^{lh}\mu^{lh}_H + p_{hh}\mu^{hh}\mu^{hh}_H)}{(p_{so}\mu^{so} + p_{lh}\mu^{lh} + p_{hh}\mu^{hh})^2} \tag{2.70}$$

where

$$p_n = \frac{1}{4\pi^3}\int f_n(\epsilon_n)d^3k \tag{2.71}$$

with f_n the corresponding distribution function, and ϵ_n the energy dispersion for each band ($n = lh$, hh, and so). The Hall scattering factor r_H was found to depend strongly on strain (and the related change in the electronic band structure), varying from a value of ≈ 3 to ≈ 0.1. Such a strong variation of r_H due to the strong anisotropy of the valence band structure could be a possible key to the understanding of the discrepancy between Hall effect and SIMS measurements in highly boron-doped diamond.

With the discovery of superconductivity, renewed interest came up in the electronic band structure of highly boron-doped diamond. Since then, several studies have appeared, either using VCA [20, 21, 22, 35] or a supercell method [23, 24, 35, 44, 168], and more focused on the electron-phonon coupling said to be responsible for superconductivity. It has been found experimentally as well as theoretically that the electronic band structure of highly boron-doped diamond resembles the one of undoped diamond, with the Fermi level situated below the top of the valence band [16]. The study of the valence band structure of diamond-type semiconductors goes back at least as far back as to the work done by Shockley in 1953 [189]. A detailed study began in the

classic paper by Dresselhaus, Kip, and Kittel [190] in which the A, B, C parameters were introduced in a three-band $k \cdot p$ model, where one finds for the light hole band and heavy hole band

$$E_{lh,hh}(k^2) = Ak^2 \pm \sqrt{B^2k^4 + C^2(k_x^2k_y^2 + k_y^2k_z^2 + k_z^2k_x^2)} \tag{2.72}$$

and for the spin orbit band

$$E_{so}(k^2) = -\Delta + Ak^2 \tag{2.73}$$

where Δ is the spin-orbit split-off (Note that $k^4 = (k_x^2 + k_y^2 + k_z^2)^2$), and an arbitrary wave vector $\vec{k} = (k_x, k_y, k_z)$. Increasing interest in the optical and transport properties of quantum semiconductor structures motivated the use of more complete tight-binding techniques. These works attempt to reproduce the warping of the valence band as shown in Eq. 2.72, and relate the calculated effective masses along the main symmetrical axes to the above mentioned parameters A, B, and C. An equivalent notation uses the Luttinger parameters γ_1, γ_2, and γ_3 [191] (and for completeness κ) which can be expressed as

$$\gamma_1 = -\frac{1}{3}(2F + 4G + 4M) - 1, \tag{2.74}$$

$$\gamma_2 = -\frac{1}{6}(2F + 4G - 2M), \tag{2.75}$$

$$\gamma_3 = -\frac{1}{6}(2F - 2G + 2M), \tag{2.76}$$

$$\kappa = -\frac{1}{3}\gamma_1 + \frac{2}{3}\gamma_2 + \gamma_3 - \frac{2}{3} \tag{2.77}$$

where F, G, and M are related to the Dresselhaus parameters A, B, C via

$$L = F + 2G,\ M = H_1 + H_2,\ N = F - G + H_1 - H_2 \tag{2.78}$$

giving

$$A = \frac{1}{3}(L + 2M) + 1,\ B = \frac{1}{3}(L - M),\ C^2 = \frac{1}{3}(N^2 - (L - M)^2) \tag{2.79}$$

where H_2 is taken to be negligible small. An effective measure of the warping can be defined as the relative change in energy along symmetry axes, for instance [192]

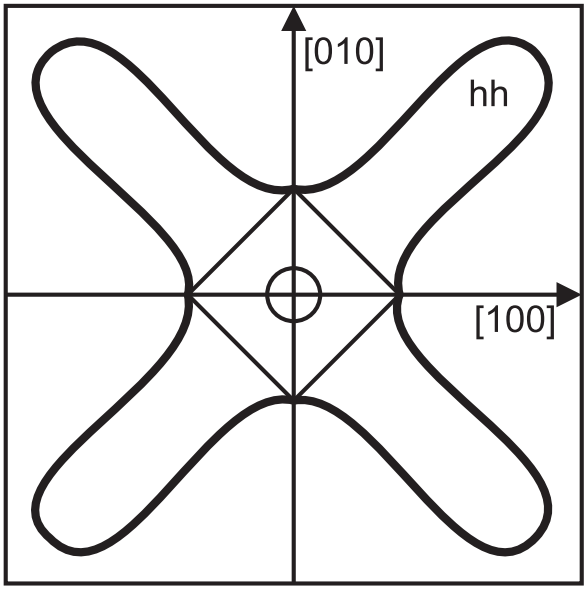

Figure 2.29.: A schematic diagram of the Fermi surface of diamond in the (001) plane of $\vec{k}$-space is shown. One should note the bulging out of this surface for the heavy hole band along the {110} directions. Adapted from Ref. 33.

$$\delta(\Sigma,\Delta) = \lim_{k\to 0} \frac{E(\Delta) - E(\Sigma)}{E(\Delta)} \tag{2.80}$$

where Σ is the {110}-direction ($\Gamma - K$) and Δ is the {100}-direction ($\Gamma - X$) in the Brillouin zone. This can be expressed with the parameters A, B, and C as follows

$$\delta_{lh,hh}(\Sigma,\Delta) = 1 - \frac{A \pm \sqrt{B^2 + \frac{C^2}{4}}}{A \pm |B|} \tag{2.81}$$

Note that in $k \cdot p$ theory, a single parameter C is used to describe the warping, but does not provide a measure of the difference in warping between the light hole and heavy hole band as can be seen from Eq. 2.81 where A and B also enter. It is often said that there is no warping if $C = 0$.

As already mentioned, recent theoretical and experimental work on the electronic band structure of highly boron-doped diamond reveal a standard $\vec{k}$-dependent diamond-like band structure with a Fermi energy situated in the valence band which corresponds to the boron doping [16]. Once the valence band structure is identified, straightforward calculation of the drift and Hall mobility μ and μ_H following Eq. 2.69, as well as the Hall scattering factor r_H (see Eq. 2.70) can be undertaken [173, 174, 175]. A detailed study of the valence band structure via first principles supercell calculations

is underway. Results on undoped (relaxed) diamond neglecting spin-orbit effects gave similar values of effective masses along the main symmetry axes and, thus, a set of Luttinger parameters, as density functional theoretical calculations in the local density approximation, assisted by $k \cdot p$ calculations [191]. A schematic diagram of the Fermi surface of diamond in the (001) plane of $\vec{k}$-space is shown in Fig. 2.29 [33]. One should note the bulging out of this surface for the heavy hole band along the {110} directions. Unfortunately, the {110} direction has not been investigated in the recent angular resolved photoemission study and, thus, needs to be confirmed. From the similarities seen in Fig. 2.29 and Fig. 2.28, one can imagine the possible influence of the warped anisotropic valence band structure on the Hall scattering factor r_H. However, preliminary calculations of the Hall scattering factor r_H using parameter sets (γ_1, γ_2, γ_3) or equivalently (A,B,C) show that the anisotropy alone cannot account for the large discrepancy between Hall effect and SIMS measurements. Based on the idea to take into account the influence of strain on the valence band structure in Si and $Si_{1-x}Ge_x$, this motivates the detailed study of the band structure and of its evolution with strain. It has been shown previously that due to the coherent growth of the highly boron doped epilayer, the lattice parameter in the plane remains unchanged while an expansion of the lattice in the growth direction is observed. Unfortunately, a detailed theoretical investigations of this problem is still lacking. Recently developed $k \cdot p$ methods taking into account the effect of strain on the band structure [193] could be used in order to fit results from supercell calculations, in order to obtain new set of Luttinger parameters under strained conditions. This would be further in agreement with the fact that the discrepancy between Hall effect and SIMS measurements is larger for higher doped samples with therefore higher amount of intrinsic strain. However, the difference between formerly grown sample (DMO) for which the above mentioned picture would apply, and recently grown samples (PA) is still an open question.

Bibliography

[1] F.P. Bundy, J. Geophys. Res. **85**, 6930 (1980).

[2] Ioffe Physico-Technical Institute, http://www.ioffe.rssi.ru/.

[3] E. Rohrer, C.F.O. Graeff, R. Janssen, C.E. Nebel, H. Güttler, R. Zachai, and M. Stutzmann, Phys. Rev. B **54**, 7874 (1996).

[4] S. Koizumi, H. Ozaki, M. Kamo, Y. Sato, and T. Inuzuka. Appl. Phys. Lett. **71**, 1064 (1997).

[5] E.A. Ekimov, V.A. Sidorov, E.D. Bauer, N.N. Mel'nik, N.J. Curro, J.D. Thompson, and S.M. Stishov, Nature **428**, 542 (2004).

[6] Y. Takano, M. Nagao, L. Sakaguchi, M. Tachiki, T. Hatano, K. Kobayashi, H. Umezawa, and H. Kawarada, Appl. Phys. Lett. **85**, 2851 (2004).

[7] K. Winzer, D. Bogdanov, and Ch. Wild, Physcia C **432**, 65 (2005).

[8] E. Bustarret, J. Kacmarcik, C. Marcenat, E. Gheeraert, C. Cytermann, J. Marcus, and T. Klein, Phys. Rev. Lett. **93**, 237005 (2004).

[9] V.A. Sidorov, E.A. Ekimov, S.M. Stishov, E.D. Bauer, and J.D. Thompson, Phys. Rev. B **71**, 060502(R) (2005).

[10] Z.L. Wang, Q. Luo, L.W. Liu, C.Y. Li, H.X. Yang, H.F. Yang, J.J. Li, X.Y. Lu, Z.S. Jin, L. Lu, and C.Z. Gu, Diam. Rel. Mat. **15**, 659 (2006).

[11] M. Nesládek, D. Tromson, C. Mer, P. Bergonzo, P. Hubik, and J.J. Mares, Appl. Phys. Lett. **88**, 232111 (2006).

[12] H. Mukuda, T. Tsuchida, A. Harada, Y. Kitaoka, T. Takenouchi, Y. Takano, M. Nagao, I. Sakaguchi, T. Oguchi, and H. Kawarada, Sci. Technol. Adv. Mater. **7**, S37 (2006).

[13] H. Mukuda, T. Tsuchida, A. Harada, Y. Kitaoka, T. Takenouchi, Y. Takano, M. Nagao, I. Sakaguchi, T. Oguchi, and H. Kawarada, Phys. Rev. B **75**, 033301 (2007).

[14] C.Y. Li, B. Li, X.Y. Lü, M.J. Li, Z.L. Wang, C.Z. Gu and Z.S. Jin, Chin. Phys. Lett. **23**, 2856 (2006).

[15] H. Umezawa, T. Takenouchi, Y. Takano, K. Kobayashi, M. Nagao, I. Sakaguchi, M. Tachiki, T. Hatano, G. Zhong, M. Tachiki, and H. Kawarada, cond-mat/0503303.

[16] T. Yokoya, T. Nakamura, T. Matsushita, T. Muro, Y. Takano, M. Nagao, T. Takenouchi, H. Kawarada, and T. Oguchi, Nature **438**, 647 (2005).

[17] B. Sacépé, C. Chapelier, C. Marcenat, J. Kacmarcik, T. Klein, M. Bernard, and E. Bustarret, Phys. Rev. Lett. **96**, 097006 (2006).

[18] M. Ortolani, S. Lupi, L. Baldassarre, U. Schade, P. Calvani, Y. Takano, M. Nagao, T. Takenouchi, and H. Kawarada, Phys. Rev. Lett. **97**, 097002 (2006).

[19] N. Dubrovinskaia, L. Dubrovinsky, T. Papageorgiou, A. Bosak, M. Krisch, H.F. Braun, and J. Wosnitza, Appl. Phys. Lett. **92**, 132506 (2008).

[20] K.-W. Lee and W.E. Pickett, Phys. Rev. Lett. **93**, 237003 (2004).

[21] L. Boeri, J. Kortus, and O.K. Andersen, Phys. Rev. Lett. **93**, 237002 (2004).

[22] Y. Ma, J.S. Tse, T. Cui, D.D. Klug, L. Zhang, Y. Xie, Y. Niu, and G. Zou, Phys. Rev. B **72**, 014306 (2005).

[23] X. Blase, Ch. Adessi, and D. Connétable, Phys. Rev. Lett. **93**, 237004 (2004).

[24] H.J. Xiang, Z. Li, J. Yang, J.G. Hou, and Q. Zhu, Phys. Rev. B **70**, 212504 (2004).

[25] J. Nagamatsu, N. Nakagawa, T. Muranaka, Y. Zenitani, and J. Akimitsu, Nature **410**, 63 (2001).

[26] J. Kortus, I.I. Mazin, K.D. Belashchenko, V.P. Antropov, and L.L. Boyer, Phys. Rev. Lett. **86**, 4656 (2001).

[27] J.M. An and W.E. Pickett, Phys. Rev. Lett. **86**, 4366 (2001).

[28] A.Y. Liu, I.I. Mazin, and J. Kortus, Phys. Rev. Lett. **87**, 087005 (2001).

[29] H. Kawaji, H. Horie, S. Yamanaka, and M. Ishikawa, Phys. Rev. Lett. **74**, 1427 (1995).

[30] K. Tanigaki, T. Shimizu, K.M. Itoh, J. Teraoka, Y. Moritomo and S. Yamanaka, Nature Mater. **2**, 653 (2003).

[31] D. Connétable, V. Timoshevskii, B. Masenelli, J. Beille, J. Marcus, B.Barbara, A.M. Saitta, G.M. Rignanese, P. Mélinon, S. Yamanaka, and X. Blase, Phys. Rev. Lett. **91**, 247001 (2003).

[32] M. Cardona, Sol. St. Comm. **133**, 3 (2005).

[33] M. Cardona, Sci. Technol.Adv. Mater. **7**, S60 (2006).

[34] W.L. McMillan, Phys. Rev. B **24**, 2739 (1981).

[35] F. Giustino, J.R. Yates, I. Souza, M.L. Cohen, and S.G. Louie, Phys. Rev. Lett. **98**, 047005 (2007).

[36] A. Floris, G. Profeta, N.N. Lathiotakis, M. Lüders, M.A.L. Marques, C. Franchini, E.K.U. Gross, A. Continenza, and S. Massidda, Phys. Rev. Lett. **94**, 037004 (2005).

[37] J. Kacmarcik, C. Marcenat, C. Cytermann, A. Ferreira da Silva, L. Ortéga, F. Gustafsson, J. Marcus, T. Klein, E. Gheeraert, and E. Bustarret, phys. stat. sol (a) **202**, 2160 (2005).

[38] K. Ishizaka, R. Eguchi, S. Tsuda, T. Yokoya, A.Chainani, T. Kiss, T. Shimojima, T. Togashi, S. Watanabe, C.T. Chen, C.Q. Zhang, Y. Takano, M. Nagao, I. Sakaguchi, T. Takenouchi, H. Kawarada and S. Shin, Phys. Rev. Lett. **98**, 047003 (2007).

[39] B. Sacépé, C. Chapelier, C. Marcenat, J. Kacmarcik, T. Klein, F. Omnès and E. Bustarret, phys. stat.sol. (a) **203**, 3315 (2006).

[40] A. Troyanovskiy, T. Nishizaki, and E. Ekimov, Sci. Technol. Adv. Mater. **7**, S27 (2006).

[41] T. Nishizaki, Y. Takano, M. Nagao, T. Takenouchi, H. Kawarada, and N. Kobayashi, Sci. Technol. Adv. Mater. **7**, S22 (2006).

[42] M. Hoesch, T. Fukuda, T. Takenouchi, J.P. Sutter, S. Tsutsui, A.Q.R. Baron, M. Nagao, Y. Takano, H. Kawarada, and J. Mizuki, Sci. Technol. Adv. Mater. **7**, S31 (2006).

[43] M. Hoesch, T. Fukuda, T. Takenouchi, J.P. Sutter, S. Tsutsui, A.Q.R. Baron, M. Nagao, Y. Takano, H. Kawarada, and J. Mizuki, Phys. Rev. B **75**, 140508 (R) (2007).

[44] E. Bourgeois, E. Bustarret, P. Achatz, F. Omnès, and X. Blase, Phys. Rev. B **74**, 094509 (2006).

[45] J.E. Field, *The properties of natural and synthetic diamond* (Academic Press, 1992).

[46] F.P. Bundy, H.T. Hall, H.M. Strong, and R.H. Wentorf, Nature **176**, 51 (1955).

[47] B.V. Deryagin, D.V. Fedoseev, V.M. Lukyanovich, B.V. Spitsyn, A.V. Ryanov, and A.V. Lavrentyev, J. Cryst. Growth **2**, 380 (1968).

[48] J.C. Angus, H.C. Will, and W.S. Stanko, J. Appl. Phys. **39**, 2915 (1968).

[49] D.J. Poferl, N.C. Gadner, and J.C. Angus, J. Appl. Phys. **44**, 1418 (1973).

[50] B.V. Spytsin, L.L. Bouilov, and B.V. Derjaguin, J. Cryst. Growth **52** 219 (1981).

[51] S. Matsumoto, Y. Sato, M. Tsutsumi, and N. Setaka, J. Mater. Sci. **17** 3106 (1982).

[52] M. Kamo, Y. Sato, S. Matsumoto, and N. Setaka, J. Cryst. Growth **62** 642 (1983).

[53] Y. Saito, S. Matsuda, and S. Nogita, J. Mater. Sci. Lett. **5** 565 (1986).

[54] D.G. Goodwin and J.E. Butler, *Handbook of industrial diamonds and diamond films* (Marcel Dekker Ltd., New York, 1997).

[55] E. Gheeraert, *Défauts de structure et impuretés dans les couches minces de diamant élaborées par dépôt chimique en phase vapeur*, thèse à l'Université Joseph Fourier, Grenoble (1992).

[56] P. Gonon, *Films polycristallins de diamant :dopage au bore à partir de la phase vapeur*, thèse à l'Université Joseph Fourier, Grenoble (1993).

[57] J. Hornstra and W. J. Bartels, J. Cryst. Growth **44**, 513 (1978).

[58] F. Brunet, P. Germi, M. Pernet, A. Deneuville, E. Gheeraert, F. Laugier, M. Burdin, and G. Rolland, J. Appl. Phys. **83**, 181 (1998).

[59] Landolt-Börnstein, *Numerical Data and Functional Relationships in Science and Technology Vol. III* (Springer-Verlag, Berlin, 1982).

[60] L. Vegard, Z. Phys. **5**, 17 (1921).

[61] E. Bustarret, E. Gheeraert, and K. Watanabe, phys.stat.sol. (a) **199**, 9 (2003).

[62] V.V. Brazhkin, E.A. Ekimov, A.G. Lyapin, S.V. Popova, A.V. Rakhmanina, S.M. Stishov, V.M. Lebedev, Y. Katayama, and K.Kato, Phys. Rev. B **74**, 140502 (R) (2006).

[63] T. Wojewoda, P. Achatz, L. Ortéga, F. Omnès, C. Marcenat, E. Bourgeois, X.Blase, F. Jomard, and E. Bustarret, Diam. Rel. Mat. **17**, 1302 (2008).

[64] J. Bardeen and W. Shockley, Phys. Rev. **80**, 72 (1950).

[65] I. Yokota, J. Phys. Soc. Jpn. **19**, 1487 (1964).

[66] M. Mermoux, B. Marcus, F. Jomard, C. Tavares, F. Omnès, and E. Bustarret, Diam. Rel. Mat. **15**, 572 (2006).

[67] M. Cardona and N.E. Christensen, Phys. Rev. B **35**, 6182 (1987).

[68] E. Bustarret, P. Achatz, B. Sacépé, C. Chapelier, C. Marcenat, L. Ortéga, and T. Klein, Phil. Trans. R. Soc. A **366**, 267 (2008).

[69] A. Ferreira da Silva, Bo E. Sernelius, J.P. de Souza, H. Boudinov, H. Zheng, and M.P. Sarachik, Phys. Rev. B **60**, 15824 (1999).

[70] T. Klein, P. Achatz, J. Kacmarcik, C. Marcenat, F. Gustafsson, J. Marcus, E. Bustarret, J. Pernot, F. Omnès, Bo E. Sernelius, C. Persson, A. Ferreira da Silva, and C. Cytermann, Phys. Rev. B **75**, 165313 (2007).

[71] Bo E. Sernelius, Phys. Rev. B **41**, 3060 (1990).

[72] E. Abramof, A. Ferreira da Silva, Bo E. Sernelius, J.P. de Souza, and H. Boudinov, Phys. Rev. B **55**, 9584 (1997).

[73] T. Tshepe, C. Kasl, J.F. Prins, and M.J.R. Hoch, Phys. Rev. B **70**, 245107 (2004).

[74] J.P. Goss, P.R. Briddon, S.J. Sque, and R. Jones, Phys. Rev. B **69**, 165215 (2004).

[75] Y. Takano, M. Nagao, T. Takenouchi, H. Umezawa, I. Sakaguchi, M. Tachiki, and H. Kawarada, Diam. Rel. Mat. **14**, 1936 (2005).

[76] H. Fritzsche and M. Pollak, *Hopping and Related Phenomena* (World Scientific, Singapore, 1989).

[77] B.I. Shklovskii and A.L. Efros, *Electronic Properties of Doped Semiconductors* (Springer-Verlag, Berlin, 1988).

[78] A. Miller and E. Abrahams, Phys. Rev. **120**, 745 (1960).

[79] N.F. Mott, J. Non-Cryst. Solids **1**, 1 (1968).

[80] N.F. Mott, *Conduction in non-crystalline materials, 2nd Ed.* (Oxford Science Publications, 1993)

[81] C. Godet, phys. stat. sol. (b) **231**, 499 (2002).

[82] T. Holstein, Phys. Rev. **124**, 1329 (1961).

[83] M. Gruenewald, H. Mueller, P. Thomas, and D. Wuertz, Solid State Commun. **38**, 1011 (1981).

[84] A. Roy, M. Levy, X.M. Guo, M.P. Sarachik, R. Ledesma, and L.L. Isaacs, Phys. Rev. B **39**, 10185 (1989).

[85] V. Ambegaokar, B.I. Halperin, and J.S. Langer, Phys. Rev. B **4**, 2612 (1971).

[86] M. Ortuno and M. Pollak, J. Non-Cryst. Solids **59-60**, 53 (1983).

[87] A.S. Skal and B.I. Shklovskii, Sov. Phys. Solid State **16**, 1190 (1974).

[88] T.G. Castner, Phys. Rev. B **55**, 4003 (1997).

[89] T.G. Castner, *Hopping Transport in Solids* (Elsevier, Amsterdam, 1991).

[90] B. Massarani, J.C. Bourgoin, and R.M. Chrenko, Phys. Rev. B **17**, 1758 (1978).

[91] T. Sato, K. Ohashi, H. Sugai, T. Sumi, K. Haruna, H. Maeta, N. Matsumoto, and H. Otsuka, Phys. Rev. B **61**, 12970 (2000).

[92] A. Aharony, Y. Zhang, and M.P. Sarachik, Phys. Rev. Lett. **68**, 3900 (1992).

[93] Y. Meir, Phys. Rev. Lett. **77**, 5265 (1992).

[94] R. Rosenbaum, N.V Lien, M.R. Graham, and M. Witcomb, J. Phys.: Condens. Matter **9**, 6247 (1997).

[95] G. Hertel, D.J. Bishop, E.G. Spencer, J.M. Rowell, and R.C. Dynes, Phys. Rev. Lett. **50**, 743 (1983).

[96] R.J. Soulen, M.S. Osofsky, and L.D. Cooley, Phys. Rev. B **68**, 094505 (2003).

[97] T. Ohtsuki and T. Kawarabayash, J. Phys. Soc. Jpn. **66**, 314 (1997).

[98] P.A. Lee and T.V. Ramakrishnan, Rev. Mod. Phys. **57**, 287 (1985).

[99] D.J. Thouless, Phys. Rev. Lett. **39**, 1167 (1997).

[100] G.A. Thomas, A. Kawabata, Y. Ootuka, S. Katsumoto, S. Kobayashi, and W. Sasaki, Phys. Rev. B **26**, 2113 (1982).

[101] Y. Ootuka, S. Kobayashi, S. Ikehata, W. Sasaki, and J. Kondo, Solid State Comm. **30**, 169 (1979).

[102] M. Watanabe, Y. Ootuka, K.M. Itoh, and E.E. Haller, Phys. Rev. B **58**, 9851 (1998).

[103] T.F. Rosenbaum, K. Andres, G.A. Thomas, and P.A. Lee, Phys. Rev. Lett. **46**, 568 (1981).

[104] E. Abrahams, P.W. Anderson, D.C. Liccardello, and T.V. Ramakrishnan, Phys. Rev. Lett. **42**, 693 (1979).

[105] G.A. Thomas, Y. Ootuka, S. Katsumoto, S. Kobayashi, and W. Sasaki, Phys. Rev. B **25**, 4288 (1982).

[106] M.J. Hirsch, U. Thomanschefsky, and D.F. Holocomb, Phys. Rev. B **37**, 8257 (1988).

[107] A.G. Zabrodskii and K.N. Zinov'eva, Sov. Phys. JETP **59**, 425 (1984).

[108] M. Rohde and H. Micklitz, Phys. Rev. B **36**, 7572 (1987).

[109] M. Yamaguchi, N. Nishida, T. Furubayashi, K. Morigaki, H. Ishimoto, and K. Ono, Physica (Amsterdam) **118B**, 694 (1983).

[110] Y. Ootuka, H. Matsuoka, and S. Kobayashi, *Anderson Localization* (Springer-Verlag, Berlin, 1988).

[111] T.F. Rosenbaum, K. Andres, G.A. Thomas, and R.N. Bhatt, Phys. Rev. Lett. **45**, 1723 (1980).

[112] P.F. Newman and D.F. Holocomb, Phys. Rev. B **28**, 638 (1983).

[113] P.F. Newman and D.F. Holocomb, Phys. Rev. Lett. **51**, 2144 (1983).

[114] W.N. Shafarman, D.W. Koon, and T.G. Castner, Phys. Rev. B **40**, 1216 (1989).

[115] A.N. Ionov, M.J. Lea, and R. Rentzsch, JETP Lett. **54**, 473 (1991).

[116] P.-H. Dai, Y. Zhang, and M.P. Sarachik, Phys. Rev. Lett. **66**, 1914 (1991).

[117] D. Belitz and T.R. Kirkpatrick, Rev. Mod. Phys. **66**, 261 (1994).

[118] A. MacKinnon and B. Kramer, Phys. Rev. Lett. **47**, 1546 (1981).

[119] T. Ohtsuki, B. Kramer, and Y. Ono, Solid State Commun. **81**, 477 (1992).

[120] M. Henneke, B. Kramer, and T. Ohtsuki, Europhys. Lett. **27**, 389 (1994).

[121] E. Hofstetter and M. Schreiber, Phys. Rev. Lett. **73**, 3137 (1994).

[122] T. Kawarabayashi, T. Ohtsuki, K. Slevin, and Y. Ono, Phys. Rev. Lett. **77**, 3593 (1996).

[123] J. Chayes, L. Chayes, D. S. Fisher, and T. Spencer, Phys. Rev. Lett. **54**, 2375 (1986).

[124] S. Hikami, Phys. Rev. B **24**, 2671 (1981).

[125] J.C. Phillips, Europhys. Lett. 14, 367 (1991).

[126] H. Stupp, M. Hornung, M. Lakner, O. Madel, and H. v. Löhneysen, Phys. Rev. Lett. **71**, 2634 (1993).

[127] I. Shlimak, M. Kaveh, R. Ussyshkin, V. Ginodman, and L. Resnick, Phys. Rev. Lett. **77**, 1103 (1996).

[128] K.M. Itoh, E.E. Haller, J.W. Beeman, W.L. Hansen, J. Emes, L.A. Reichertz, E. Kreysa, T. Shutt, A. Cummings, W. Stockwell, B. Sadoulet, J. Muto, J.W. Farmer, and V.I. Ozhogin, Phys. Rev. Lett. **77**, 4058 (1996).

[129] K.M. Itoh, M. Watanabe, Y. Ootuka, E.E. Haller, and T. Ohtsuki, J. Phys. Soc. Jpn. **73**, 173 (2004).

[130] J. Bardeen, L.N. Cooper, and J.R. Schrieffer, Phys. Rev. **108**, 1175 (1957).

[131] W.L. McMillan, Phys. Rev. **167**, 331 (1968).

[132] G.M. Eliashberg, Sov. Phys. JETP **11**, 696 (1960).

[133] X. Blase, C. Adessi, and D. Connétable, Phys. Rev. Lett. **93**, 237004 (2004).

[134] M.S. Osofsky, R.J. Soulen, Jr., J.H. Claassen, G. Trotter, H. Kim, and J.S. Horwitz, Phys. Rev. Lett. **87**, 197004 (2001).

[135] M.S. Osofsky, R.J. Soulen, Jr., J.H. Claassen, G. Trotter, H. Kim, and J.S. Horwitz, Phys. Rev. B **66** 020502(R) (2002).

[136] W.L. Bond et al., Phys. Rev. Lett. **15**, 260 (1965).

[137] F.P. Missell and J.E. Keem, Phys. Rev. B **29**, 5207 (1984).

[138] R.C. Dynes and J.P. Garno, Phys. Rev. Lett. **46**, 137 (1981).

[139] B. Stritzker, Phys. Rev. Lett. **42**, 1769 (1979).

[140] P. Morel and P.W. Anderson, Phys. Rev. **125**, 1263 (1962).

[141] D. Pines, Phys. Rev. **109**, 280 (1958).

[142] P.G. de Gennes, *Superconductivity in Metals and Alloys* (W.A. Benjamin, New York, 1966).

[143] H.K. Onnes and W. Tuyn, Leiden Commun. **160b** (1922).

[144] E. Justi, Phys. Z **42**, 325 (1941).

[145] E. Maxwell, Phys. Rev **78**, 477 (1950).

[146] E. Maxwell, Phys. Rev **79**, 173 (1950).

[147] C.A. Reynolds, B. Serin, W.H. Wright, and L.B. Nesbitt, Phys. Rev **78**, 487 (1950).

[148] B. Serin, C.A. Reynolds, and L.B. Nesbitt, Phys. Rev **78**, 813 (1950).

[149] H. Fröhlich, Phys. Rev **79**, 845 (1950).

[150] J. Bardeen, Phys. Rev **80**, 567 (1950).

[151] J. Bardeen, Phys. Rev **81**, 829 (1951).

[152] J. Bardeen, Phys. Rev **82**, 978 (1951).

[153] T.R. Anthony, W.F. Banholzer, J.F. Fleischer, L. Wei, P.K. Kuo, R.L. Thomas, and R.W. Pryor, Phys. Rev. B **42**, 1104 (1990).

[154] H. Holloway, K.C. Hass, M.A. Tamor, T.R. Anthony, and W.F. Banholzer, Phys. Rev. B **44**, 7123 (1991).

[155] A.T. Collins, S.C. Lawson, G. Davies, and H. Kanda, Phys. Rev. Lett. **65**, 891 (1990).

[156] T.R. Anthony and W.F. Banholzer, Diam. Relat. Mater. **1**, 717 (1992).

[157] R.M. Chrenko, J. Appl. Phys. **63**, 5873 (1988).

[158] K.C. Hass, M.A. Tamor, T.R. Anthony, and W.F. Banholzer, Phys. Rev. B **45**, 7171 (1992).

[159] J. Spitzer, P. Etchegoin, M. Cardona, T.R. Anthony, and W.F. Banholzer, Solid State Commun. **88**, 509 (1993).

[160] A.K. Ramdas, S. Rodriguez, M. Grimsditch, T.R. Anthony, and W.F. Banholzer, Phys. Rev. Lett. **71**, 189 (1993).

[161] R. Vogelgesang, A.K. Ramdas, S. Rodriguez, M. Grimsditch, and T.R. Anthony, Phys. Rev. B **54**, 3989 (1996).

[162] U. Fano, Phys. Rev. **124**, 1866 (1961).

[163] J.P. Carbotte, Rev. Mod. Phys. **62**, 1027 (1990).

[164] E. Bustarret, A. Gheeraert, and K. Watanabe, phys. stat. solidi a **199**, 9 (2003).

[165] M. Bernard, C. Baron, and A. Deneuville, Diam. Rel. Mater. **13**, 896 (2004).

[166] J.P. Goss, P.R. Briddon, R. Jones, Z. Teukam, D. Ballutaud, F. Jomard, J. Chevallier, M. Bernard, and A. Deneuville, Phys. Rev. B **68**, 235209 (2003).

[167] J.P. Goss, P.R. Briddon, S. Papagiannidis, and R. Jones, Phys. Rev. B **70**, 235208 (2004).

[168] J.P. Goss and P.R. Briddon, Phys. Rev. B **73**, 085204 (2006).

[169] E.H. Hall, Amer. J. Math. **2**, 287 (1879).

[170] R.A. Smith, *Semiconductors, Cambridge University Press, Cambridge, 1959.*

[171] N.W. Ashcroft and N.D. Mermin, *Solid State Physics, Saunders College Publishing, 1976.*

[172] L.M. Roth, *Dynamics and Classical Transport of Carriers in Semiconductors, North-Holland, Amsterdam, 1992.*

[173] Y. Fu, K.B. Joelsson, K.J. Grahn, W.-X Ni, G.V. Hansson, and M. Willander, Phys. Rev. B **54**, 11317 (1996).

[174] K.B. Joelsson, Y. Fu, W.-X Ni, and G.V. Hansson, J. Appl. Phys. **81**, 1264 (1996).

[175] J.E. Dijkstra and W. Th. Wenckebach, J. Appl. Phys. **85**, 1587 (1999).

[176] R. Baron, G.A. Shifrin, O.J. Marsh, and J.W. Mayer, J. Appl. Phys. **40**, 3702 (1969).

[177] T. Ambridge and C.J. Allen, Electron. Lett. **15**, 648 (1979).

[178] N.D. Young and M.J. Hight, Electron. Lett. **21**, 1044 (1985).

[179] R.L. Petritz, Phys. Rev. **110**, 1254 (1958).

[180] R.D. Larrabee and W.R. Thurber, IEEE Trans. Electron Dev. **27**, 32 (1980).

[181] L.F. Lou and W.H. Frye, J. Appl. Phys. **56**, 2253 (1984).

[182] C.M. Wolfe and G.E. Stillman, *Apparent Mobility Enhancement in Inhomogeneous Crystals, Semiconductors and Semimetals, Academic Press, New York, 1975.*

[183] T. Teraji, H. Wada, M. Yamamoto, K. Arima, and T. Ito, Diam. Rel. Mater. **15**, 602 (2006).

[184] J. Pernot, T. Teraji, and F.T. Ito, Hasselt Diamond Workshop SBDD XII, 2007

[185] M. Lundstrom, *Fundamentals of carrier transport, Cambridge University Press, 2000.*

[186] W. Shockley, *Electrons and Holes in Semiconductors, D. van Nostrand, New York, 1950.*

[187] K. Seeger, *Semiconductor Physics, Springer, Berlin, 1991.*

[188] Y. Fu, M. Willander, Z.-F. Li, and W. Lu, Phys. Rev. B **67**, 113313 (2003).

[189] W. Shockley, Phys. Rev. **90**, 491 (1953).

[190] G. Dresselhaus, A.F. Kip, and C. Kittel, Phys. Rev. **95**, 568 (1954).

[191] M. Willatzen, M. Cardona, and N.E. Christensen, Phys. Rev. B **50**, 18504 (1994).

[192] D. Helmholz and L.C. Lee Yan Voon, Phys. Rev. B **65**, 233204 (2002).

[193] Y. Sun, S.E. Thompson, and T. Nishida, J. Appl. Phys. **101**, 104503 (2007).

3. Heavily boron-doped nanocrystalline diamond thin films

As already mentioned, diamond is a potential candidate for various applications due to its outstanding materials properties. The lack of an inexpensive substrate for homoepitaxial growth motivated many efforts made in growth of poly- and nanocrystalline diamond films. Heteroepitaxial growth can be done on a variety of materials used as substrate, for instance silicon but also quartz, opening up the way for large-area application. The material we refer to as nanocrystalline diamond is a small grain size polycrystalline diamond, grown under conventional growth conditions using a hydrogen-rich gas phase. Obviously, after a certain thickness, nanocrystalline diamond become a conventional microcrystalline diamond. The roughness is hereby proportional to the thickness. Therefore smaller grain sizes are generally more desirable.

In the following, a study of the transport properties of heavily boron-doped nanocrystalline diamond thin films at temperatures down to 50 mK will be presented. The films show superconducting properties with critical temperatures T_c up to 2.1 K. The system undergoes a doping-induced metal-insulator transition with an interplay of intergranular conductance g and intragranular conductance g_0, as expected for a granular system with metallic grains. Metallic samples far away from the transition show similarities to heavily boron-doped single crystal diamond. Metallic samples close to the transition show a more rich behaviour. Global phase coherence leads in both cases to superconductivity. A peak in the low-temperature magnetoresistance measurements for samples close to the transition is explained due to corrections to the conductance according to superconducting fluctuations.

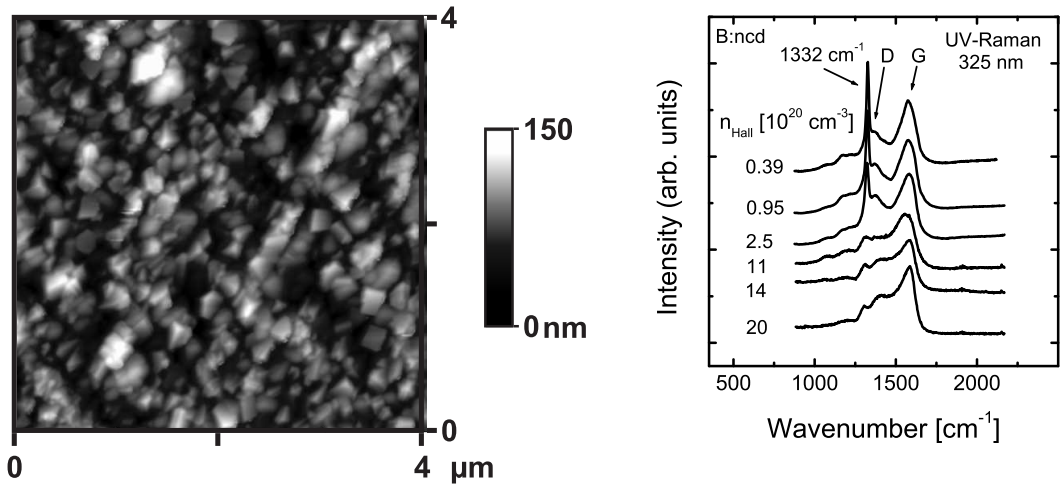

(a) (b)

Figure 3.1.: (a) Typical AFM image of a nanocrystalline diamond sample, with grain sizes of about 200 nm. The grain size does not change upon boron incorporation; (b) UV-Raman spectra (325 nm) of several boron-doped nanocrystalline diamond thin films. One clearly sees the D and G peak originating from sp^2-bonded carbon as well as a peak associated with the central phonon line (at 1332 cm^{-1} for undoped diamond). With increasing doping the central phonon line shifts to lower energies and for high doping concentrations a Fano resonance around the central phonon line can be seen.

3.1. Sample preparation and structural properties of heavily boron-doped nanocrystalline diamond thin films

Nanocrystalline diamond films were grown in a metallic microwave plasma-enhanced chemical vapor deposition (MPCVD) reactor from a hydrogen-rich gas phase, with $CH_4/H_2 \leq 4$ %. Doping with boron was achieved by adding trimethylboron to the gas phase with molar concentrations B/C reaching 10000 ppm (see Tab. 3.1). These films were grown on quartz substrates (suitable for transport measurements). The quartz substrate were either prepared by mechanical polishing (Bmec prefix) or by ultrasonic seeding (Bus prefix) with a monodisperse solution of nanodiamond particles, in order to provide a high density of nucleation sites for film growth [1]. The substrate temperature was maintained at 700 °C, while the total pressure and input power were varied between 30 to 40 Torr and 2500 to 3500 W, respectively.

Fig. 3.1 (a) shows a typical AFM image ($4\mu m \times 4\mu m$) of a boron-doped nanocrys-

talline diamond sample. The typical sample thickness is about 200 nm, with grain sizes about 150 nm. The grain size does not depend on the dopant concentration [2].

The UV-Raman spectra shown in Fig. 3.1 (b) display the presence of the D and G peaks [3], originating from sp^2-bonded carbon in the grain boundaries, as well as a peak associated with the central phonon line (at 1332 cm^{-1} for undoped diamond). With increasing doping a shift of the central phonon line to lower energies and a clear Fano resonance can be seen, as already reported in highly boron-doped single crystalline, polycrystalline, and nanocrystalline diamond [4, 5, 6, 7, 8].

3.2. Metal-insulator transition in heavily boron-doped nanocrystalline diamond

Renewed interest in doping-induced electronic phase transitions came up as superconductivity was discovered in heavily boron-doped polycrystalline diamond prepared in a high pressure high temperature process [9], and was confirmed by several other groups [8, 10, 11, 12, 13, 14] in polycrystalline, single crystalline, and nanocrystalline boron-doped diamond (see Ref. 15 and 16, and references therein). The metal-insulator transition in highly boron-doped diamond has been analyzed in ion-implanted films [17] and more recently by our group in single crystalline diamond [18] (see Chap. 2.3). In this part of the work, we report on the metal-insulator transition in highly boron-doped nanocrystalline diamond (B:ncd) thin films, clearly showing the influence of the granular structure on the transport properties at low temperatures. Tuning the microscopic parameters, a granular material can vary from a relatively good metal to an insulator, depending on the strength of electron tunneling coupling between conducting grains.

Fig. 3.2 shows the room temperature conductivity as a function of the free carrier concentration as determined from room temperature Hall effect measurements for several boron-doped nanocrystalline diamond thin films with boron concentrations (SIMS) in the range from 9.7 $\times 10^{16}$ cm^{-3} up to 3.0 $\times 10^{21}$ cm^{-3} (see Tab. 3.1). A strong increase of almost 10 orders of magnitude from 10^{-8} $(\Omega cm)^{-1}$ up to 75 $(\Omega cm)^{-1}$ already indicates a transition from insulating to metallic samples. Compared to the room temperature conductivity of heavily boron-doped single crystal diamond [4, 18], boron-doped nanocrystalline diamond films have substantially lower conductivities in the high doping range (one order of magnitude). High temperature transport measurements on weakly-doped nanocrystalline diamond films reveal an activation energy

Sample	$[TMB]$	$n_{Hall,300K}$	$[B]$	σ_{300K}	μ_{300K}
	ppm	$[cm^{-3}]$	$[cm^{-3}]$	$[\Omega^{-1}cm^{-1}]$	$[cm^2/Vs]$
Bus0	0	$< 10^{15}$	$9.7 \cdot 10^{16}$	$1.5 \cdot 10^{-8}$	-
Bme50	50	$1.2 \cdot 10^{16}$	-	$3.4 \cdot 10^{-3}$	1.82
Bmec150	150	$7.0 \cdot 10^{15}$	$2.4 \cdot 10^{19}$	$2.4 \cdot 10^{-3}$	2.1
Bus20	20	$7.0 \cdot 10^{18}$	-	0.25	0.22
Bus100	100	$9.5 \cdot 10^{19}$	-	0.30	0.02
Bmec2500	2500	$3.9 \cdot 10^{19}$	$2.3 \cdot 10^{20}$	0.8	0.13
Bus1000	1000	$2.5 \cdot 10^{20}$	$2.9 \cdot 10^{20}$	6.2	0.15
Bmec5000	5000	$5.6 \cdot 10^{20}$	$1.3 \cdot 10^{21}$	21.7	0.27
Bus3000	3000	$1.1 \cdot 10^{21}$	$1.3 \cdot 10^{21}$	29.3	0.16
Bus4000	4000	-	$3.0 \cdot 10^{21}$	34.9	-
Bus4500	4500	$1.1 \cdot 10^{21}$	$1.8 \cdot 10^{21}$	63.3	0.36
Bus10000	10000	$1.4 \cdot 10^{21}$	-	55.2	0.24
Bus6660	6660	$2.0 \cdot 10^{21}$	$2.7 \cdot 10^{21}$	75.8	0.24
Bus5000	5000	$2.4 \cdot 10^{21}$	-	72.2	0.19

Table 3.1.: The 200 nm thick samples are designated after the seeding procedure on the substrate before growth and the boron concentration in the gas phase during growth in ppm. The Hall carrier concentration, the Hall mobility, and the conductivity as determined from Hall and van der Pauw measurements taken at room temperature, as well as the results of SIMS measurements are summarized. Sample Bus0 showed no detectable Hall effect.

of about 390 meV [2], and, thus, indicate substitutional incorporation of boron in these films (see Ref. 19 and references therein). Assuming full ionization at very high doping levels, the difference between the Hall carrier concentration and the larger boron concentration as determined by SIMS (see Tab. 3.1) indicates the compensating effects of the grain boundaries. For heavily boron-doped single crystal diamond, the apparent Hall carrier concentration takes values up to ten times higher than the boron concentration measured by SIMS [18], which is discussed in Chap. 2.5.

The temperature dependence of the normalized resistance $\rho/\rho(300K)$ in the range 300 K down to 350 mK is shown in Fig. 3.3 for several samples. In contrast to the minimum resistivity observed in single crystal diamond at intermediate temperatures [18], the resistivity of nanocrystalline diamond increases with decreasing temperature. The highly doped samples with $n_B \geq 1.3 \times 10^{21} cm^{-3}$ (see Tab. 3.1) also show superconductivity with a critical temperatures of about $T_c = 2.1$ K (Samples Bus1000 and Bme5000 behaved like a disordered metal, but showed no superconductivity down to 350 mK).

Fig. 3.4 (b) shows the effective activation energy E_{act} as determined from the slope

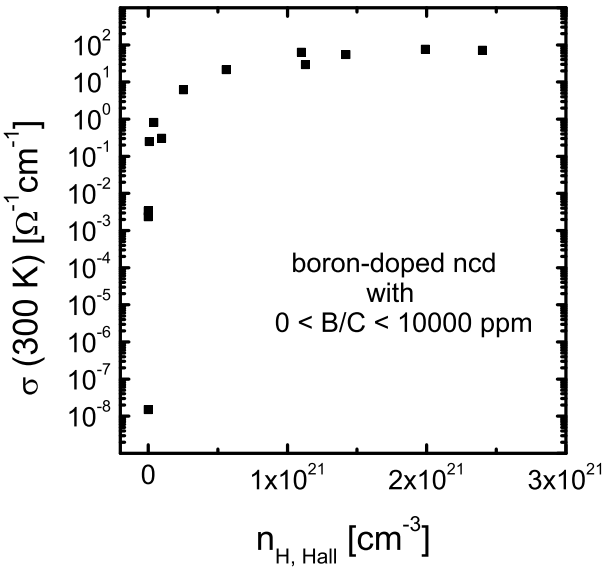

Figure 3.2.: Room temperature conductivity as a function of the free carrier concentration, as determined from room temperature Hall effect measurements, shown for several boron-doped nanocrystalline diamond thin films with boron concentrations (SIMS) in the range from 9.7 10^{16} cm^{-3} up to 3.0 10^{21} cm^{-3} (see Tab. 3.1). The strong increase of the conductivity with boron doping, from 10^{-8} $(\Omega cm)^{-1}$ up to 75 $(\Omega cm)^{-1}$, already indicates the transition from the insulating to the metallic samples.

of Arrhenius plots of the temperature dependent conductivity, normalized to its room temperature value σ^*. Thermally activated transport via hopping conduction ($E_{act} > k_BT$) is only observed for the weakly doped samples Bus100 and Bmec2500. The highly-doped samples behave like a disordered metal. The apparent activation energy of a disordered metal is only a small fraction of k_BT in the corresponding temperature range ($E_{act} < k_BT$), as already reported elsewhere [20, 21, 22]. Therefore, the critical boron concentration n_c for the metal-insulator transition lies in the range from 2.3×10^{20} cm^{-3} up to 2.9×10^{20} cm^{-3}, in good agreement with what was found for single crystal and polycrystalline diamond (see Ref. 15 and 16, and references therein). As will be shown below, the metal-insulator transition is not only due to the increasing doping within the grains, but also to the increase in intergranular coupling between metallic grains.

Fig. 3.5 (a) shows the temperature dependence of the normalized conductivity for the weakly-doped samples Bus100 and Bmec2500, which are close to the metal-insulator transition. An Efros-Shklovskii (ES) type of hopping dependence is observed over

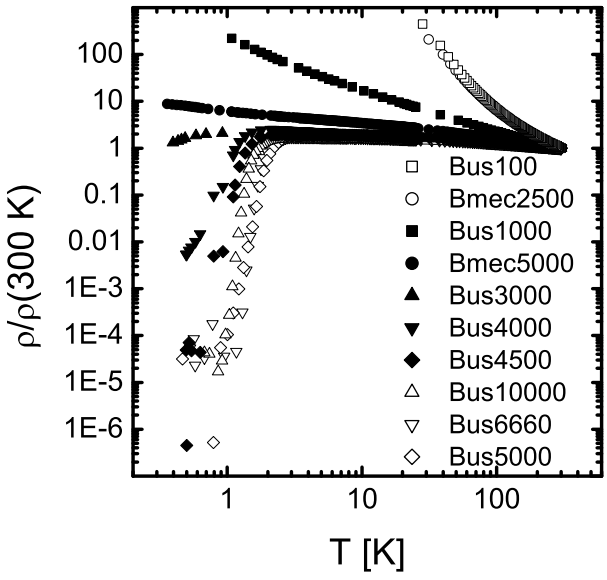

Figure 3.3.: Temperature dependence of the normalized resistance $\rho/\rho(300K)$ from 300 K down to 350 mK. Highly doped samples with $n_B \geq 1.3\ 10^{21} cm^{-3}$ show superconductivity with a critical temperatures of about $T_c = 2.1\ K$.

a strikingly wide range of temperatures, from 300 K down to 20 K. The exponential decrease of conductivity with decreasing temperature is typically seen on the insulating side of disordered materials such as heavily doped semiconductors. The interplay between thermal activation and tunneling processes leads to hopping transport [23, 24], characterized by a stretched exponential temperature dependence of the conductivity following

$$\sigma(T) = \sigma_0 \exp\left[-\left(\frac{T_0}{T}\right)^m\right] \tag{3.1}$$

with m depending on the hopping mechanism. For nearest-neighbour hopping (NNH) m equals unity for simple activated behaviour [25], whereas $m = 1/4$ in the case of variable range hopping (VRH), as predicted by Mott [26]. Taking into account that Coulomb interaction leads to a reduction of the single-particle density of states near the Fermi energy and, thus, to an opening up of the so-called Coulomb gap, the hopping mechanism is called Efros-Shklovskii VRH with $m = 1/2$ instead of $m = 1/4$ [27, 28, 29]. The Coulomb interaction plays an important role at low temperatures, and the crossover from VRH to ES-hopping should be observed below a certain critical temperature. For highly boron-doped single crystal diamond, insulating samples close

to the metal-insulator transition exhibit VRH and no crossover to Efros-Shklovskii VRH could be seen, probably due to the decrease of the T_0 value when approaching the metal-insulator transition [18] (see Chap. 2.3). A crossover from VRH to Efros-Shklovskii VRH has recently been reported by Tshepe et al. in boron-ion-implanted films [17] as well as by Sato et al. in a lower-doped single crystal diamond [30]. The theoretical value of $T_{0,ES}$ for Efros-Shklovskii VRH in Eq. 3.1 is given by

$$T_{0,ES} = \frac{e^2\beta}{4\pi k_B \epsilon_0 \epsilon_r \xi} \tag{3.2}$$

with ϵ_r the relative permittivity and ξ the localization length (decay length of wave function for isolated impurity atoms). The coefficient β is equal to 2.8 according to Shklovskii [24] or equal to 0.57 according to Adkins [31]. Taking $\epsilon_r = 5.7$, $\beta = 2.8$, and $\xi = 0.3\ nm$ as the effective Bohr radius of the boron acceptor in diamond [32], one obtains for $n \ll n_c$ $T_{0,ES} = 2.7 \times 10^4\ K$. From the fit of the low temperature transport data of the low doped samples Bus100 and Bmec2500 we find $T_{0,ES}$ values of the order of 3000 K (see Fig. 3.5 (a)), which is a factor of 9 smaller than the theoretically predicted value. A discrepancy of a factor 5 can be explained by the choice of the value β. Another possibility is the scaling of $T_{0,ES}$ when approaching the metal-insulator transition[17], or a temperature-induced smearing of the Coulomb gap [33, 34].

An Efros-Shklovskii hopping conductivity over a wide range of temperatures has also been found in metallic and semiconducting granular arrays [35, 36, 37, 38, 39, 40, 41]. This temperature dependence has been a puzzle for a long time, and a detailed understanding was only recently achieved (see Ref. 42 and references therein). Multiple cotunneling processes can lead to Efros-Shklovskii-like variable range hopping in granular metal arrays with weak intergrain coupling [41, 43, 44]. For quantum dot arrays, random charging of dots and long range Coulomb interactions create a soft Coulomb gap [45].

The physical quantities characterizing a granular material are the intragranular conductance g_0, the intergranular (tunneling) conductance g (both g_0 and g dimensionless conductance (corresponding to one spin component) and measured in the units of the quantum conductance $e^2/\hbar$: $g = G/(2e^2/\hbar)$ with G the conductance ($[G] = \Omega^{-1}$).), the charging energy $E_c = e^2/4\pi k_B \epsilon_0 \epsilon_r d$ (d is the grain size), and the mean level spacing $\delta = (\nu V)^{-1}$ with ν the density of states and V the volume of the grain (notation used as in Ref. 42, ν should not be confused with the critical exponent used before). A "granular system" is obtained in the limit $g \ll g_0$, whereas the case $g \sim g_0$ can be viewed as a homogeneously disordered system. Samples with $g > g_c$ exhibit metallic

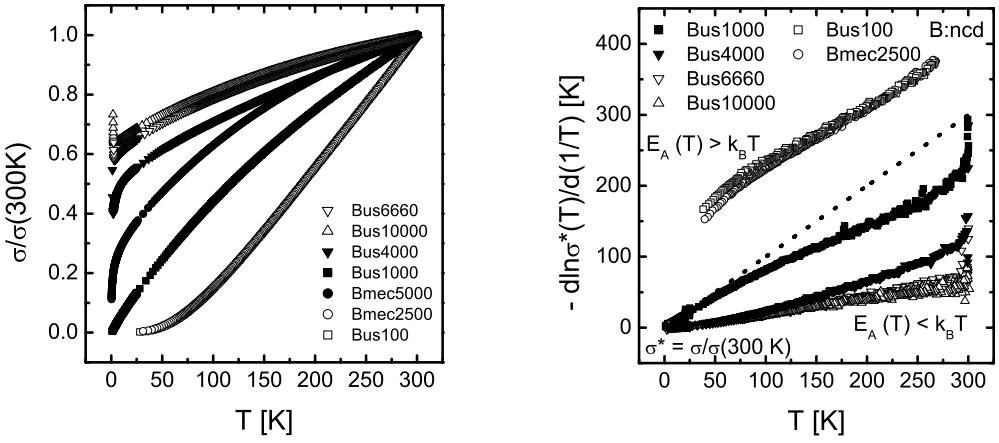

(a) (b)

Figure 3.4.: (a) Temperature dependence of the normalized conductivity $\sigma/\sigma(300K)$ for several samples in the range 300 K down to 350 mK. The highly doped sample with $n_B = 3.3\ 10^{21} cm^{-3}$ also shows superconductivity with a critical temperature $T_c = 2.6K$; (b) Temperature dependence of the slope of the Arrhenius plots for the same samples. The Ioffe criterion as explained in detail in the text suggests a crossover from a thermally activated transport and, thus, insulating regime to a metallic regime. The critical concentration n_c for this crossover is estimated to be about $3 \times\ 10^{20} cm^{-3}$ as determined from SIMS.

transport whereas samples with $g < g_c$ show insulating behaviour, corresponding to metallic grains with strong and weak intergrain coupling, respectively. Here, g_c is the critical conductance which is related to E_c and δ as

$$g_c = (1/2\pi D) \ln(E_c/\delta) \tag{3.3}$$

where D is the dimensionality [42]. For a grain size $d \approx 150\ nm$ and a typical density of states $\nu \approx\ 10^{20}\ eV^{-1} cm^{-3}$ one gets $E_c \approx 20K$ and $\delta \approx 1mK$. One could expect two-dimensional effects, as the grain size is of the same order of magnitude as the thickness and, thus, $g_c \approx 0.52$ or $g_c \approx 0.77$ for a three-dimensional or two-dimensional system. These values lie between the estimated conductances for samples Bus100 and Bus1000 (see Tab. 3.1). This is in good agreement with the criterion of effective activation energy used above to determine the metal-insulator transition in this material (see Fig. 3.4 (b)).

As already mentioned above, for $g < g_c$ insulating behaviour is predicted following an Efros-Shklovskii variable range hopping, which is observed in nanocrystalline

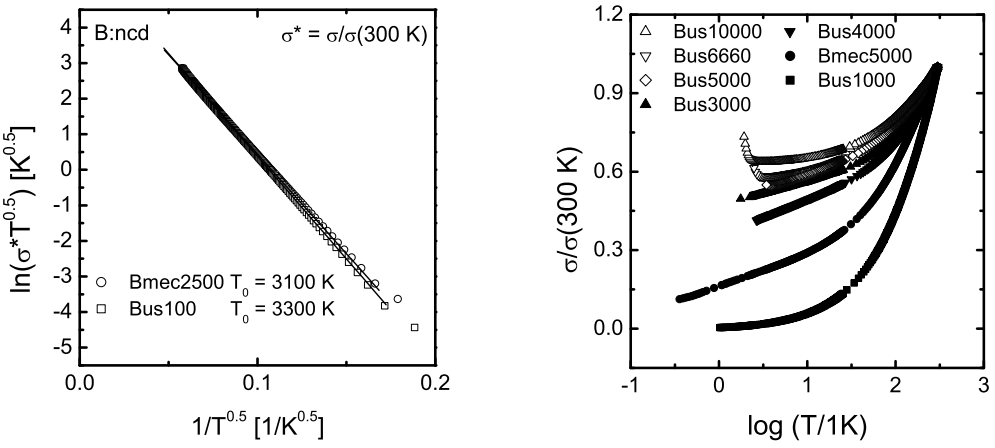

(a) (b)

Figure 3.5.: (a) Temperature dependence of the normalized conductivity for the low doped samples Bus100 and Bmec2500, following a Efros Shklovskii type of hopping dependence over a wide range of temperatures. The T_0 values of both samples are indicated; (b) Logarithmic temperature dependence of the normalized conductivity for several highly doped samples as expected for a granular metal. The deviations are explained in detail in the text.

diamond over a wide temperature range (see Fig. 3.5 (a)). An estimate of the localization length ξ from the experimentally determined T_0 values gives $\xi \approx 1\ nm$, which corresponds to localization within one grain. This result is important because larger values would imply strongly coupled clusters of grains.

For samples with $g > g_c$, several contributions to the conductivity can be seen, depending on the temperature range (see Ref. 42 and references therein). For temperatures $T > \Gamma$ ($\Gamma = g\delta$ can be interpreted as the width of the smearing of the energy levels in the grains), one should find a logarithmic temperature dependence (for two- as well as three-dimensional systems) of the conductivity [42]:

$$\sigma_T = \sigma_0 \left(1 - \frac{1}{\pi z g}\right) ln \left[\frac{g E_c}{T}\right] = a + b ln(T) \tag{3.4}$$

with z the coordination number of the arbitrary periodic lattice (E_c taken in Kelvin, or T in units of Kelvin).

This behaviour has been reported for several granular metallic systems [37, 46, 47, 48, 49]. As can be seen in Fig. 3.5 (b), some of the nanocrystalline samples show a logarithmic temperature dependence at low temperatures. A crossover to superconducting

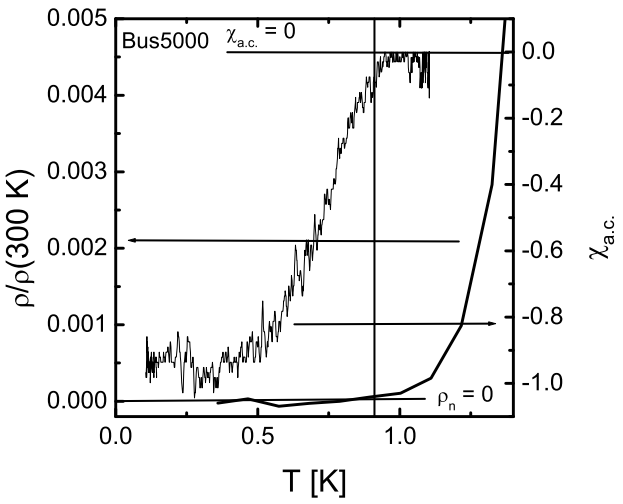

Figure 3.6.: Zoom of the temperature dependence of the normalized resistance $\rho/\rho(300K)$ for the highly boron-doped nanocrystalline sample Bus5000 with $n_B = 2.4 \times 10^{21}\ cm^{-3}$, compared to the diamagnetic response obtained from a.c. susceptibility measurements. The onset of diamagnetic screening corresponds to the transition to zero resistance.

behaviour occurs for the highly conducting samples (Bus4000 to Bus10000). The temperature at which the deviation from the logarithmic temperature dependence takes place increases with doping. Electron-electron interaction is responsible for the logarithmic temperature dependence, at higher temperatures interactions with phonons lead to a power law dependence (whole temperature range for Bus1000). No clear logarithmic temperature dependence can be seen for samples Bus6660 and Bus10000 (see Fig. 3.5 (b)). One possibilty is that the intergranular conductance g increases with doping. Therefore, one reaches $g \sim g_0$, and these samples should be treated as a homogeneously disordered system. The decrease in conductivity at low temperatures can be explained by localization effects and electron-electron interactions typical for disordered metals (see Ref. 50 and references therein), leading to

$$\sigma_T = \sigma_0 + A \times T^{1/2} + B \times T^{p/2} \tag{3.5}$$

where p is an index depending on scattering mechanism [50], and σ_0 the finite conductivity extrapolated to zero temperature, in good agreement with the experimental data. As will be seen in the next Chapter, very highly conductive nanocrystalline samples show similar superconducting properties as the single crystal diamond samples studied before, whereas nanocrystalline diamond samples close to the metal-insulator

transition exhibit a more rich behaviour. An increase in intergranular conductance g with doping could indeed account for this resemblance as pointed out above.

The highly-doped metallic nanocrystalline diamond films undergo a superconducting transition at low temperatures, as was recently reported by another group [8, 20, 21, 22]. This group used as criterion for superconductivity the transition to zero resistance alone which is not a sufficient, but a necessary condition. However, due to the small volume specific heat measurements are not even imaginable, but until now even the magnetic response has not been measured. Fig. 3.6 compares the temperature dependence of the normalized resistance $\rho/\rho(300K)$ for the highly boron-doped nanocrystalline sample Bus5000 with $n_B = 2.4 \times 10^{21}\ cm^{-3}$ with the diamagnetic response obtained from a.c. susceptibility measurements. The onest of diamagnetic screening correspond to the transition to zero resistance, clearly indicating a response of the bulk rather than a shortcircuiting due to a superconduting filamentary pathway.

3.3. Magnetoresistance and phase diagram of heavily boron-doped nanocrystalline diamond thin films

As already mentioned, the physical quantities characterizing a granular material are the intragranular conductance g_0, the intergranular (tunneling) conductance g, the charging energy $E_c = e^2/4\pi k_B \epsilon_0 \epsilon_{0r} d$ (d is the grain size), and the mean level spacing $\delta = (\nu V)^{-1}$ (ν is the density of states and V the volume of the grain) [42]. A "granular system" is obtained in the limit $g \ll g_0$ whereas the case $g \sim g_0$ can be viewed as a homogeneously disordered system. Samples with $g \ll 1$ are insulating while samples with $g \gg 1$ are metallic. If the constituent grains are made of a superconducting material, the behaviour of such a system can be quantified by adding one more energy parameter, the superconducting gap Δ of the material of a single grain. The interplay between Josephson coupling J and and grain charging Coulomb energy E_c determine whether global macroscopic superconductivity is built up in the sample or not.

Fig. 3.7 (a) shows the magnetoresistance for sample Bus6660 at several constant temperatures. With increasing magnetic field superconductivity is broken, the onset is shifted to lower magnetic field values with increasing temperature. This behaviour is quantitativly similar to results obtained on equivalent heavily boron-doped single crystal diamond films. In the inset of Fig. 3.7 (b) the superconducting transition in zero field is shown, from the phase diagram $H_{c2}(T)$ a critical magnetic field of about 2.5 T is estimated, similar to single crystal diamond in the same doping range.

The superconducting properties of a granular system are in many ways determined by the properties of the granules of which is it formed. The superconducting gap Δ exists in each grain and its value is close to the gap magnitude in the bulk, provided $\Delta \gg \delta$ [42]. Anderson showed that the superconducting gap is suppressed or can even be fully destroyed if the latter inequality is not satisfied [51, 52], which has been confirmed experimentally [53, 54, 55]. In our case, $\delta = (\nu V)^{-1} \approx 1mK$ and $\Delta \approx 300\mu V = 3.6$ K [56] and, thus, these effects can be neglected. Sufficiently strong coupled grains ($g \gg 1$) can maintain (global) superconducting coherence because the coupling reduces the phase fluctuations. Based on the ideas of Anderson, the interplay between Josephson coupling $J = \pi g\Delta/2$ and Coulomb charging energy E_c was suggested by Abeles [57] to identify whether superconductivity can exist in a granular system, indicating a large interval of conductances $E_c/\Delta = g_s \ll g \ll 1$ where superconductivity should exist while the corresponding normal array represents an insulating state. The Anderson-Abeles criterion was found to be in conflict with many experiments [58, 59, 60, 61]. It was found that the superconductor-insulator transition (in granular as well as homogeneously disordered films) is determined by the normal-state resistance with a critical value $R_0 = h/(2e^2)^2 \approx 6.4\ k\Omega$ rather than the ratio of the Josephson and Coulomb energies [62, 63, 64]. From the theoretical point of view this corresponds to a resistively shunted Josephson junction [65, 66, 67], a phenomenological resistive term in the coupling was applied to granular systems leading to the same result [68, 69, 70]. This dissipative coupling was identified with direct electron tunneling processes between grains in addition to Josephson couplings [71].

In the approach of Chakravarty et al. (see Ref. 71) the originally strong Coulomb interaction is reduced by the electron tunneling to other grains. This renormalization corresponds to the screening of the Coulomb interaction by free charges usually seen in metals. In the case of strong coupling ($g \gg 1$) and strong Coulomb interaction ($E_c \gg \Delta$) the charging energy is renormalized to $\approx \Delta/g$. Therefore, for $g \gg 1$ the effective Coulomb energy is always smaller than the Josephson coupling $J \approx g\Delta$, and superconductivity occurs at sufficiently low temperatures [72, 73]. With $E_c \approx 20$ K this is the case of sample Bus6660, as can be seen in Fig. 3.7(a). Low temperature transport measurements have shown that these samples are in the homogeneously disordered limit $g \approx g_0$, and, thus, the BCS theory should be a good starting point to describe the granular system, in good agreement with our experimental data, and comparing equivalent nanocrystalline and single crystal diamond films.

Fig. 3.8 (a) shows the magnetoresistance of sample Bus4000 at several constant low

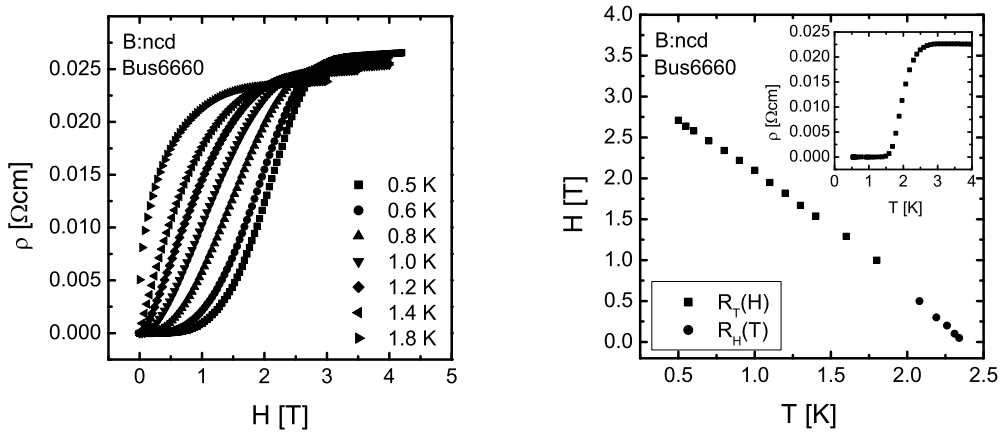

(a) (b)

Figure 3.7.: (a) Magnetoresistance for sample Bus6660 at several constant temperatures, similar to results obtained on equivalent heavily boron-doped single crystal diamond films. For sample Bus6660 $g \approx g_0 \gg 1$ holds and the properties are not very different from those of the bulk superconductor; (b) The inset shows the temperature dependence of the resistivity in the vicinity of the superconducting transition. The phase diagram obtained from temperature sweeps at constant magnetic field ($R_T(H)$) and magnetic field sweeps at constant temperature ($R_H(T)$) indicate a critical magnetic field H_{c2} of about 2.5 T comparable to values obtained in single crystal material.

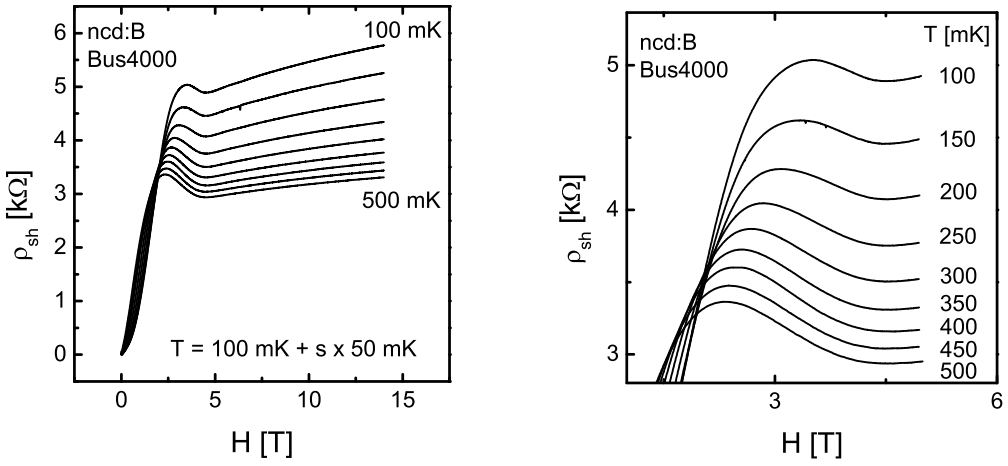

(a) (b)

Figure 3.8.: (a) Magnetoresistance of sample Bus4000 at several constant temperatures, revealing regions with negative and positive magnetoresistance, respectively; (b) Zoom in of the graph show in (a).

temperatures in the range from 100 up to 500 mK and with perpendicular fields up to 14 T. Bulk superconductivity (superconducting grains) is destroyed by application of extremely strong fields, the positive magnetoresistance in the high-field limit resembles the behaviour seen in metallic single crystal and nanocrystalline diamond films [4, 8]. By decreasing the magnetic field, a region with negative magnetoresistance is found. Only at sufficiently weak magnetic fields the resistivity starts to decrease and the sample displayed superconducting behaviour. Similar behaviours have been reported in other granular systems [38, 74, 75]. In Fig. 3.8 (b) a zoom into the region of the negative magnetoresistance is shown, also showing the crossing point.

Negative magnetoresistance due to weak localization can play a role in disordered metals [50, 76], but the characteristic magnetic fields are several Tesla, such that all weak-localization effects are strongly suppressed. Beloborodov et al. explained the negative magnetoresistance of a granular metal by the suppression of the density of states (DOS) due to superconducting fluctuations [77].

The theory of superconducting fluctuations near the transition into the superconduting state was developed long ago (see Ref. 78 and references therein). One fluctuation contribution comes from nonequilibrium Cooper pairs forming a new transport channel ($\delta\sigma_{AL}$) [79], and another comes from coherent scattering of electrons forming a Cooper pair on impurities ($\delta\sigma_{MT}$)[80, 81, 82]. Both corrections enhance the conductivity and lead to a positive magnetoresistance. The formation of nonequilibrium Cooper pairs results in a fluctuational gap in the one-electron spectrum [83]. This suppression of the density of states has been shown to lead to a correction of the conductivity $\delta\sigma_{DOS}$ [77]. While in conventional superconductors $\delta\sigma_{Asl}$ and $\delta\sigma_{MT}$ are more important than $\delta\sigma_{DOS}$, in granular systems the DOS correction plays a very important role [77, 84]. The conductivity $\delta\sigma_{DOS}$ is negative and its absolute value decreases with increasing magnetic field, thus leading to the negative magnetoresistance. This is what is seen for sample Bus4000 in Fig. 3.8. One should keep in mind that for sample Bus4000 g is close to one, approaching the quantum resistance $R_0 = \hbar/(2e)^2 \approx 6.4\ k\Omega$ for which a superconductor-insulator transition is expected. In the case of a superconductor-insulator transition, similar behaviours of the magnetoresistance have been reported [85, 86, 87]. The origin of such a transition is still under debate. Some theories claim that it may be understood in terms of Cooper-pair scattering out of the superconducting condensate into a Bose-glass [88, 89], others claim that a percolation description of the superconductor-insulator transition is more adequate [90].

Bibliography

[1] O.A. Williams, O. Douhéret, M. Daenen, K. Haenen, E. Osawa, and M. Takahashi, Chem. Phys. Lett. **445**, 255 (2007).

[2] W. Gajewski, private communication.

[3] A.C. Ferrari and J. Robertson, Phys. Rev. B **61**, 14095 (2000).

[4] E. Bustarret, E. Gheeraert, and K. Watanabe, phys. stat. sol. (a) **199**, 9 (2003).

[5] P. Gonon, E. Gheeraert, A. Deneuville, F. Fontaine, L. Abello, and G. Lucazeau, J. Appl. Phys. **78**, 7059 (1995).

[6] J.W. Ager, W. Walukiewicz, M. McCluskey, M.A. Plano, and M.I. Landstrass, Appl. Phys. Lett. **66**, 616 (1995).

[7] Y. Wang, H. Li, Z. Lin, and K. Feng, Jpn. J. Appl. Phys. **39**, 2795 (2000).

[8] M. Nesládek, D. Tromson, C. Mer, P. Bergonzo, P. Hubik, and J.J. Mares, Appl. Phys. Lett. **88**, 232111 (2006).

[9] E.A. Ekimov, V.A. Sidorov, E.D. Bauer, N.N. Mel'nik, N.J. Curro, J.D. Thompson, and S.M. Stishov, Nature **428**, 542 (2004).

[10] Y. Takano, M. Nagao, L. Sakaguchi, M. Tachiki, T. Hatano, K. Kobayashi, H. Umezawa, and H. Kawarada, Appl. Phys. Lett. **85**, 2851 (2004).

[11] K. Winzer, D. Bogdanov, and Ch. Wild, Physcia C **432**, 65 (2005).

[12] E. Bustarret, J. Kacmarcik, C. Marcenat, E. Gheeraert, C. Cytermann, J. Marcus, and T. Klein, Phys. Rev. Lett. **93**, 237005 (2004).

[13] V.A. Sidorov, E.A. Ekimov, S.M. Stishov, E.D. Bauer, and J.D. Thompson, Phys. Rev. B **71**, 060502(R) (2005).

[14] Z.L. Wang, Q. Luo, L.W. Liu, C.Y. Li, H.X. Yang, H.F. Yang, J.J. Li, X.Y. Lu, Z.S. Jin, L. Lu, and C.Z. Gu, Diam. Rel. Mat. **15**, 659 (2006).

[15] E. Bustarret, P. Achatz, B. Sacépé, C. Chapelier, C. Marcenat, L. Ortéga, and T. Klein, Phil. Trans. R. Soc. A **366**, 267 (2008).

[16] E. Bustarret, phys. stat. sol. (a) **205** 997 (2008).

[17] T. Tshepe, C. Kasl, J.F. Prins, and M.J.R. Hoch, Phys. Rev. B **70**, 245107 (2004).

[18] T. Klein, P. Achatz, J. Kacmarcik, C. Marcenat, F. Gustafsson, J. Marcus, E. Bustarret, J. Pernot, F. Omnès, Bo E. Sernelius, C. Persson, A. Ferreira da Silva, and C. Cytermann, Phys. Rev. B **75**, 165313 (2007).

[19] K. Thonke, Semicond. Sci. Technol. **18**, S20 (2003).

[20] J.J. Mares, P. Hubík, M. Nesládek, D. Kindl, and J. Kristofik, Diam. Rel. Mat. **15**, 1863 (2006).

[21] J.J. Mares, M. Nesládek, P. Hubík, D. Kindl, and J. Kristofik, Diam. Rel. Mat. **16**, 1 (2007).

[22] J.J. Mares, M. Nesládek, P. Hubík, and J. Kristofik, Diam. Rel. Mat. **16**, 921 (2007).

[23] H. Fritzsche and M. Pollak, *Hopping and Related Phenomena* (World Scientific, Singapore, 1989).

[24] B.I. Shklovskii and A.L. Efros, *Electronic Properties of Doped Semiconductors* (Springer-Verlag, Berlin, 1988).

[25] A. Miller and E. Abrahams, Phys. Rev. **120**, 745 (1960).

[26] N.F. Mott, J. Non-Cryst. Solids **1**, 1 (1968).

[27] M. Pollak, Philos. Mag. **23**, 519 (1971).

[28] A.L. Efros and B.I. Shklovskii, J. Phys. C **8**, L49 (1975).

[29] A.L. Efros and B.I. Shklovskii, J. Phys. Solid State Phys. **9**, 2021 (1976).

[30] T. Sato, K. Ohashi, H. Sugai, T. Sumi, K. Haruna, H. Maeta, N. Matsumoto, and H. Otsuka, Phys. Rev. B **61**, 12970 (2000).

[31] C.J. Adkin, J. Phys.: Condens. Matter **1**, 1253 (1989).

[32] A.T. Collins, *The Physics of Diamond* (IOS Press, Amsterdam, 1997).

[33] I. Shlimak, M. Kaveh, R. Ussyshbin, V. Ginodman, S. D. Baranovskii, P. Thomas, H. Vaupel, and R. W. van der Heijden, Phys. Rev. Lett. **75**, 4764 (1995).

[34] N.F. Mott and M. Kaveh, Adv. Phys. **34**, 329 (1985); 34, 367 (1985).

[35] B. Abeles, P. Sheng, M.D. Coutts, and Y. Arie, Adv. Phys. **24**, 407 (1975).

[36] T. Chui, G. Deutscher, P. Lindenfeld, and W.L. McLean, Phys. Rev. B **23**, 6172 (1981).

[37] R.W. Simon, B.J. Dalrymple, D. Van Vechten, W.W. Fuller, and S.A. Wolf, Phys. Rev. B **36**, 1962 (1987).

[38] A. Gerber, A. Milner, G. Deutscher, M. Karpovsky, and A. Gladkikh, Phys. Rev. Lett. **78**, 4277 (1997).

[39] D. Yu, C. Wang, B.L. Wehrenberg, and P. Guyot-Sionnest, Phys. Rev. Lett. **92**, 216802 (2004).

[40] H.E. Romero and M. Drndic, Phys. Rev. Lett. **95**, 156801 (2005).

[41] T.B. Tran, I.S. Beloborodov, X.M. Lin, T.P. Bigioni, V.M. Vinokur, and H.M. Jaeger, Phys. Rev. Lett. **95**, 076806 (2005).

[42] I.S. Beloborodov, A.V. Lopatin, V.M. Vinokur, and K.B. Efetov, Rev. Mod. Phys. **79** 469 (2007).

[43] M.V. Feigel'man and A.S. Ioselevich, JETP Lett. **81**, 227 (2005).

[44] I.S. Beloborodov, K.B. Efetov, A.V. Lopatin, and V.M. Vinokur, Phys. Rev. B **71**, 184501 (2005).

[45] J. Zhang and B.I. Shklovskii, Phys. Rev. B **70**, 115317 (2004).

[46] A. Gerber, J. Phys.: Condens. Matter **2** 8161 (1990).

[47] C. Radhakrishnan, C.K. Subramaniam, S. Sankaranaranyanan, G.V.S. Rao, and R. Srinivasen, Physica C **167**, 53 (1990).

[48] H. Fujimori, S. Mitani, S. Ohnuma, T. Ikeda, T. Shima, and T. Matsumoto, Mater. Sci. Eng. A **181-182**, 897 (1994).

[49] L. Rotkina, S. Oh, J.N. Eckstein, and S.V. Rotkin, Phys. Rev. B **72**, 233407 (2005).

[50] P.A. Lee and T.V. Ramakrishnan, Rev. Mod. Phys. **57** 287 (1985).

[51] P.W. Anderson, J. Phys. Chem. Solids **1**, 26 (1959).

[52] P.W. Anderson, *Lectures on the Many-Body problem* (Academic, New York, 1964).

[53] D.C. Ralph, C.T. Black, and M. Tinkham, Phys. Rev. Lett. **74**, 3241 (1995).

[54] C.T. Black, D.C. Ralph, and M. Tinkham, Phys. Rev. Lett. **76**, 688 (1996).

[55] D. Davidovic and M. Tinkham, Phys. Rev. Lett. **83**, 1644 (1999).

[56] B. Sacépé, C. Chapelier, C. Marcenat, J. Kacmarcik, T. Klein, M. Bernard, and E. Bustarret, Phys. Rev. Lett. **96**, 097006 (2006).

[57] B. Abeles, Phys. Rev. B **15**, 2828 (1977).

[58] B.G. Orr, H.M. Jaeger, and A.M. Goldman, Phys. Rev. B **32**, 7586 (1985).

[59] B.G. Orr, H.M. Jaeger, A.M. Goldman, and C.G. Kuper, Phys. Rev. Lett. **56**, 378 (1986).

[60] H.M. Jaeger, D.B. Haviland, A.M. Goldman, and B.G. Orr, Phys. Rev. B **34**, 4920 (1986).

[61] H.M. Jaeger, D.B. Haviland, B.G. Orr, and A.M. Goldman, Phys. Rev. B **40**, 182 (1989).

[62] Y. Liu, D.B. Haviland, B. Nease, and A.M. Goldman, Phys. Rev. Lett. **47**, 5931 (1993).

[63] N. Markovic, C. Christiansen, A.M. Mack, W.H. Huber, and A.M. Goldman, Phys. Rev. B **60**, 4320 (1999).

[64] A. Frydman, O. Naaman, and R.C. Dynes, Phys. Rev. B **66**, 052509 (2002).

[65] A. Schmid, Phys. Rev. Lett. **51**, 1506 (1983).

[66] S. Bulgadaev, JETP Lett. **39**, 314 (1984).

[67] G. Schön and A. Zaikin, Phys. Rep. **198**, 237 (1990).

[68] S. Chakravarty, G.L. Ingold, S. Kivelson, and A. Luther, Phys. Rev. Lett. **56**, 2303 (1986).

[69] M.P.A. Fisher, Phys. Rev. Lett. **57**, 885 (1986).

[70] E. Simánek and R. Brown, Phys. Rev. B **34**, 3495 (1986).

[71] S. Chakravarty, S. Kivelson, G.T. Zimanyi, and B.I. Halperin, Phys. Rev. B **35**, 7256 (1987).

[72] A.I. Larkin and Y.N. Ovchinnikov, Phys. Rev. B **28**, 6281 (1983).

[73] U. Eckern, G. Schön, and V. Ambegaokar, Phys. Rev. B **30**, 6419 (1984).

[74] V.F. Gantmakher, M. Golubkov, J.G.S. Lok, and A. Geim, JETP Lett. **82**, 951 (1996).

[75] R. Parthasarathy, X.-M. Lin, K. Elteto, T.F. Rosenbaum, and H.M. Jaeger, Phys. Rev. Lett. **92**, 076801 (2004).

[76] B.L. Altshuler, D.E. Khmel`nitskii, A.I. Larkin, and P.A. Lee, Phys. Rev. B **22**, 5142 (1980).

[77] I.S. Beloborodov and K.B. Efetov, Phys. Rev. Lett. **82**, 3332 (1999).

[78] A.I. Larkin and A. Varlamov, *Theory of Fluctuations in Superconductors* (Oxford University Press, New York, 2005).

[79] L.G. Aslamazov and A.I. Larkin, Sov. Phys. Solid State **10**, 875 (1968).

[80] K. Maki Prog. Theor. Phys. **39**, 897 (1968)

[81] K. Maki Prog. Theor. Phys. **40**, 193 (1968).

[82] R.S. Thompson, Phys. Rev. B **1**, 327 (1970).

[83] E. Abrahams, M. Redi, and J. Woo, Phys. Rev. B **1**, 208 (1970).

[84] I.S. Beloborodov, K.B. Efetov, and A.I. Larkin, Phys. Rev. B **61**, 9145 (2000).

[85] A.F. Hebard and M.A. Paalanen, Phys. Rev. Lett. **65**, 927 (1990).

[86] M.A. Paalanen, A.F. Hebard, and R.R. Ruel, Phys. Rev. Lett. **69**, 1604 (1992).

[87] N. Mason and A. Kapitulnik, Phys. Rev. Lett. **82**, 5341 (1999)

[88] M.P.A. Fisher, Phys. Rev. Lett. **65**, 923 (1990)

[89] E.S. Sorensen, M. Wallin, S.M. Girvin, and A.P. Young, Phys. Rev. Lett. **69**, 828 (1992)

[90] Y. Dubi, Y. Meir, and Y. Avishai, Phys. Rev. B **71**, 125311 (2005).

4. Superconductivity in heavily boron-doped cubic silicon

As already mentioned, superconductivity has been found very early in several doped semiconductors such as GeTe, PbTe, and $SrTiO_3$ and with characteristics that confirmed the idea of an (phonon-mediated) attractive interaction between electrons pointed out in the BCS theory [1, 2, 3]. Theoretical calculations have predicted that germanium [4] as well as silicon [5, 6] should become superconducting upon doping in their face-centered cubic (diamond) structure. However, at the beginning of this thesis superconductivity had only been found in silicon in its $\beta - Sn$ and hexagonal metallic phases obtained under extreme pressures of the order of 10 GPa [7, 8, 9]. With the discovery of superconductivity in highly boron-doped diamond [10] as well as in silicon clathrates [5, 11, 12], renewed interest came up for group IV elements. For sufficiently high boron doping, silicon becomes metallic, but the calculations showed that it was necessary to incorporate boron well above its thermodynamical solubility (via out of equilibrium processes [13]) in order to reach superconducting properties at a well observable scale [14].

4.1. Sample preparation and structural properties of heavily boron-doped cubic silicon

The ongoing miniaturization in CMOS technologies reaching the sub 0.1 μm regime requires the realization of box-like ultra-shallow highly-doped junctions [15]. In this context, the International Technology Roadmap for Semiconductors (ITRS) suggested laser processing techniques as potential candidates [16, 17, 18], in contrast to the existing technologies such as rapid thermal annealing or spike annealing (posterior to an ion implantation step) [19]. The laser doping technique can be classified into two main categories: laser thermal processing (LTP) and gas immersion laser doping (GILD). Common to both techniques, a pulsed laser beam induces a melting/solidification cy-

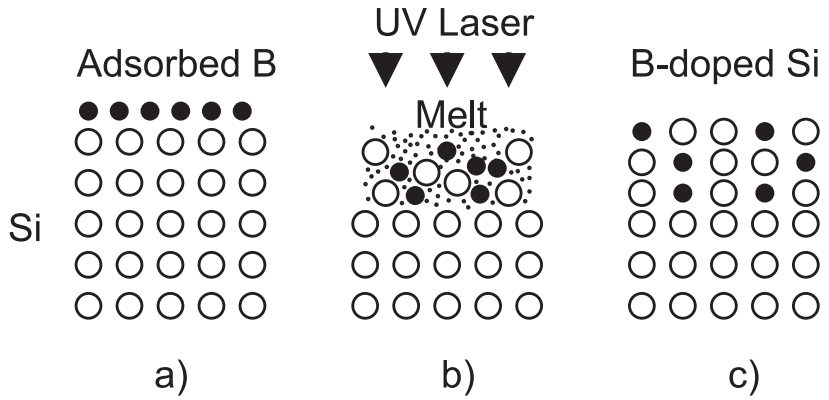

Figure 4.1.: Diagrams of the three initial steps of gas immersion laser doping: (a) adsorption of BCl_3 on the silicon wafer surface, (b) local surface melting of silicon induced by a laser shot, and (c) formation of the Si:B layer upon cooling.

cle over a depth which is mainly controlled by the laser energy density (see Fig. 4.1). In the LTP case, dopants are ion implanted before the laser processing, whereas in the GILD case, the dopants are chemisorbed on the silicon substrate surface prior to the laser shot (see Fig. 4.1 (b)). As shown in Fig. 4.1 (c), during the solidification period, the molten silicon grows epitaxially from the underlying crystalline silicon. The diffusion coefficient of dopant atoms in liquid silicon is several orders of magnitude larger than in solid silicon, and dopants may diffuse over the whole melted depth. The solidification has to be too fast for boron atoms to pair up (or cluster) near the interface, but has also to be slow enough so that the liquid phase epitaxy at the interface is perfect. The dopants are set in substitutional sites at concentrations well above their solubility limit (in silicon about $6 \times 10^{20}\ cm^{-3}$ [20, 21, 22]) due to the high velocity of the solidification process. The laser-doped layer is limited to the melted region and, thus, highly-doped box-like structures are possible to be realized.

Gas immersion laser doped silicon samples have been prepared by D. Débarre and J. Boulmer of the Institut d'Electronique Fondamentale (Université Paris Sud and CNRS) in Paris, France [13, 23, 24]. Laser processing takes place in a high vacuum chamber with a 10^{-7} mbar base pressure. After cleaning and removing the native oxide, the {100}-oriented silicon substrate is introduced in the chamber. In a special GILD configuration, ten separate $2 \times 3\ mm^2$ areas of the same wafer have been processed. A homogenized XeCl excimer laser with a wavelength $\lambda = 308\ nm$ was used, the melting/solidification cycle was repeated 200 times with a duration of 25 ns of each laser pulse. As dopant precursor gas BCl_3 was injected and chemisorbed on the substrate surface prior to each laser shot. The laser is thereby triggered after each

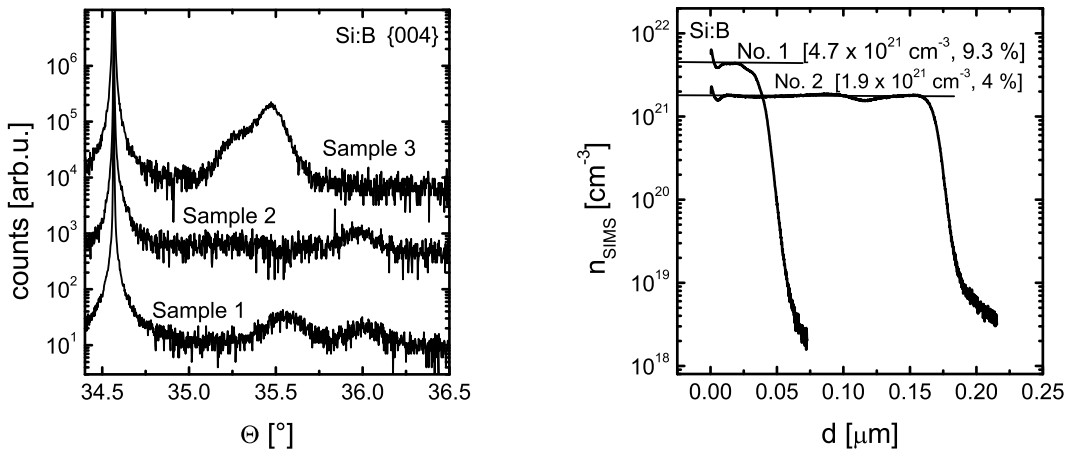

(a) (b)

Figure 4.2.: (a) High resolution X-ray diffraction measurements of three Si:B superconducting samples along the Bragg reflection (004); (b) Secondary ion mass spectroscopy depth profile of samples 1 and 3, with boron concentrations of about $n_B = 4.7$ and 1.9×10^{21} cm^{-3}, respectively.

gas injection pulse with a time delay of the order of 10 ms. The power and duration of the pulses were adjusted in order to ensure maximum doping over the whole thickness of the melt, based on the in situ monitoring of the transient reflectivity at 675 nm together with a previous calibration by secondary ion mass spectroscopy [24]. In the following we will focus on three of the samples without loss of generality.

The incorporation of boron in silicon leads as in the case of diamond to the formation of biaxially strained layers due to in-plane lattice matching [23, 24]. In contrast to boron-doped diamond, the lower covalent radius of boron with respect to that of silicon [25] results in a lattice contraction in the growth direction. In Fig. 4.2(a), the high resolution X-ray diffraction analysis along the (004) Bragg reflection of the three samples is shown. Beside the narrow line arising from the substrate, one or two broad diffraction peaks can be observed at higher diffraction angles corresponding to a lattice contraction in the growth direction. This indicates a non-uniform distribution of the strain perpendicular to the surface and, thus, of the boron content, but confirms the epitaxial single crystal character of the films. For instance, the two broad maxima of sample 1 situated at 35.56° and 36.02° correspond to a contraction of the lattice parameter a along the {001}-direction of $\Delta a/a = -2.5$ % and -3.7 %, respectively, and correspond to an isotropic lattice parameter variation of -1.4 % and -2.1 %. Application of Vegard's law as in the case of boron-doped diamond and previous

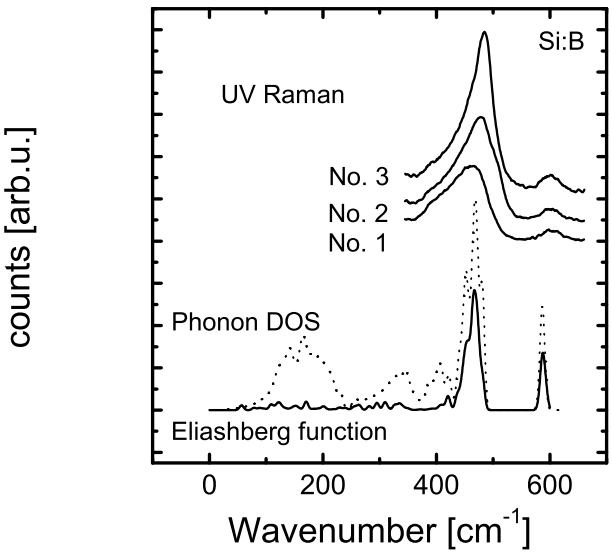

Figure 4.3.: UV-Raman spectra (325 nm) of the three Si:B samples in the 350 − 650 cm^{-1} range. Note that no signal from the silicon substrate could be detected due to the very small absorption length. Also shown are the Phonon density of states as well as the Eliashberg funtion as obtained from ab initio calculations in a supercell approximation [14].

calibrations, this corresponds to substitutional boron concentrations of 5.7 *at.* % (2.8×10^{21} cm^{-3}) and 8.4 *at.* % (4.2×10^{21} cm^{-3}), respectively [23, 24]. The XRD analysis shown in Fig. 2.11 indicates that sample 2 has a slightly lower boron concentration, whereas sample 3 has a much lower boron concentration than sample 1. This is in good agreement with secondary ion mass spectroscopy measurements presented in Fig. 4.2(b). The depth profile of samples 1 and 3 are shown, with boron concentrations of about $n_B = 4.7$ and $1.9 \times\ 10^{21}$ cm^{-3}, respectively, corresponding to 9.3 *at.* % and 4.0 *at.* %. The thickness of both samples are approximately 35 nm for sample 1 and 170 nm for sample 3. Hall effect measurements performed at room temperature on sample 1 give a free hole density of the order of $(5\pm2)\times10^{21}$ cm^{-3}, which is comparable to the higher boron concentration deduced above.

The Raman spectra of the three samples are shown in Fig. 4.3, clearly showing two features around 480 cm^{-1} and 600 cm^{-1}, respectively. The former corresponds to the zone-center optical mode of silicon and is shifted by about 40 cm^{-1} with respect to the peak position of 520 cm^{-1} found in pure silicon. The broadened Raman peaks agree well with the phonon density of states obtained from ab initio calculations [14]. This softening is caused by the large amount of free carriers, which more than compensates

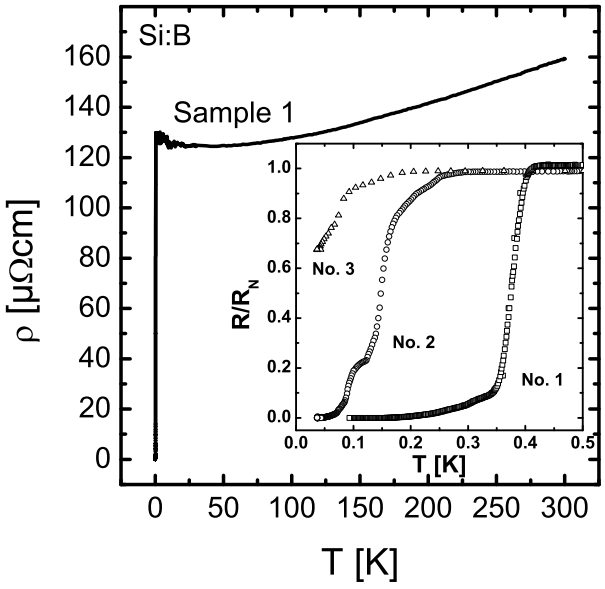

Figure 4.4.: Temperature dependence of the resistivity for the three Si:B samples, typical for a disordered metal. The inset shows the respective superconducting transition seen at low temperatures.

the effect of lattice contraction. Experimentally, the shift to lower frequency and the broadening are more pronounced for sample 1, which has the highest critical temperature T_c as will be shown later. The Raman active mode around $590-600\ cm^{-1}$ seen experimentally has been already reported in non-superconducting films [26, 27]. Ab initio calculations identify it with a Si-B stretching mode [14, 28]. This good match between theory and experiment further confirms the incorporation of boron on substitutional sites.

4.2. Superconductivity of heavily boron-doped cubic silicon at low temperatures

Fig. 4.4 shows the temperature dependence of the resistivity ρ of sample 1 from room temperature down to 350 mK, clearly showing metallic behaviour $d\rho/dT < 0$. The increase in resistance at low temperatures can be explained by localization effects and electron-electron interactions typical for disordered metals (see Ref. 29 and references therein), leading to

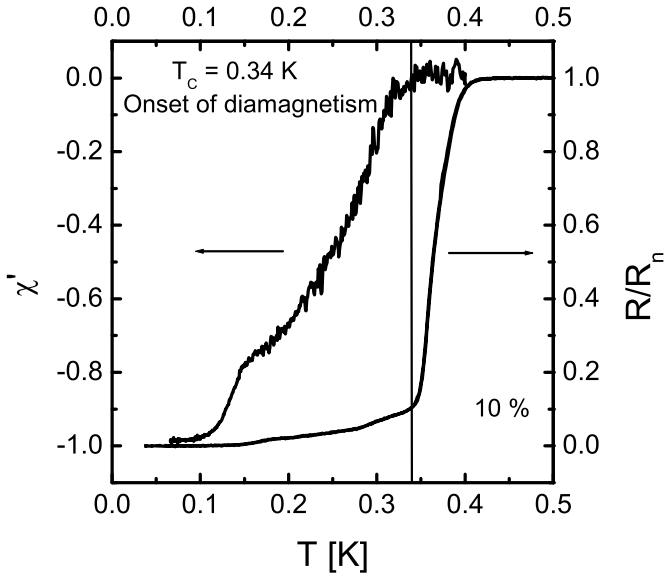

Figure 4.5.: Temperature dependence of the d.c. electrical resistivity (normalized to its normal state value) and of the real part of the a.c. susceptibility. The onset of diamagnetism at 0.34 K occurs at a value of 10 % of the normal state resistance, whereas full diamagnetic screening is not achieved until 150 mK.

$$\sigma_T = \sigma_0 + A \times T^{1/2} + B \times T^{p/2} \tag{4.1}$$

as was already pointed out for the case of highly boron-doped single crystal diamond samples [30]. The room-temperature sheet resistance of the three samples 1, 2, and 3 are 35, 17, and 8 Ω, respectively, while their resistivities are of the order of 0.1 $m\Omega cm$. As shown in the inset of Fig. 4.4, the temperature dependence of the normalized resistivity was measured for the three samples down to 30 mK in a dilution refrigerator. Samples 1 and 2 undergo superconducting transitions to zero resistance at 150 mK and 45 mK, respectively, whereas sample 3 only shows a partial transition. Hereby it should be noted that elemental boron cannot account for this superconducting transition as it only becomes superconducting under very high pressures of the order of 160 GPa [31].

The temperature dependence below 0.5 K of the electrical resistance R (d.c.) and of the real part of the a.c. magnetic susceptibility χ' is plotted in Fig. 4.5. A sharp drop of the resistance is observed with an onset around 0.4 K and an immeasurably small R value is observed below 150 mK as already mentioned above. Similarly, as the

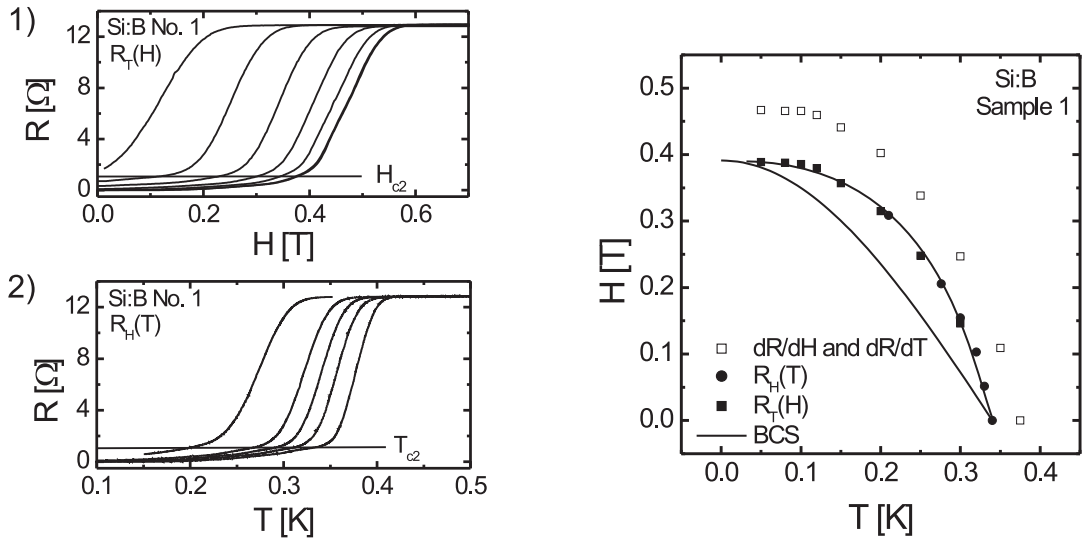

(a) (b)

Figure 4.6.: (a) (1) H_{c2} measured by magnetic field sweeps $R_T(H)$ at 50, 150, 200, 250, 300, and 350 mK; (2) T_{c2} measured by temperature sweeps $R_H(T)$ at magnetic fields of 0.1, 0.2, 0.3, 0.4, and 0.5 T; (b) Temperature dependence of the upper critical field H_{c2}, as obtained from the 10 % criterion. Open symbols represent the maxima of dR/dT and dR/dH. The solid line corresponds to classical theory.

temperature decreases there is an onset of diamagnetism below 0.34 K (corresponding to 10 % of the normal state resistance), but full magnetic screening is not achieved until 150 mK. These measurements unambiguosly demonstrate the occurence of superconductivity in sample 1. The foot of the resistive and diamagnetic transitions, as well as the width of the magnetic response, are typical of an inhomogeneous superconductor [32]. This inhomogeneity is expected, as already pointed out by the non-uniform boron distribution detected by XRD.

In order to define the phase diagram, electrical measurements have been performed. Fig. 4.6(a) (1) and Fig. 4.6(a) (2) show the temperature dependence of the resistance for various constant magnetic field values ($R_H(T)$, T-sweeps) or the magnetic field dependence of the resistance for various constant temperature values ($R_T(H)$, H-sweeps). The magnetic field is hereby applied perpendicular to the plane of the sample. The transitions remain sharp and no hysteresis or supercooling was seen. The relatively high value of the critical field $H_{c2}(T = 0K) \approx 0.4$ T, which exceeds that of lead (8×10^{-2} T), the strongest known type I superconductor, suggests that boron-doped silicon is a type II superconductor. The critical temperature T_{c2} and the critical

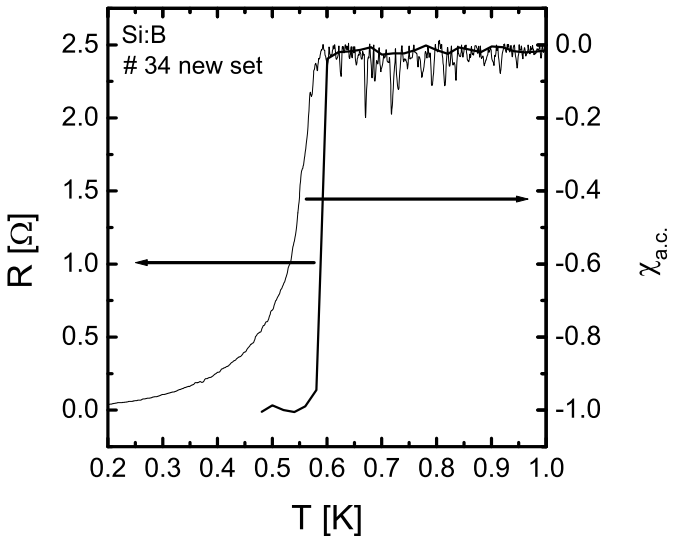

Figure 4.7.: Temperature dependence of the d.c. electrical resistivity (normalized to its normal state value) and of the real part of the a.c. susceptibility for a Si:B sample of the new series. The onset of diamagnetism occurs at 0.6 K, together with the transition to zero resistance.

magnetic field H_{c2} (taken at 10 % of the normal state value of the resistance which corresponds to the onset of diamagnetism in zero field) are plotted in Fig. 4.6(b). In order to get an idea of the width of the transition, the positions of maxima of the slope of the resistance versus temperature (dR/dT) in the T-sweeps as well as of maxima of dR/dH in the H-sweeps are also shown in Fig. 4.6(b). Compared to the standard BCS dependence, the critical field versus temperature curve has a marked curvature [33]. On the one hand, this observation could be due to the films inhomogeneity if, for instance, the dimensions of the superconducting regions are restricted parallel to the film surface or due to percolation or localization phenomena [34, 35]. On the other hand, the observed dependence could be explained by paramagnetic limitations if the carriers are assigned a gyromagnetic factor g 40 % larger than the standard value 2 [36]. One can use the phase diagram to estimate the coherence length ξ. Using the experimentally obtained slope of H_{c2} against temperature at T_c, an estimate in the so-called orbital limit yields $\xi = 13$ nm, whereas a larger estimate of approximately 20 nm is found based on the values T_c and $H_{c2}(0)$ (at zero temperature) within the standard BCS theory. Both values are not much smaller than the estimated thickness ((35 ± 5) nm) of the sample, which can also act to limit the extent of the coherence length [37].

Furthermore, ab initio supercell calculations have been performed in order to study the electronic, vibrational, and electron-phonon coupling properties of boron-doped silicon [14]. The calculated band structure resembles that of undoped silicon, the Fermi level is located approximately 0.5 eV below the top of the valence band (for a 6.25 % doping level). This confirms the degenerate nature of boron-doped silicon at such high dopant concentrations, as already seen for highly boron-doped single crystal diamond. Compared to diamond, most of the coupling originates from the optical modes [6, 38, 39]. By using the Eliashberg function (also shown in Fig. 4.3), an average over the Brillouin zone and phonon bands yields a coupling constant λ of about 0.28, which is in good agreement with results obtained within the virtual crystal approximation ($\lambda = 0.3$ for 5 % doped Si) [6]. For commonly used values of the screened Coulomb repulsion μ^* in the range 0.08 to 0.12, one obtains critical temperatures T_c in the range 0.5 to 0.03 K from the already mentioned McMillan formula [40]. This suggests that a standard BCS mechanism can account for the observed superconducting transition. Theory as well as experimental results lead us to expect that a higher superconducting transition temperature might be achieved if more boron could be incorporated into the silicon [6, 41], opening up new ways to exploit superconductivity in nanostructured, mesoscopic devices. More recently, our results have been confirmed on a new set of approximately 20 samples grown under improved conditions. The superconductivity has been shown to occur at temperatures up to 0.6 K (see Fig. 4.7), a range of temperature easily accessible to ^3He pumped cryostats, instead of the more complicated dilution refrigerator.

It has been shown that highly boron-doped silicon exhibits superconducting properties, which is a very promising result for future fundamental research on the one hand and which concludes a standing quest of such a transition in silicon-based systems on the other hand. In the future, gas immersion laser doping and laser thermal processing of implanted silicon could yield silicon samples highly doped with other dopants as for instance aluminum (p-type) or phosphorous (n-type). Theoretical calculations have been performed recently and show that the critical temperature T_c could be higher than in boron-doped silicon by one order of magnitude in the case of aluminum-doped silicon [28]. Furthermore, this special type of laser processing technique could be adapted to germanium as substrate material, the group IV element for which a superconducting transition has not yet been found.

Bibliography

[1] R.A. Hein, J.W. Gibson, R. Mazelsky, R.C. Miller, and J.K. Hulm, Phys. Rev. Lett. **12**, 320 (1964).

[2] J.F. Schooley, W.R. Hosler, E. Ambler, and J.H. Becker, Phys. Rev. Lett. **14**, 305 (1965).

[3] A. Lasbley, R. Granger, and S. Rolland, Solid State Commun. **13**, 1045 (1973).

[4] M.L. Cohen, Phys. Rev. **134**, A511 (1964).

[5] D. Connétable, V. Timoshevskii, B. Masenelli, J. Beille, J. Marcus, B. Barbara, A.M. Saitta, G.-M. Rignanese, P. Mélinon, S. Yamanaka, and X. Blase, Phys. Rev. Lett. **91**, 247001 (2003).

[6] L. Boeri, J. Kortus, and O.K. Andersen, Phys. Rev. Lett. **93**, 237002 (2004).

[7] W. Buckel and J. Wittig, Phys. Lett. **17**, 187 (1965).

[8] G.N. Stepanov, T.V. Valyanskaya, and E.N. Yakovlev, Sov. Phys. Solid State **22**, 292 (1980).

[9] K.J. Chang, M.M. Dacarogna, M.L. Cohen, J.M. Mignot, G. Chouteau, and G. Martinez, Phys. Rev. Lett. **54**, 2375 (1985).

[10] E.A. Ekimov, V.A. Sidorov, E.D. Bauer, N.N. Mel'nik, N.J. Curro, J.D. Thompson, and S.M. Stishov, Nature **428**, 642 (2004).

[11] H. Kawaji, H.-O. Horie, S. Yamanaka, and M. Ishikawa, Phys. Rev. Lett. **74**, 1427 (1995).

[12] K. Tanigaki, T. Shimizu, K.M. Itoh, J. Teraoka, Y. Morimoto, and S. Yamanaka, Nat. Mater. **2**, 653 (2003).

[13] G. Kerrien, T. Sarnet, D. Débarre, J. Boulmer, M. Hernandez, C. Laviron, and M.-N. Semeria, Thin Solid Films **453**, 106 (2004).

[14] E. Bustarret, C. Marcenat, P. Achatz, J. Kacmarcik, F. Lévy, A. Huxley, L. Ortéga, E. Bourgeois, X. Blase, D. Débarre, and J. Boulmer, Nature **444**, 465 (2006).

[15] International Technology Roadmap for Semiconductors, http://public.itrs.net.

[16] B. Yu, Y. Wang, Q. Xiang, C. Riccobene, S. Talwar, and M.R. Lin, Proc. of IEDM'99, 510 (1999).

[17] K.I. Goto, T. Yamamato, M. Kose, Y. Wang, T. Lin, S. Talwar, and T. Sugii, Proc. of IEDM'99, 931 (1999).

[18] T. Noguchi, M. Kubota, H. Yamamato, K. Matsumoto, and M. Yamagishi, Tech. Rep. IEICE, ED2000-45, SDM2000-45, 7 (2000).

[19] E.C. Jones and E. Ishida, Mater. Sci. Eng. R **24**, 1 (1998).

[20] F. Foulon, A. Slaoui, and P. Siffert, Appl. Surf. Sci. **43**, 333 (1989).

[21] S.H. Jain, P.B. Griffin, J.D. Plummer, S. Mccoy, J. Gelpey, T. Selinger, and D.F. Downey, J. Appl. Phys. **96**, 7357 (2004).

[22] J. Adey, R. Jones, and P.R. Briddon, phys. stat. sol. (c) **2**, 1953 (2005).

[23] G. Kerrien, J. Boulmer, D. Débarre, D. Bouchier, A. Grouillet, and D. Lenoble, Appl. Surf. Sci. **186**, 45 (2002).

[24] G. Kerrien, M. Hernandez, C. Laviron, T. Sarnet, D. Débarre, T. Noguchi, D. Zahorski, J. Venturini, M.-N. Semeria, and J. Boulmer, Appl. Surf. Sci. **208**, 277 (2003).

[25] A. Vailionis, G. Glass, P. Desjardins, D.G. Cahill, and J.E. Greene, Phys. Rev. Lett. **82**, 4464 (1999).

[26] M. Chandrasekhar, H.R. Chandrasekhar, M. Grimsditch, and M. Cardona, Phys. Rev. B **22**, 4825 (1980).

[27] C.P. Herrero and M. Stutzmann, Phys. Rev. B **38**, 12668 (1988).

[28] E. Bourgeois and X. Blase, Appl. Phys. Lett. **90**, 142511 (2007).

[29] P.A. Lee and T.V. Ramakrishnan, Rev. Mod. Phys. **57**, 287 (1985).

[30] T. Klein, P. Achatz, J. Kacmarcik, C. Marcenat, F. Gustafsson, J. Marcus, E. Bustarret, J. Pernot, F. Omnès, Bo. E. Sernelius, C. Persson, A. Ferreira da Silva, and C. Cytermann, Phys. Rev. B **75**, 165313 (2007).

[31] M.I. Eremets, V.V. Struzhkin, H.-K. Mao, and R.J. Hemley, Science **293**, 272 (2001).

[32] M. Tinkham, AIP Conf. Proc. **58**, 1 (1980).

[33] N.R. Werthamer, E. Helfand, and P.C. Hohenberg, Phys. Rev. **147**, 295 (1966).

[34] J.H. Quateman, Phys. Rev. B **34**, 1948 (1986).

[35] A.D. Kent, A. Kapitulnik, and T.H. Geballe, Phys. Rev. B **36**, 8827 (1987).

[36] C.S. Ting, T.K. Lee, and J.J. Quinn, Phys. Rev. Lett. **34**, 870 (1975).

[37] E. Guyon, F. Meunier, and R.S. Thomson, Phys. Rev. **156**, 452 (1967).

[38] X. Blase, C. Adessi, and D. Connétable, Phys. Rev. Lett. **93**, 237004 (2004).

[39] K.W. Lee and W.E. Pickett, Phys. Rev. Lett. **93**, 237003 (2004).

[40] W.L. McMillan, Phys. Rev. **167**, 331 (1968).

[41] E. Bustarret, J. Kacmarcik, C. Marcenat, E. Gheeraert, C. Cytermann, J. Marcus, and T. Klein, Phys. Rev. Lett. **93**, 237005 (2004).

5. Metal-insulator transition in heavily aluminum-doped 4H:SiC

SiC is a promising semiconducting material for manufacturing high-power, high-temperature, and high-speed electronic devices, in particular the 4H polytype. In order to minimize on-state losses in SiC devices, highly-doped p-type layers are necessary to reduce the ohmic contact resistance of devices below $1 \times 10^{-5}\ \Omega\ cm^2$. Aluminum is the usual shallow acceptor dopant in SiC crystals and epilayers with an activation energy of about 191 meV (from photoluminescence studies [1]) or around 205 meV (from electronic transport studies [2]). Very high doping concentrations are needed in order to obtain low resistivity material. Aluminum implantation is commonly used to prepare highly doped samples, but problems related to the annealing of the crystal damage and the electrical activation of acceptor atoms in SiC still remain [3, 4]. As an alternative, Vapour-Liquid-Solid (VLS) mechanism in Al-Si melt has been shown to be an appropriate method for growing high quality epitaxial 4H-SiC layers with a high amount of aluminum [5].

5.1. Sample preparation and structural properties

The Al-doped epitaxial 4H-SiC layers were grown by a VLS mechanism in an Al-Si melt at low temperatures (1100 C) on n^+ doped Si face 4H-SiC (0001) substrate, 8° off oriented toward $[11\bar{2}0]$. The growth conditions have been described elsewhere in detail [6]. In the following, VLS93 and VLS98 are the names of the insulating and the metallic layers, respectively.

In Fig. 5.1 one can see the SIMS profile of two samples grown by the VLS mechanism with aluminum concentrations of about 3.4 to 6.4 $\times 10^{20}\ cm^{-3}$ for sample VLS93 and of about 8.7 $\times 10^{20}\ cm^{-3}$ for sample VLS98. The uniformity of doping is an indication of the high quality of the epilayers grown by the VLS mechanism, as previously reported using Raman spectroscopy and Transmission electron microscopy [5]. One should

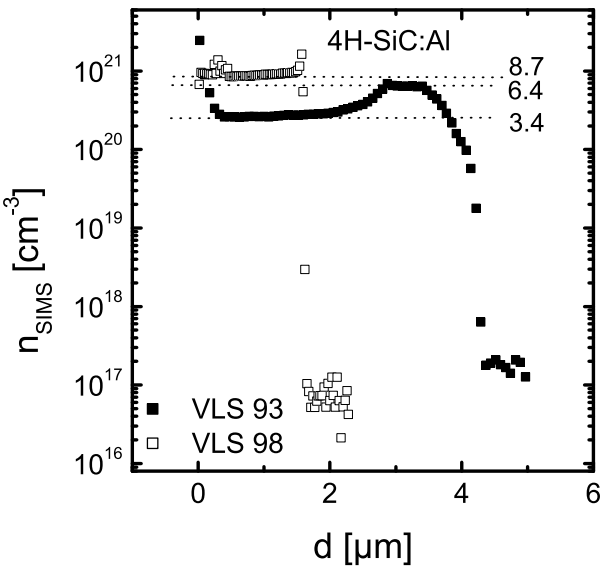

Figure 5.1.: SIMS profiles for highly aluminum-doped 4H-SiC samples VLS93 and VLS98, with aluminum concentrations of about 3.4 to 6.4 $\times 10^{20}$ cm^{-3} for sample VLS93 and of about 8.7 $\times 10^{20}$ cm^{-3} for sample VLS98.

note that such a high doping level is difficult to achieve by standard CVD or by ion implantation without any degradation of the layer quality. The onset of the SIMS profile of sample VLS93 seen in Fig. 5.1 is only an artefact of the measurement. Due to the non-uniformity of the SIMS profile of sample VLS93, the uncertainty on the resulting thickness value led us to refer to sheet resistance values in the following.

5.2. Metal-insulator transition in heavily aluminum-doped 4H:SiC

Beside the technological relevance of heavily doped SiC, the study of doping-induced insulator to metal transitions in wide band gap semiconductors is interesting in its own right. Persson et al. have studied theoretically the metal-insulator transition in p-type SiC polytypes [7]. Hereby, Mott's original model, an extended Mott-Hubbard model, and a model based on the total energy of the metallic and non-metallic phases have been used and led to values of the critical aluminum concentration in the same range, with an upper limit of 2.7×10^{20} cm^{-3} [7]. The electrical transport properties of highly doped 4H-SiC samples prepared by aluminum implantation have been reported

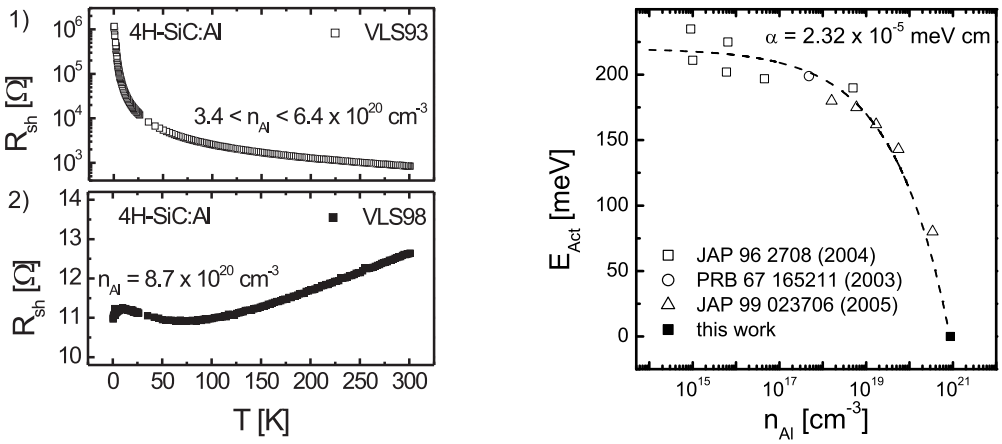

(a) (b)

Figure 5.2.: (a) (1) Temperature dependence of the sheet resistance (log. scale) for VLS93, showing a clear insulating behaviour; (2) Temperature dependence of the sheet resistance (lin. scale) of sample VLS98. A metallic behaviour $d\rho/dT < 0$ is clearly seen. The appearance of a drop in resistance at very low temperatures probably indicates the onset of a superconducting transition. Attention should be payed to the different scales of the resistance; (b) Doping dependence of the activation energy E_{Act} on the aluminum level in 4H-SiC. Experimental values of Ivanov et al. [12], Matsuura et al. [13], and Pernot et al. [2] are included. The dashed line represents the theoretical concentration dependence following $E_{Act} = E_0 - \alpha \times n_{Al}^{1/3}$ with $E_0 = 220$ meV and $\alpha = 2.32 \times 10^{-5}$ meV cm.

for samples with n_{Al} up to 2×10^{21} cm^{-3} (note that this concentration refers to the total implanted aluminum concentration, not only the activated one), but no metallic behaviour could be found (finite activation energy of the conductivity at low temperatures) [2, 8, 9, 10]. Recently, renewed interest came up for the metal-insulator transition in n-type SiC polytypes [11]. In this PhD project, we present the experimental observation of the metal-insulator transition in highly aluminum-doped 4H-SiC polytype.

The temperature dependence of the sheet resistance down to 360 mK for the two different aluminum-doped 4H-SiC samples is shown in Fig. 5.2 (a,1) and (a,2), respectively. One clearly sees that sample VLS93 is following an insulating behaviour while sample VLS98 follows a metallic behaviour $d\rho/dT < 0$. Assuming a doping efficiency of 100 %, the critical concentration of aluminum for the doping-induced metal-insulator transition lies in the range between 3.4 to 8.7 $\times 10^{20}$ cm^{-3} as determined from SIMS.

In Fig. 5.2 (b) the doping dependence of the activation energy E_{Act} of the aluminum

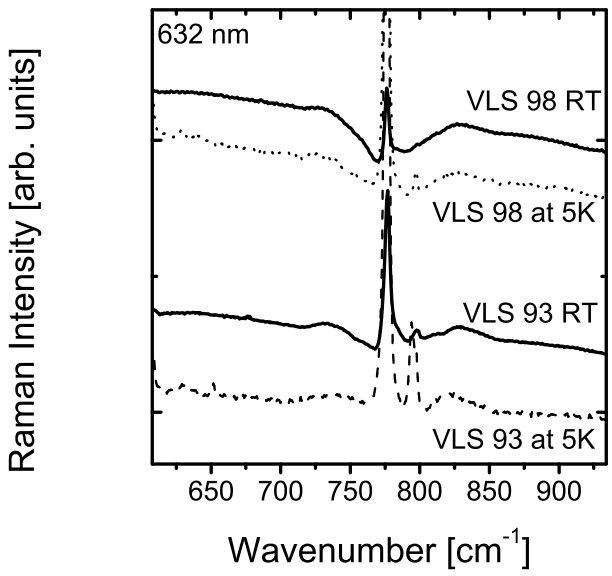

Figure 5.3.: Comparison of Raman spectra (632 nm) taken at room temperature and 4 K for two aluminum-doped samples VLS93 and VLS98. All samples show a clear Fano resonance at room temperature. Only for sample VLS98 does the Fano resonance persist down to 5 K, indicating no significant change in the carrier concentration and, therefore, suggesting metallic behaviour.

level in 4H-SiC is shown. Experimental values of Ivanov et al. [12], Matsuura et al. [13], and Pernot et al. [2] are included. The theoretical concentration dependence following $E_{Act} = E_0 - \alpha \times n_{Al}^{1/3}$ with $E_0 = 220$ meV and $\alpha = 2.32 \times 10^{-5}$ meV cm is indicated. As mentioned, Persson et al. predicted a critical value of aluminum concentration of $2.7 \times 10^{20}\ cm^{-3}$ [7], already questioned by the experimental findings of several groups [2, 8, 9, 10]. Matsuura et al. [13] and Pernot et al. [2] calculated values for α of about 1.9×10^{-5} meV cm and 1.7×10^{-5} meV cm, respectively. The upper limit of $8.7 \times 10^{20}\ cm^{-3}$ for the aluminum concentration determined in this work can be used to calculate a lower limit of $\alpha = 2.32 \times 10^{-5}$ meV cm.

As shown in Fig. 5.2 (a,1), the sample VLS93 follows an insulating behaviour. Attention should be payed to the logarithmic scale for the sheet resistance, indicating an increase of about three orders of magnitude down to low temperatures. No general fitting in terms of hopping conduction or temperature activated behaviour was possible, the conductance of sample VLS93 showing a remarkable linear temperature dependence over the whole temperature range, probably as a result of the non-uniformity of the carrier concentration as indicated by the SIMS profile in Fig. 5.1.

Fig. 5.2 (a,2) shows the temperature dependence of the sheet resistance for the aluminum-doped 4H-SiC samples VLS98, showing clear metallic behaviour $d\rho/dT < 0$. The increase in resistance at low temperatures can be explained by localization effects and electron-electron interactions typical for disordered metals (see Ref. 14 and references herein), leading to

$$\sigma_T = \sigma_0 + A \times T^{1/2} + B \times T^{p/2} \tag{5.1}$$

where p is an index depending on scattering mechanism and σ_0 the finite conductivity extrapolated to zero temperature, as was already pointed out for the case of highly boron-doped single crystal diamond samples (see Chap. 2.3, Eq. 2.29).

The appearance of a drop in resistance shown in Fig. 5.2 (a,2) at very low temperatures up to about 7 K was verified several times and may indicate the onset of a superconducting transition, probably masked by the high disorder and inhomogeneity of the sample. Indeed, superconductivity was found recently in boron-doped SiC with a critical temperature of $T_c \approx 1.4$ K [15]. A similar behaviour of the temperature dependence of the resistivity was seen in heavily boron-doped silicon [16], as well as heavily boron-doped diamond [17].

Raman spectroscopy clearly identifies the SiC polytype to be 4H-SiC [18]. Distortion and asymmetry of Raman bands occur when scattering by a discrete phonon state interferes with a broad continuum of electronic states [19]. This effect, called Fano interference or resonance, was first observed in SiC by Colwell and Klein [20]. The Fano resonance seen around the central TO phonon line at 776 cm^{-1} is a clear indication of a high free carrier concentration [18]. Fig. 5.3 shows the Raman spectra (633 nm) of the two aluminum-doped 4H-SiC samples VLS93 and VLS98 taken at room temperature and at around 5 K, respectively. One clearly sees that the Fano resonance persists in the case of the sample VLS98 down to 5 K, therefore following a clear metallic behaviour. In contrast to this, the Fano resonance seen in sample VLS93 had completely disappeared at around 5 K. This indicates a strong decrease in the number of free carriers with decreasing temperature as expected for an insulating sample.

5.3. LO-phonon-plasmon-coupled mode in 4H-SiC:Al

As already indicated, Raman spectroscopy is a powerful tool to characterize silicon carbide crystals non-destructively. It can not only be used to identify the polytype of the SiC crystal, but also to study the structural properties including e.g. stacking

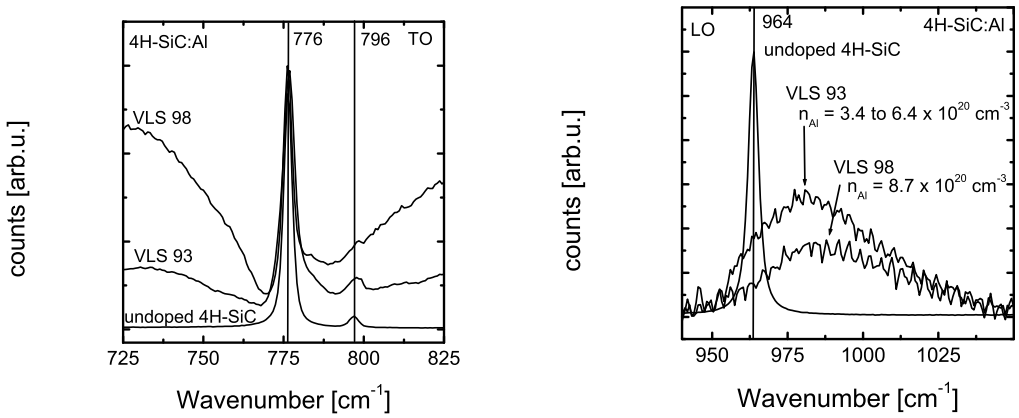

(a) (b)

Figure 5.4.: Room temperature Raman spectra of the two aluminum-doped 4H-SiC samples VLS93 and VLS98 together with a nominally undoped 4H-SiC reference, focussing on the (a) transversal optical and (b) longitudinal optical phonon modes, respectively.

disorder and stress evaluation, as well as the electronic properties giving thus information about e.g. the carrier concentration. For the latter purpose, Raman scattering from the LO-phonon-plasmon-coupled modes has been studied. This method has been applied in many III-IV semiconductors [21] as for instance GaP [22] and InP [23], as well as in ZnO [24] and ZnSe [25]. The rapid progress in growth of SiC single crystals has motivated the same study in n-type 3C-SiC [26], n-type 4H-SiC [18, 27, 28] and n-type 6H-SiC [18, 27, 28]. To our knowledge, no such study for p-type SiC polytype has shown a shift of the respective phonon mode due to the LO-phonon-plasmon-coupling [29, 30]. In our case, (temperature dependent) Raman spectroscopy has been used and reveal a clear shift of the LO phonon mode with increasing hole carrier concentration (the LO-phonon-plasmon-coupled mode).

Fig. 5.4 shows the Raman spectra (633 nm) taken at room temperature of the two aluminum-doped 4H-SiC samples VLS93 and VLS98 together with a nominally undoped 4H-SiC reference. Fig. 5.4(a) focusses on the region around the transversal optical (TO) phonon modes centered at 776 cm^{-1} (E_{2T}) and 796 cm^{-1} (E_{1T}), whereas Fig. 5.4(b) is centered around the longitudinal optical (LO) mode around 964 cm^{-1} (A_{1LO}) [31, 32, 33]. In Fig. 5.4(a), the well-observed Fano resonance is more pronounced in sample VLS98, in agreement with the much higher carrier concentration in this metallic sample. Furthermore, no discernible change in the peak intensity and position as well as the FWHM for the TO mode at 776 cm^{-1} can be seen, clearly

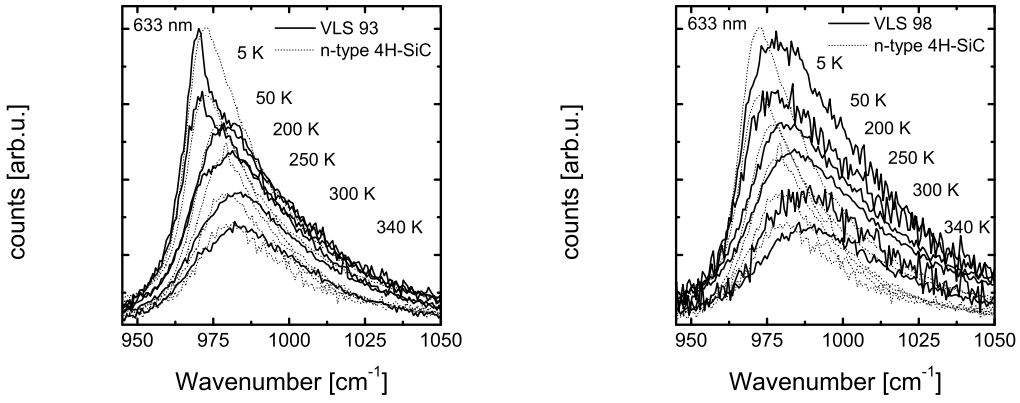

(a) (b)

Figure 5.5.: Temperature dependence of the LO-phonon-plasmon-coupled mode for sample (a) VLS93 and (b) VLS98, respectively, compared to the spectra taken for a typical substrate used for the growth of both samples.

indicating the stress-free nature of the samples [34]. In Fig. 5.4(b), the A_{1LO} mode located at 964 cm^{-1} in the undoped 4H-SiC reference sample is broadened and shifted to higher frequencies in the two highly-doped samples VLS93 and VLS98 with aluminum concentrations of 3.4 to 6.4 $\times 10^{20}$ cm^{-3} and 8.7 $\times 10^{20}$ cm^{-3}, respectively. A very strong shift of about 24 cm^{-1} in sample VLS98 and of about 19 cm^{-1} in sample VLS93 is seen. The broadening and shift of these peak profiles are typical features of LO-phonon-plasmon coupling.

As already mentioned, similar results on the LO-phonon-plasmon-coupled modes have been observed for the n-type 4H-SiC polytype [18, 27, 28]. This group studied the dependence of the peak position for carrier concentrations up to 5×10^{18} cm^{-3}, with shifts up to 16 cm^{-1}. The n-type substrates used for the growth of the aluminum-doped 4H-SiC layers VLS93 and VLS98 have carrier concentrations of about 5×10^{18} cm^{-3} and, thus, care has to be taken in the analysis of the peak position of the LO-phonon-plasmon-coupled modes.

Fig. 5.5(a) and Fig. 5.5(b) show the temperature dependence of the LO-phonon-plasmon-coupled mode for sample VLS93 and VLS98, respectively, compared to the spectra taken for a typical substrate used for the growth of both samples. At high temperature, a clear difference between the contribution from the substrate and from the sample is seen for both samples VLS93 and VLS98. This difference is maintained in sample VLS98 even at low temperatures, whereas it is difficult to differentiate between the contribution from the substrate and the layer for sample VLS93 at low

temperatures. This can be clearly seen in Fig. 5.6(a), showing the peak position of the LO-phonon-plasmon-coupled mode for sample VLS93 and VLS98 as well as the substrate reference sample. A more detailed lineshape analysis of the Raman spectra is necessary taking into account the two-layer structure of our samples, in order to obtain quantitative information about the real peak position.

The dielectric function $\epsilon(\omega)$ is considered to be given by the contributions from the phonons and plasmons, and can be written as

$$\epsilon(\omega) = \epsilon_\infty \left\{ 1 + \frac{\omega_{LO}^2 - \omega_{TO}^2}{\omega_{TO}^2 - \omega^2 - i\omega\Gamma} - \frac{\omega_p^2}{\omega\left(\omega + i\gamma\right)} \right\} \tag{5.2}$$

where ω_{LO}, ω_{TO} are the frequencies of the A_{1LO} and A_{1TO} modes, respectively, Γ the phonon damping constant and γ the plasma damping constant. The plasma frequency ω_p is given by

$$\omega_p^2 = \frac{4\pi n e^2}{\epsilon_\infty m^*} \tag{5.3}$$

with n the carrier concentration and m^* the effective mass. Note that from the Raman spectra (due to the backscattering geometry) of the axial mode A_{1LO} we could only obtain information about the longitudinal effective mass along the same c-axis (or ML in the Brillouin zone). Neglecting both damping terms in Eq. 5.2, the (two) LPP (LO-phonon-plasmon) frequencies are roots of the equation $\epsilon(\omega) = 0$, following

$$\omega_{LPP,\,\pm}^2 = \frac{1}{2}\left\{ \omega_{LO}^2 + \omega_{TO}^2 \pm \left[\left(\omega_{LO}^2 + \omega_{TO}^2\right)^2 - 4\omega_p^2\omega_T^2 \right]^{1/2} \right\} \tag{5.4}$$

This gives the usual non-linear behaviour displayed schematically in Fig. 5.6(b). It is important to note that this picture is only valid taking the phonon and plasmon damping constant (Γ and γ, respectively) negligible small, corresponding to a perfect crystal with infinite lifetime for carriers and phonons. Moreover, the plasmon damping constant is inversely proportional to the carrier mobility. Therefore, a good agreement of experimental data with this simplified model was found in the case of highly conductive GaN bulk crystals [35]. Perlin et. al have been able to identify the two branches $LPP+$ and $LPP-$ for samples with very high carrier concentrations and mobilities [35]. The same approach can not be made for the n- and p-type 4H-SiC samples. The crossing point of the plasmon frequency and the LO-phonon frequency would yield much too high carrier concentration using Eq. 5.3 (only unrealistic values of the effective mass $m^* \approx 15m_0$ would correspond to the experimental situation). Therefore, a slight plasmon overdamping had to be introduced in order to fit the data correctly

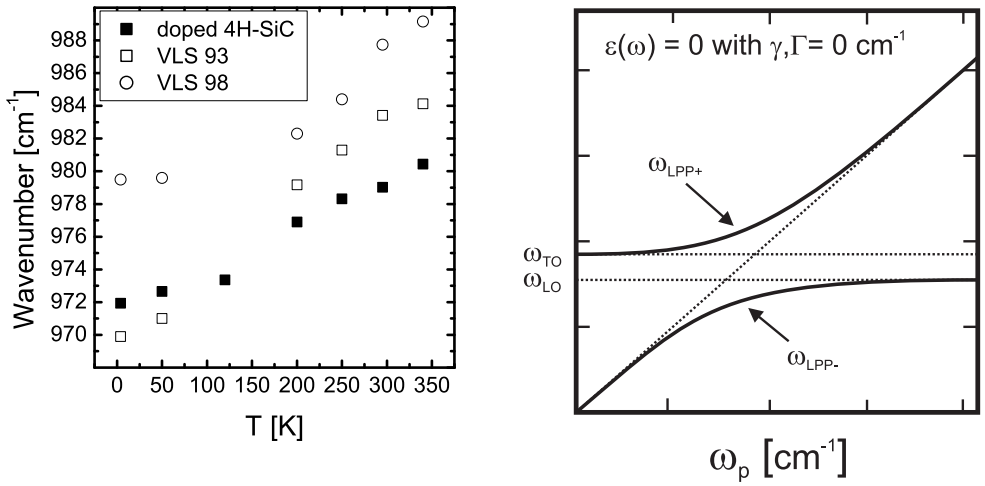

(a) (b)

Figure 5.6.: (a) Peak position of the LO-phonon-plasmon-coupled mode for sample VLS93 and VLS98 as well as the substrate reference sample; (b) Roots of Eq. 5.4 for $\epsilon(\omega) = 0$, in the case of negligible phonon and plasmon damping.

in the case of n-type 4H-SiC samples with carrier concentrations in the range 10^{16} to 10^{18} cm^{-3} [18, 27, 28]. As already mentioned, in p-type 4H-SiC a similar fitting of the LO-phonon-plasmon-coupled modes as a function of the carrier concentration has not yet been performed. Previous studies on samples with carrier concentrations up to 1×10^{20} cm^{-3} showed no shift of the LO-phonon mode, thus suggesting a very weak phonon-plasmon coupling [29, 30]. However, our experimental data show a clear shift in frequency which is attributed to the LO-phonon-plasmon-coupled mode $LPP+$. The corresponding lower branch $LPP-$ (shown schematically in Fig. 5.6(b)) would appear at wavenumbers too close to the Rayleigh scattered light in our experiments and, thus, could not be observed simultaneously. As already mentioned, in the case of n-type 4H-SiC a lineshape analysis introducing the plasmon frequency ω_p and the phonon and plasmon damping constants Γ and γ, respectively, as adjustable parameters, reproduced very well the experimental data [18, 27, 28].

Fig. 5.7(a) and Fig. 5.7(b) show schematically the influence of both the plasmon and phonon damping constant γ and Γ, respectively, on the lineshape of the LO-phonon-plasmon-coupled mode following the usual fitting procedure [18, 26, 27, 28]. As seen in Fig. 5.7(a), a small plasmon damping constant $\gamma = 0.5 \times \omega_p$ (with respect to the plasmon frequency ω_p) yields a symmetric lineshape centered close to the plasmon frequency ω_p as it was depicted in Fig. 5.6(b) valid for negligible damping. Overdamping (as for n-type 4H-SiC [28]) results in a strong shift to lower frequencies

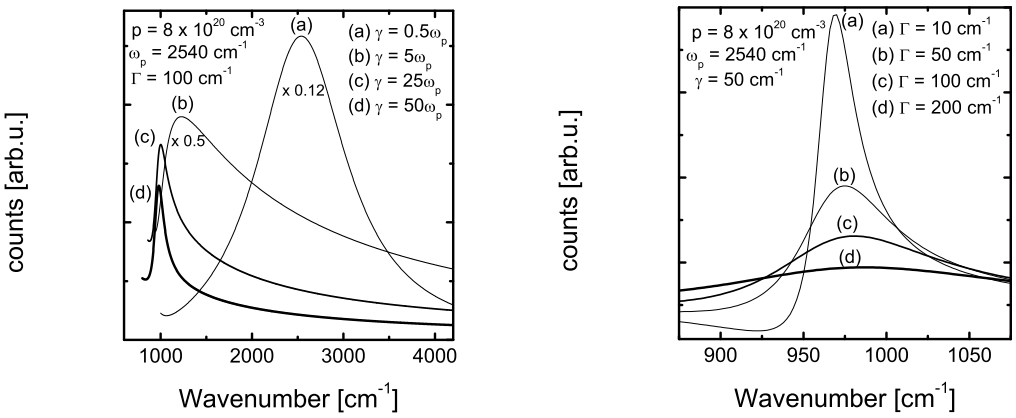

(a) (b)

Figure 5.7.: Influence of both the plasmon and phonon damping constant (a) γ and (b) Γ, respectively, on the lineshape of the LO-phonon-plasmon-coupled mode following the usual fitting procedure [18, 26, 27, 28].

and to a more asymmetric lineshape, similar to the lineshapes obtained at low temperatures for the 4H-SiC substrate (n-type) and the aluminum-doped sample VLS93 shown in Fig. 5.5(a). Keeping the plasmon damping parameter constant, an increase in the phonon damping constant shown in Fig. 5.7(b) does not shift significantly the center frequency, but results in a more symmetric lineshape, as was observed for both aluminum-doped samples VLS93 and VLS98 (see Fig. 5.5). However, a detailed analysis of the lineshape is necessary taking into account the layered structure in order to seperate the contribution to the signal from the n-type 4H-SiC substrate and the highly aluminum-doped layer, respectively. Unfortunately we were not able to perform Hall effect measurements on both layers, probably due to the layered structure. Müller et al. [30] were not able to detect a discernible shift in the LO-phonon frequency due to the coupling to the plasmon, but correlated the Hall carrier concentration p_{Hall} to the linewidth $FWHM_{LPP+}$ of the LO-phonon-plasmon-coupled mode for carrier concentrations in the lower-doped range 3×10^{16} to 2×10^{19} cm^{-3}, following an analytical expression $p_{Hall} = 2.63 \times 10^{14} \times (FWHM_{LPP+})^{4.03}$. Neglecting the contribution of the substrate (valid at higher temperatures), the linewidth $FWHM_{LPP+}$ for both samples VLS93 and VLS98 estimated at room temperature, are approximately 25 cm^{-1} and 40 cm^{-1}, respectively. This would correspond to carrier concentrations of about 1.1×10^{20} cm^{-3} and 7.5×10^{20} cm^{-3} for samples VLS93 and VLS98, respectively, in good agreement with the aluminum concentration determined from secondary ion

mass spectroscopy (3.4 to 6.4 $\times 10^{20}$ cm^{-3} and 8.7 $\times 10^{20}$ cm^{-3}). The underestimate is probably due to the underestimate of the linewidth resulting from neglecting the contribution from the substrate and/or due to the partial ionisation of acceptors for sample VLS93.

The doping-induced metal-insulator transition has been observed in highly aluminum-doped 4H-SiC via electronic transport measurements and temperature dependent Raman spectroscopy. The possible onset of a superconducting transition at low temperature for the metallic sample motivates a more detailed study of such highly aluminum-doped samples. Furthermore, we presented the first experimental evidence of a shift of the LO-phonon-plasmon-coupled mode $LPP+$ in p-type 4H-SiC with respect to the LO-phonon frequency of the undoped material. In various other materials, this shift has been studied extensively in order to obtain information on the electronic properties, for instance effective mass, carrier concentration, and mobility. A similar approach motivates new measurements of the Hall effect in our double layer system in order to extract more information from the temperature dependent Raman spectroscopy measurements. A complementary study of the far infrared absorption could give information on the free carrier concentration via the plasma edge.

Bibliography

[1] M. Ikeda, H. Matsunami, and T. Tanaka, Phys. Rev. B **22**, 2842 (1980).

[2] J. Pernot, S. Contreras, and J. Camassel, J. Appl. Phys. **98**, 023706 (2005).

[3] V. Heera, K.N. Madhusoodanan, A. Mücklich, D. Pankin, and W.Skopura, Appl. Phys. Lett. **81**, 70 (2002).

[4] Y. Negoro, T. Kimoto, H. Matsunami, F. Schmid, and G. Pensl, J. Appl. Phys. **96**, 4916 (2004).

[5] C. Jacquier, G. Ferro, C. Balloud, M. Zielinski, J. Camassel, E. Polychroniadis, J. Stoemenos, F. Cauwet, and Y. Monteil, Mat. Sci. Forum **457-460**, 735 (2004).

[6] G. Ferro and C. Jacquier, New Jour. Chem. **28**, 889 (2004).

[7] C. Persson, A. Ferreira da Silva, and B. Johansson, Phys. Rev. B **63**, 205119 (2001).

[8] T. Troffer, M. Schadt, T. Frank, H. Itoh, G. Pensl, J. Heindl, H.P. Strunk, and M. Maier, phys. stat. sol (a) **162**, 277 (1997).

[9] J.M. Bluet, J. Pernot, J. Camassel, S. Contreras, J.L. Robert, J.F. Michaud, and T. Billon , J. Appl. Phys. **88**, 1971 (2000).

[10] V. Heera, K.N. Madhusoodanan, W. Skorupa, C. Dubois, and H. Romanus, J. Appl. Phys. **99**, 123716 (2006).

[11] A. Ferreira da Silva, J. Pernot, S. Contreras, B.E. Sernelius, C. Persson, and J. Camassel, Phys. Rev. B **74**, 245201 (2006).

[12] I.G. Ivanov, B. Magnusson, and E. Janzén, Phys. Rev. B **67**, 165211 (2003).

[13] H. Matsuura, M. Komeda, S. Kagamihara, H. Iwata, R. Ishihara, T. Hatakeyama, T. Watanabe, K. Kojima, T. Shinohe, and K. Arai, J. Appl. Phys. **96**, 2708 (2004).

[14] P.A. Lee and T.V. Ramakrishnan, Rev. Mod. Phys. **57**, 287 (1985).

[15] Z. Ren, J. Kato, T. Muranaka, J. Akimitsu, M. Kriener, and Y. Maeno, J. Phys. Soc. Jpn. **76**, 103710 (2007).

[16] E. Bustarret, C. Marcenat, P. Achatz, J. Kacmarcik, F. Lévy, A. Huxley, L. Ortéga, E. Bourgeois, X. Blase, D. Débarre, and J. Boulmer, Nature **444**, 465 (2006).

[17] T. Klein, P. Achatz, J. Kacmarcik, C. Marcenat, F. Gustafsson, J. Marcus, E. Bustarret, J. Pernot, F. Omnès, Bo. E. Sernelius, C. Persson, A. Ferreira da Silva, and C. Cytermann, Phys. Rev. B **75**, 165313 (2007).

[18] S. Nakashima and H. Harima, phys. stat. sol (a) **162**, 39 (1997).

[19] U. Fano, Phys. Rev. **124**, 1866 (1961).

[20] P.J. Colwell and M.V. Klein, Phys. Rev. B **6**, 498 (1972).

[21] M.V. Klein, *Light scattering in solids* (Springer-Verlag, Berlin, 1975).

[22] G. Irmer, W. Siegel, G. Kühnel, J. Monecke, F.M.M. Yauoka, B.H. Bairamov, and V.V. Toprov, Semicond. Sci. Technol. **6**, 1072 (1991).

[23] L. Artús, R. Cuscó, J. Ibánez, N. Blanco, and G. González-Díaz, Phys. Rev. B **60**, 5456 (1999).

[24] B.H. Bairamov, A. Heinrich, G. Irmer, V.V. Toporov, and E. Ziegler, phys. stat. solidi b **119**, 227 (1983).

[25] Yugami, S. Nakashima, K. Sakai, H. Kojima, M. Hangyo, and A. Mitsuishi, J. Phys. Sot. Jpn. **56**, 1881 (1987).

[26] H. Yugami, S. Nakashima, and A. Mitsuishi, J. Appl. Phys. **61**, 354 (1987).

[27] H. Harima, S. Nakashima, and T. Uemura, J. Appl. Phys. **78**, 1996 (1995).

[28] S. Nakashima and H. Harima, J. Appl. Phys. **95**, 3541 (2004).

[29] H. Harima, T. Hosoda, and S. Nakashima, Mat. Sci. Forum **338**, 607 (2000).

[30] R. Müller, U. Künecke, A. Thuaire, M. Mermoux, M. Pons, and P. Wellmann, phys. stat. solidi c **3**, 558 (2006).

[31] D.W. Feldman, J.H. Parker, W.J. Choyke, and L. Patrick, Phys. Rev. **170**, 698 (1968).

[32] D.W. Feldman, J.H. Parker, W.J. Choyke, and L. Patrick, Phys. Rev. **173**, 787 (1968).

[33] P.J. Colwell and M.V. Klein, Phys. Rev. B **6**, 498 (1972).

[34] G. Martinez, *Optical properties of solids* (North-Holland, Amsterdam, 1980).

[35] P. Perlin, J. Camassel, W. Knap, T. Taliercio, J.C. Chervin, T. Suski, I. Grzegory, and S. Porowski, Appl. Phys. Lett. **67**, 2524 (1995).

6. Outlook

The first part of this PhD project reports on the metal-insulator transition and its impact on the superconductivity in highly boron-doped single crystal diamond. The main idea behind the isotopic substitution for this material was the examination of the isotope effect which turned out to be a difficult task, hopefully made easier by our results. However, the identification of the low wavenumber phonon mode with the vibrational mode related to boron dimers was proposed on the basis of this substitution. The effect of the (high) boron incorporation on the structural properties has been studied. The electronic band structure of diamond has been discussed and the relevance of strain for electronic properties has been pointed out.

In addition, work done during this PhD project contributed to several other studies related to aspects of superconductivity in single crystal diamond. Low temperature scanning tunneling spectroscopy measurements on a more recently grown sample confirmed the BCS compatibility (via the temperature dependancy of the superconducting gap), and also the better quality of the sample, which is also under study by transmission electron microscopy (TEM, U. Cádiz). A more detailed study of the until now not well understood magnetic field-induced resonances observed in the BCS gap is underway. Based on an already performed study of the phonon softening for superconducting diamond samples by Hösch et al. (PRB 75, 140508R (2007)), a more detailed study of this softening and its dependence across the metal-insulator transition was motivated by inelastic X-ray scattering (IXS) measurements performed at the ESRF, Grenoble, France, by M. Hösch, together with our second order Raman spectroscopy measurements. Furthermore, a study of the electronic band structure via angular resolved photo emission spectroscopy (ARPES) is planned in the near future, in order to confirm the results obtained by Yokoya et al. (Nature 438, 647 (2005)), and extend their study to probe other directions in the Brillouin zone.

The superconductivity of highly boron-doped diamond samples could further be used to fabricate new devices as for example SQUIDs due to the high critical magnetic fields. Together with the high stiffness of diamond, the fabrication of nanomechanical structures from this material are of high interest for fundamental research.

With suspended diamond nanostructures one could reach GHz vibration frequencies comparable with thermal energies at milliKelvin temperatures. Highly boron-doped nanocrystalline diamond films grown on a standard silicon wafer (with intermediate SiO_2 layer) are hereby of particular interest due to the easy adaption of lithographic lift-off techniques.

As already mentioned, granularity plays an important role in highly boron-doped nanocrystalline diamond. The grain size is about 200 nm, in the reach of standard processing techniques. Etching on a 150 nm scale would result in a linear chain of superconducting granules, an innovative method to mimic a one-dimensional chain of Josephson junctions.

In the case of highly boron-doped single crystal silicon, the reproducibility and amelioration of the superconducting properties are the first step towards new superconduting devices based on this material. One could hereby benefit from the already existing highly advanced processing tools for silicon. From the fundamental point of view, the dependence of the superconducting transition temperature on the dopant concentration, as well as the study of the origin of the superconductivity via isotopic substitution or via scanning tunneling spectroscopy (study is underway), remain open questions.

Only recently, highly boron-doped 3C-SiC has been found superconducting by Ren et al. (JPSJ 76, 103710 (2007). Further investigation of the possible occurence of superconductivity in highly aluminum-doped 4H-SiC is thus highly motivated. Even from a more general point of view, in the case of highly-doped column IV elements or compounds, there are still many other systems open for the study of superconductivity, for example highly-doped germanium-based samples as well as n-type silicon and diamond (even if much progress has been made, note that highly-doped n-type diamond samples are not yet available).

A. Experimental techniques

A.1. Secondary Ion Mass Spectroscopy (SIMS)

Secondary ion mass spectroscopy is a powerful technique for the analysis of impurities in solids. The technique relies on removal of material from a solid by sputtering and on analysis of the sputtered ionized species. A primary ion beam impinges on the sample and (ionized) atoms from the sample are ejected from the sample in case they receive enough energy from the incident ions. These ions are further analyzed with a mass spectrometer. It allows simultaneous detection of different elements with resolution limits (depending on the element and the background signal) as low as 10^{14} to 10^{15} cm^{-3}. Unfortunately it is a destructive characterization method since removing material by sputtering leaves a crater in the sample. Profilometric measurements of the crater depth are used for calibration of the thickness. The secondary ion signal of a given element is monitored as a function of time giving access to the dopant density profile on a scale of several microns, with a depth resolution of 1 to 5 nm. The impurity density is obtained by comparison with the secondary ion signal of a reference sample with a well-known dopant profile. One should note that secondary ion mass spectroscopy determines the total, and not the electrically active impurity density. No information about the actual configuration of the impurity atoms in the host lattice is obtained.

In the case of highly boron-doped single crystal diamond, all measurements have been performed by F. Jomard at the GEMaC (Groupe d'Etude de la Matière Condensée) at the CNRS and Université de Versailles Saint Quentin (UVSQ). A commercially available CAMECA IMS 4f instrument was used and a diamond reference implanted with 2×10^{15} cm^{-2} was measured in the same runs for calibration. An incident beam of Cs^+ ions with an energy of 10 keV was used, the extraction bias being 4.5 kV.

The boron density profiles of several samples (PA in {001} growth direction in the configuration $^{12}C^{11}B$) are shown in Fig. A.1(a). Hereby the total amount of boron is presented, based on the assumption of a natural abundance of 19 % for ^{10}B.

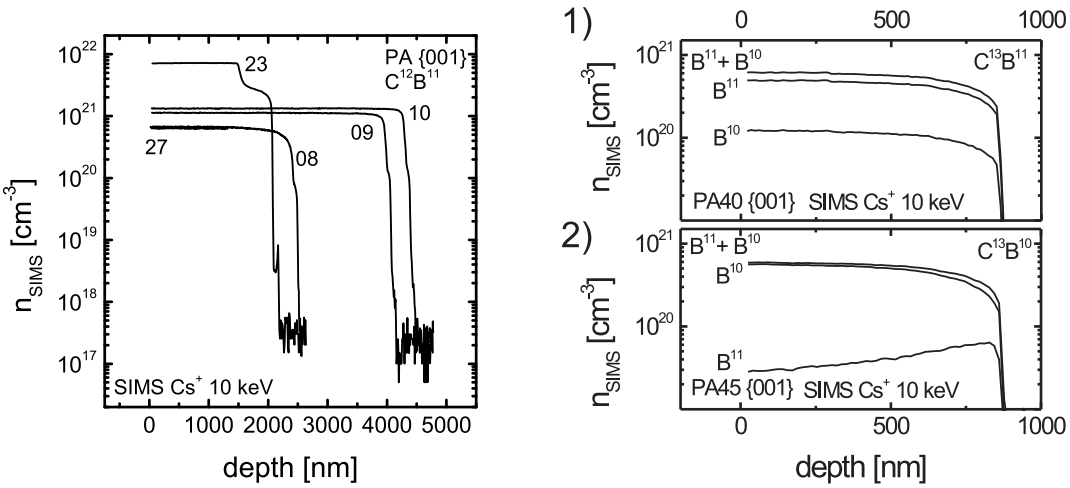

(a) (b)

Figure A.1.: (a) Several depth profiles of the boron concentration as measured by SIMS for several recently grown samples PA; (b) Typical SIMS depth profile for each of both series of isotopically substituted samples: (1) The data for samples grown with ^{11}B containing diborane B_2H_6 clearly reflect the already mentioned natural abundance of 19 % for ^{10}B, whereas (2) samples grown with the isotopically marked diborane $^{10}B_2H_6$ only contain small amounts of the isotope ^{11}B.

For samples grown with boron concentrations in the gas phase up to B/C = 2000 ppm, uniform profiles are obtained (on a log-scale). Presented on a linear scale, deviations in the 10 % range determine the total error bar. The little shoulder seen as the signal decreases (at the interface epilayer/substrate) reveals the high boron concentrations in the approximately 50 nm thick buffer layer due to the memory effect of the growth chamber. The SIMS data shown in Fig. A.1(b) (1) and (2) show two typical, isotopically resolved density profiles for the other two possible configurations $^{13}C^{11}B$ and $^{13}C^{10}B$ studied in this work. The data for samples grown with ^{11}B containing diborane B_2H_6 clearly reflect the already mentioned natural abundance of 19 % for ^{10}B, whereas samples grown with the isotopically marked diborane $^{10}B_2H_6$ only contain small amounts of the isotope ^{11}B.

The highly boron-doped nanocrystalline diamond samples have been analysed by the Centre of Surface and Materials Analysis (CSMA Ltd.) in England, also using a Cameca IMS 4f secondary ion mass spectrometer. The primary beam consists of O_2^+ ions with a nominal impact energy of about 8 keV (incident angle 30°). The calibration was performed using a ^{11}B ion implanted diamond-like carbon standard

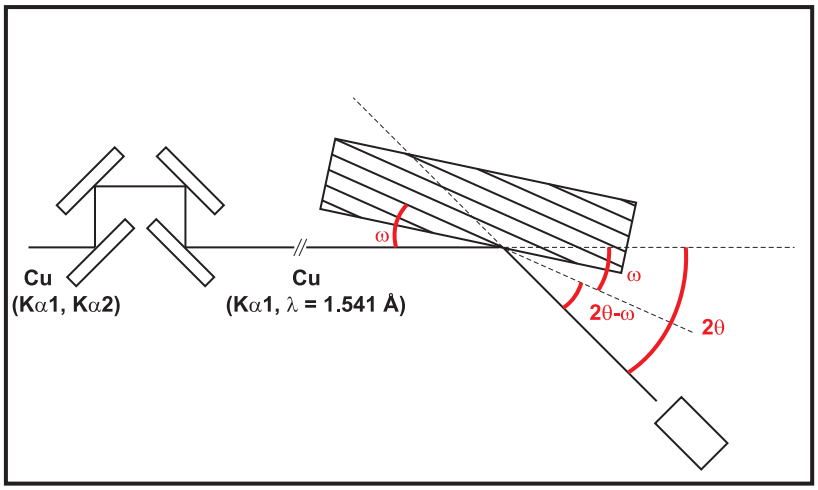

Figure A.2.: Schematic description of the setup used for the high resolution X-ray diffraction measurements.

with 5×10^{14} cm^{-2}.

A.2. High resolution X-ray diffraction

The X-ray diffraction (XRD) data were collected around symmetrical Bragg reflections, {004}- and {111}-direction according to the orientation of the substrate. In the case of highly boron-doped diamond as well as silicon, in-plane lattice matching leads to either an expansion or contraction of the lattice parameter a in the growth direction. Therefore, a XRD signal is detected under different angles for the substrate and the epilayer, corresponding to the different lattice spacings due to the difference in size of the constituent atoms. In the case of boron-doped diamond, the higher Bohr radius of boron with respect to carbon leads to a lattice expansion in the growth direction and hence a peak in XRD is seen at smaller diffraction angles as the substrate. For boron-doped silicon, the inverse situation occurs. The Bohr radius of boron is smaller compared to the one of silicon, a peak in XRD is detected at higher diffraction angles corresponding to a contraction of the lattice in growth direction. In order to get further information on the mosaicity and the strain distribution in the epilayer, reciprocal space mapping (rsm) around symmetrical and also on asymmetrical Bragg reflections have been performed. The out of plane mapping ({311}-direction) experimentally proves the biaxially strained nature of our boron-doped epilayers.

High-resolution XRD measurements were performed with a commercial Philips Materials research diffractometer which is shown schematically in Fig. A.2. The triple

axis diffractometer is using as a source the $CuK_{\alpha 1}$ line with a wavelength $\lambda = 0.15406$ nm, selected through a (220) Ge four-reflection channel cut monochromator. The angular resolution was better than 3×10^{-3} degrees. The rocking curves consist in fact of a $(2\Theta - \omega)$-scan, by measuring the diffracted intensity as a function of the rotation, ω, of the sample, with a continuous change of 2ω for the detector. This resembles the normally used rocking curves where only the sample is rotated due to the fact that our detector opening is not wide enough in order to detect the total signal. In the case of reciprocal space mapping, another analyzer was located in front of the detector to increase selectivity. A series of $(2\Theta - \omega)$-scans is performed for a range of ω values about the specific X-ray reflection.

A.3. Raman spectroscopy

Raman spectroscopy is based on the Raman effect first reported by Raman in 1928, based on the inelastic interaction of the incident light with the vibrational modes of the material probed. The scattered light from the sample is found to contain mainly wavelengths that were incident on the sample (so-called Rayleigh scattering) but also at different wavelengths at much lower intensities. The interaction of light with optical phonons is called Raman scattering, whereas the interaction with acoustic phonons results in Brillouin scattering. Raman spectroscopy is only practical when an intense monochromatic light source like a laser is used. One distinguishes between Stokes-shifted and Anti-Stokes-shifted scattering depending on wether a phonon is emitted to the lattice or absorbed from the lattice. The latter is much weaker in signal, and it is the Stokes-mode which is usually measured. One should note that Raman spectroscopy is a non-destructive and, thus, very powerful characterization tool.

Raman spectroscopy measurements have been performed using a single monochromator Jobin-Yvon Labram Infinity model, operating at either 633 nm in the visible (internal HeNe laser source) or 325 nm in the UV (external HeCd laser source). An optical microscope is used to focus the laser on the sample surface, the micro-Raman spectra are obtained in a backscattering geometry under confocal conditions. Measurements done at room temperature are realized using a $\times 100$ objective in the visible (1800 cm^{-1} grating, notch filter) and a $\times 40$ objective in the UV (2400 cm^{-1} grating, edge filter). For the low temperature measurements down to 5 K, a He flow cryostat was used and measurements were restricted to a long working distance $\times 50$ objective in the visible. It was not possible to perform UV-Raman measurements at low tem-

peratures due to the opacity of the optical window of the cryostat. A liquid nitrogen cooled charged-coupled device (CCD) was used for signal collection.

A.4. Electronic transport, Hall effect, and a.c. susceptibility measurements

The temperature dependence of the resistivity has been obtained using a standard four terminal configuration, with current injection on the outer leads and voltage measurement on the inner leads. There exist following relationship between the resistivity ρ and the measured resistance R as

$$R = \rho\frac{L}{A} = \rho\frac{L}{wd} = \frac{\rho}{d}\frac{L}{w} \tag{A.1}$$

where $\frac{\rho}{d}$ is also known as the so-called sheet resistance R_{sh}. w is the width of the contacts, whereas L is the distance between the voltage leads.

Hall effect measurements have been performed in the van der Pauw contact configuration, a comparison with van der Pauw measurements of the resistivity enabled us to determine the carrier concentration as well as the mobility. The Hall effect was discovered by Hall in 1879. Hall studied the nature of the force acting on a conductor carrying a current in a magnetic field. As schematically shown in Fig. A.3(a), the charge carriers in the conductor become deflected by the magnetic field and give rise to an electric field (Hall voltage) that is perpendicular to both the current and magnetic field.

In the y-direction there is no net current, therefore

$$J_y = J_h + J_e = epv_{hy} + envey = 0, \Rightarrow pv_{hy} = -nv_{ey} \tag{A.2}$$

with v_{hy} and v_{ey} the drift velocities in y-direction and p and n the carrier concentration for holes and electrons, respectively. The net force experienced by the carriers, as shown in Fig. A.3(a), is

$$F_{hy} = \frac{ev_{hy}}{\mu_h} = eE_y - ev_{hy}B_z \tag{A.3}$$

for holes (h) and

$$F_{ey} = \frac{ev_{ey}}{\mu_e} = eE_y + ev_{ey}B_z \tag{A.4}$$

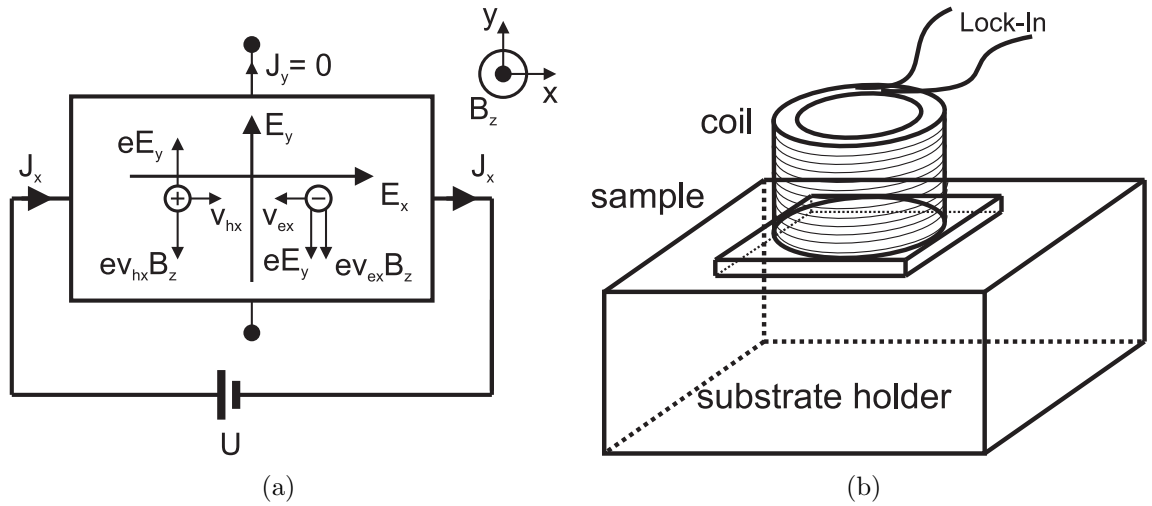

Figure A.3.: (a) Schematic description of the principle of the Hall effect; (b) Schematic description of the setup used for a.c. susceptibility measurements.

for electrons (e). Substituting $v_{hx} = \mu_h E_x$ and $v_{ex} = \mu_e E_x$, one gets together with Eq. A.2 the expression

$$E_y(p\mu_h + n\mu_e) = B_z E_x(p\mu_h^2 - n\mu_e^2) \tag{A.5}$$

The total current density is finite and is given by the usual expression

$$J_x = epv_{hx} + env_{ex} = (p\mu_h + n\mu_e)eE_x \tag{A.6}$$

and using substituting Eq. A.6 for E_x in Eq. A.5 one obtains for the Hall coefficient, by definition,

$$R_H = \frac{E_y}{J_x B_z} = \frac{p\mu_h^2 - n\mu_e^2}{e(p\mu_h + n\mu_e)^2} = \frac{p - nb^2}{e(p + nb)^2} \tag{A.7}$$

with $b = \mu_e/\mu_h$. In the case $p \gg n$ one finds the well-known result $R_H = 1/qp$.

As already mentioned, zero resistivity alone is no indication for the occurence a superconducting transition in the bulk material. Superconducting filamentary paths across the sample could shortcircuit the rest of the sample, yielding zero resistance. Filamentary superconductivity is rather sensitive to the currents applied to the sample. The fact that the superconducting resistive transition is quite stable over a relatively large range of applied currents (10 nA up to 10 μA) is an indication for a transition in the bulk. However, only complementary measurements of for instance the magnetization or the specific heat can give insight about the bulk nature of the superconducting

transition. Unfortunately, all attempts measuring the specific heat anomaly typical for a superconducting transition (and reported by Ekimov et. al) remained unsuccessful. Laser cutting of the thickest possible epilayer deteriorated the material due to graphitization. More easily accessible is the Meissner effect seen in superconductors, the expulsion of a magnetic field due to the perfect diamagnetism (provoked by induced dissipationless currents) of the superconductor. The magnetic susceptibility χ for a superconductor can therefore be written as

$$\chi = \frac{dM}{dH} = -1 \tag{A.8}$$

where M is the magnetization and H the magnetic field. The magnetic induction B equals zero in the superconductor, and the relation $B = \mu_0(H + M)$ leads to Eq. A.8. The superconducting transition corresponds to a change in the susceptibility from $\chi = 0$ in the normal state to $\chi = -1$ in the superconducting state.

Measurements of the a.c. susceptibility were obtained by recording the change in the self inductance of a small coil using standard Lock-In amplification. The mounting of the sample is shown schematically in Fig. A.3(b), the sample is glued to the (thermalizing) sample holder and the superconducting epilayer covers the whole surface of the coil. An a.c. current $i = i_0 sin(\omega t)$ applied to the coil results in an a.c. magnetic field $h = h_0 sin(\omega t)$. The real and imaginary part of the impedance is measured with the Lock-In, which can be written as

$$Z(\omega) = R + j\omega L \tag{A.9}$$

with L the inductance of the coil and R the resistance. The magnetic flux Φ through the coil is directly related to the inductance L via $\Phi = LI$ with I the total current. Assuming the ideal case of an infinite coil, and that the whole surface of the coil is covered by the (superconducting) sample, $\Phi = BS$ with S the total covered surface, using $BS = Li_0$ one obtains

$$L\omega = \frac{\mu_0(1 + \chi)HS\omega}{i_0} \tag{A.10}$$

To detect the superconducting transition it is sufficient to measure the change in the self inductance.

Acknowledgements

At this point I want to express my thanks to all the people who helped during the work on my PhD project. These are in particular

Etienne Bustarret, who made the link between the TUM/WSI and the CEA Grenoble via his wide band gap semiconductor group, and gave me the possibility to work on this interesting and nice topic. He guided and encouraged me throughout this work, and his codirection was a big source of motivation. He made this difficult task possible and manageable.

Martin Stutzmann, who guided me in the choice of my PhD project and accepted the codirection of this thesis at the TU München. My stays at the WSI during this work always led to very fruitful discussions, opening up my mind from a professional as well as personal point of view.

Christophe Marcenat, who accepted the direction of this PhD project at the CEA Grenoble. His great expertise for all the delicate low temperature measurements was indispensable for the success of this thesis.

Jerôme Lesueur and **Christoph Nebel**, who accepted to render an expert opinion for this PhD thesis, and **Etienne Gheeraert**, who also took part of the examining jury.

Jean-Pascal Brison, chef de service du SPSMS, as well as **Bernard Salce** and **Marc Sanquer**, chefs du LCP and LaTEQS, who gave me the possibility to work in their group at the CEA Grenoble where I gained a lot of and in experience.

The chefs de l'équipe semi-conducteurs à large bande interdite: **Etienne Bustarret**, **Pierre Muret**, and **Etienne Gheeraert**. It was a pleasure to join this group.

All the members of my groups in the CEA and CNRS Grenoble, as well as the WSI, especially **Thierry** scaling **Klein**, **Julien** transport **Pernot**, the Master of the X-rays **Luc Ortéga**, the Master of epitaxy **Franck Omnès**, **Pierre** machine care **Giroux**, **Jacques** le maître d'astuces **Marcus**, **Philippe** the Handwerker **Plaindoux**, programming **Bartosz Zawilski**, the Masters of the STS **Claude Chapelier**, **Thomas Dubouchet**, and **Benjamin Sacépé**, as well as **Herve Courtois** and **Franck Dahlem**, **Anne-Marie** AFM **Bonnot**, **Daniel** PPMS **Braithwaite**, the dilution and diluette Masters **Xavier Jehl**, **Marc Sanquer**, **Andrew Huxley**,

and **Florence Lévy**, and last but not least the WSI diamond backbone **José Antonio Garrido** and **Wojciech Gajewski**.

All the other collaborators and sample providers: **Oliver** nanocrystalline diamond **Williams**, the Si:B Gilders **Jacques Boulmer** and **Dominique Débarre**, **Gabriel** VLS 4H-SiC:Al **Ferro**, the ab intio Masters **Xavier Blase** and **Emmanuel Bourgeois**, the slovakian power **Jozef Kačmarčik**, the Master of SIMS **François Jomard**, the inelastic X-ray scatterers **Moritz Hösch**, **Jorge Serrano**, and **Michael Krisch**, **Hervé** ARPES **Guyot**, the several not mentioned related materials provider **Florian Furtmayr**, **Robert Lechner**, **Christian Jäger**, **Michael Scholz**, and the Master of granularity **Igor Beloborodov**.

All the administrative staff and secretaries for their indispensable help: **Gwenaelle Stephane**, **Véronique Fauvel**, **Marielle Lardato**, **Martine Lemoine**, **Sabine Gadal**, **Louise Infuso**, **Marielle Perrier**, and **Veronika Enter**.

All my fellow (PhD) students, especially **Pierre Darancet** and **François Varchon** and their office in which time scales differently, **Raoul Piquerel**, **Charles Agnès**, **Slimane Ghodbane**, **Thomas Wojewoda**, **Frederik Gustafsson**, **Estelle Colombier**, **Céline Tavares**, **Pierre-Nicolas Volpe**, **Roland Dietmüller**, and **André Stegner**.

My father, who supported and encouraged me all the time.

All my very precious and valuable friends from the old and from the new times.

Diana Lopez para todo lo que representa para mi! Sin ella no habría sido posible.

TITRE

Transition métal-isolant et supraconductivité du diamant dopé au bore et des matériaux voisins

RESUME

La transition métal-isolant et la supraconductivité induites par le dopage ont été étudiées dans le diamant monocristallin fortement dopé au bore (propriétés structurales, approche en loi d'échelle de la transition métal-isolant, substitution isotopique, structure de bande et son importance pour les mesures d'effet Hall, modes de vibration des dimères de bore) et dans des matériaux voisins. La supraconductivité a été découverte dans le cas du silicium monocristallin fortement dopé au bore (échantillons élaborés par la méthode GILD), ainsi que la transition métal-isolant dans le cas du carbure de silicium 4H fortement dopé à l'aluminium (échantillons élaborés par la méthode VLS). L'étude de la transition métal-isolant et du magnétotransport à basse température dans le diamant nanocristallin dopé au bore a montré l'importance de la granularité de ce système.

TITLE

Metal-insulator transition and superconductivity in heavily boron-doped diamond and related materials

SUMMARY

The doping-induced metal-insulator transition and superconductivity have been studied in highly boron-doped single crystal diamond (structural properties, scaling law approach for the metal-insulator transition, isotopic substitution, band structure and its influence on Hall effect measurements, vibrational modes for boron dimers) and related materials. Superconductivity has been discovered in the case of highly boron-doped single crystal silicon (samples prepared by GILD), as well as the metal-insulator transition in the case of highly aluminum-doped 4H silicon carbide (samples prepared by VLS). The study of the metal-insulator transition and of the low temperature magnetotransport in highly boron-doped nanocrystalline diamond has shown the importance of the granularity in this system.